

Mario Bica de Moraes
IFGW - UNICAMP

BACKSCATTERING SPECTROMETRY

Wei-Kan Chu

IBM
East Fishkill Facility
Hopewell Junction, New York

James W. Mayer Marc-A. Nicolet

California Institute of Technology
Pasadena, California



ACADEMIC PRESS New York San Francisco London 1978

A Subsidiary of Harcourt Brace Jovanovich, Publishers

PHYSICAL CHEMISTRY CAMP
class: 539.752
author: C.554 JF
...00. ...
Lombard, 581R
22-82

COPYRIGHT © 1978, BY ACADEMIC PRESS, INC.
ALL RIGHTS RESERVED.
NO PART OF THIS PUBLICATION MAY BE REPRODUCED OR
TRANSMITTED IN ANY FORM OR BY ANY MEANS, ELECTRONIC
OR MECHANICAL, INCLUDING PHOTOCOPY, RECORDING, OR ANY
INFORMATION STORAGE AND RETRIEVAL SYSTEM, WITHOUT
PERMISSION IN WRITING FROM THE PUBLISHER.

ACADEMIC PRESS, INC.
111 Fifth Avenue, New York, New York 10003

United Kingdom Edition published by
ACADEMIC PRESS, INC. (LONDON) LTD.
24/28 Oval Road, London NW1 7DX

Library of Congress Cataloging in Publication Data

Chu, Wei-Kan.
Backscattering spectrometry.

Bibliography: p.

1. Alpha ray spectrometry. 2. Backscattering.

I. Mayer, James W., Date joint author.
II. Nicolet, Marc-A., joint author. III. Title.
AC793.5.A227C47 539.7'522 78-82418
ISBN 0-12-173850-7

PRINTED IN THE UNITED STATES OF AMERICA

*To the members of the
Kaiserlich-Königliche Böhmisches Physikalische Gesellschaft,
whose field of particle-solid interactions
is the basis of backscattering spectrometry*

Contents

Preface	xi
Acknowledgments	xv
Chapter 1 Introduction	
1.1 Introduction	1
1.2 Concept of a Backscattering Experiment and Its Layout	3
1.3 Basic Physical Processes	6
1.4 Examples and Applications	9
1.5 Strengths and Weaknesses of Backscattering Spectrometry	12
1.6 How to Read a Backscattering Spectrum	14
1.7 Book Outline	19
References	20
Chapter 2 Basic Physical Concepts	
2.1 Introduction	21
2.2 Kinematic Factor K	22
2.3 Scattering Cross Section σ	26
2.4 Energy Loss and Stopping Cross Section	32
2.5 Linear Additivity of Stopping Cross Sections (Bragg's Rule)	43
2.6 Energy Straggling	45
2.7 Linear Additivity of Energy Straggling	51
References	52

Chapter 3 Concepts of Backscattering Spectrometry

3.1	Introduction	54
3.2	Depth Scale for an Elemental Sample	59
3.3	Energy E before Scattering	64
3.4	Numerical Methods to Find the Energy E before Scattering	67
3.5	Height of an Energy Spectrum for an Elemental Sample	68
3.6	Depth Scale for a Homogeneous Solid Containing More Than One Element (Compound Sample)	76
3.7	Height of an Energy Spectrum for a Homogeneous Solid Containing More Than One Element (Compound Sample)	80
3.8	High-Energy Edge of an Energy Spectrum for an Elemental Sample with Several Isotopes	84
3.9	Energy Loss and Yield Respond to Atoms per Unit Area	85
3.10	Numerical Methods to Compute Backscattering Spectra	87
	References	88

Chapter 4 Backscattering Spectrometry of Thin Films

4.1	Introduction	89
4.2	Energy Spectrum of a Thin Elemental Film	90
4.3	Energy Spectrum of Multilayered Elemental Films	94
4.4	Energy Spectrum of a Homogeneous Thin Film Containing More Than One Element (Compound Film)	105
4.5	Energy Spectrum of Multilayered Films Containing More Than One Element (Layered Compound Films)	111
4.6	Influence of Energy Straggling and System Resolution	116
	References	122

Chapter 5 Examples of Backscattering Analysis

5.1	Introduction	123
5.2	Surface Impurity on an Elemental Bulk Target	124
5.3	Elemental Samples Containing Uniform Concentrations of Impurities	127
5.4	Composition of Homogeneous Samples Containing More Than One Element	130
5.5	Impurities Distributed in Depth in an Elemental Sample	137
5.6	Thickness of Thin Films	144
	References	152

Chapter 6 Instrumentation and Experimental Techniques

by R. A. LANGLEY

6.1	Introduction	153
6.2	Accelerator	154
6.3	Energy Stabilization System	160
6.4	Energy Calibration	161
6.5	The Vacuum System	164
6.6	Beam Definition and Measurement	166
6.7	Backscattering Beam Energy Analysis	170
6.8	Sample Holders	181
	References	183

Chapter 7 Influence of Beam Parameters

7.1	Introduction	185
7.2	Mass Resolution	186
7.3	Accessible Depth	193
7.4	Depth Resolution at Normal Incidence	198
7.5	Depth Resolution at Glancing Incidence	203
7.6	Sensitivity to Detection of Surface Impurities	207
7.7	Low-Energy Tails	209
7.8	Non-Rutherford Scattering, Nuclear Reactions, and Detection of Low-Mass Impurities	210
7.9	Microscopic Beam and Nonuniform Layers	218
	References	220

Chapter 8 Use of Channeling Techniques

8.1	Introduction	223
8.2	Crystal Alignment Procedures	225
8.3	Perfect Crystal	230
8.4	Lattice Disorder Amorphous Layers and Polycrystalline Films	239
8.5	Flux Peaking and Lattice Site Location of Impurities	264
8.6	Influence of the Analysis Film	272
	References	273

Chapter 9 Energy-Loss Measurements

9.1	Introduction	276
9.2	Extraction of ϵ Values from $[\epsilon]$ Measurements	277
9.3	Measurement of $[\epsilon]$ from Thin-Film Data	279
9.4	Determination of $[\epsilon]$ from Signal Height	281
	References	287

Chapter 10 Bibliography on Applications of Backscattering Spectrometry

10.1	Introduction	288
10.2	Surfaces	292
10.3	Bulk Properties	294
10.4	Oxide and Nitride Layers	299
10.5	Deposited and Grown Layers	302
10.6	Thin-Film Reactions	305
10.7	Ion Implantation in Metals	310
10.8	Ion Implantation in Semiconductors	313
10.9	Hydrogen and Helium in Metals	315
10.10	Sputtering and Blistering Processes	317
10.11	Microbeams and Other Applications	318

Appendix A Transformation of the Rutherford Formula from Center of Mass to Laboratory Frame of Reference

Appendix B	Influence of Energy Straggling on a Thin-Film Spectrum	323
Appendix C	The True Position of the Edges of a Narrow Rectangular Signal	328
Appendix D	List of Energy-Loss Complications	332
Appendix E	Rough Targets	334
Appendix F	Numerical Tables	339
Table I.	Elements	344
Table II.	K_{M2} for ${}^1\text{H}$ as Projectile and Integer Mass M_2	350
Table III.	K_{M2} for ${}^4\text{He}$ as Projectile and Integer Target M_2	354
Table IV.	\bar{K} for ${}^1\text{H}$ as Projectile	358
Table V.	\bar{K} for ${}^4\text{He}$ as Projectile	360
Table VI.	${}^4\text{He}$ Stopping Cross Sections ϵ	362
Table VII.	Polynomial Fit to the ${}^4\text{He}$ Stopping Cross Sections ϵ	364
Table VIII.	${}^4\text{He}$ Stopping Cross Section Factor [ϵ_0]	366
Table IX.	${}^4\text{He}$ Energy-Loss Factor [S_0]	368
Table X.	Rutherford Scattering Cross Section of the Elements for 1 MeV ${}^4\text{He}$	370
Table XI.	Surface Height of Backscattering Yield for ${}^4\text{He}$ on Elemental Targets H_0	372
Indexes		375

Preface

The conceptual framework on which backscattering spectrometry is based was erected in the years following the discoveries of Rutherford and of Geiger and Marsden (1909–1913). A rapid succession of milestone developments then brought order into the structure of the atom. The nucleus began to attract the attention of increasing numbers in the physics community. Particle accelerators were developed to probe the inner workings of that nucleus. After World War II, the number of accelerators in the 1–3 MeV range increased rapidly. Why, then, did it take about 20 more years before these accelerators came to be used in solving problems outside of the field of nuclear physics? There is probably no single answer to this question. The growth and evolution of interdisciplinary fields of science and technology follow patterns of their own. The rules that govern them and the guidelines one should follow to further such evolutions can perhaps be learned from the study of cases such as that of backscattering spectrometry.

First, one must observe that the nuclear physicists who used these accelerators were fully aware of the analytical power of Rutherford backscattering from the very beginning. For example, it was (and still is) common practice to recognize contaminants of the target by an analysis of backscattered particles. Also, there was a constant trickle of publications over those 20 years to prove

that investigators were always conscious of the analytical possibilities that Rutherford backscattering could offer. Throughout the 1960s, applications of the method were proposed by a steadily increasing number of authors. By the end of that decade, backscattering had taken a foothold.

Another development took place independently. In the early 1960s, the channeling of fast particles moving in a crystalline lattice was rediscovered after having been anticipated by W. H. and W. L. Bragg and by J. Stark in the 1910s. The phenomenon attracted attention and brought particle accelerators into the arena of solid-state physics through the other door. By the time backscattering spectrometry was finding acceptance, channeling had already become an integral part of the method.

Clearly, the idea of using Rutherford backscattering had always been alive. The obstacles in the way of its immediate introduction as an analytical tool outside of nuclear physics were elsewhere.

One difficulty was instrumental. At the outset, the only detectors with good energy resolution were the magnetic spectrometers, which are bulky and time-consuming to operate. Around 1960, solid-state detectors became available. These relatively inexpensive devices promised good resolution, good linearity, fast response, and simultaneous analysis over a wide energy range. Their development was correspondingly rapid. At present they constitute the preferred particle detectors in the energy range of interest to backscattering spectrometry.

Another major experimental improvement occurred in the electronic systems for data handling and processing. Speed, accuracy, stability, and generous capacities for data storage and handling became available at reasonable cost. In combination with a solid-state detector, such a system transformed an accelerator into a rapid and efficient analytical instrument.

Planar technology was first introduced to make semiconductor devices in 1960. Because of its inherent advantages, this technology found rapid acceptance, but with it came numerous novel problems in the formation and control of thin layers used for masking and contacting. The fact that backscattering spectrometry was an ideal tool with which to investigate these problems went unnoticed. The *problems existed*, but those equipped to solve them remained unaware of them, and those seeking answers overlooked the tool.

A direct link between planar technology and backscattering spectrometry was finally established with ion implantation. It offered accurate control of the dopants and uniform surface density over a whole wafer, and thus superior yields. The need arose to establish the depth profile of an implanted atom and the amount of disorder produced by the energetic ions. Backscattering spectrometry came as a fairly natural solution to those familiar with ion beams and ion implantation. In early applications an attribute of backscattering spectrometry that had not been fully appreciated became evident, namely, its ability to provide a depth scale to the elements detected. It is this ability more than any

other that gives backscattering spectrometry its unique analytical power. The great success of the method in connection with thin films, their structure, composition, and reactions, demonstrates this fact very clearly. Actually, a professional society exists whose purpose is to promote the specific field of particle-solid interaction, of which backscattering spectrometry is a recognized part.

Finally, the pressure to bring MeV accelerators to bear on the problems arising in the semiconductor industry came from the semiconductor industry. Typically, it was not the scientists who had already mastered the tool who sought out the problems, but rather the scientists with the problem who sought out the tool. Without the magnanimous response of those in charge of the accelerators, the interdisciplinary effort would not have unfolded. Where the intellectual curiosity for the solution to a problem at hand overruled the man-made subdivisions of scientific disciplines, the barriers fell and backscattering spectrometry rose to success.

So far, the main beneficiary of the technique has been the semiconductor industry, where thin-film and ion implantation problems abound. In sorts, backscattering spectrometry pays a tribute it owes. It was the semiconductor industry's earlier efforts that had readied the MeV accelerators for this task by providing them with suitable detectors and electronic systems.

Acknowledgments

This book grew out of a program supported at Caltech by the Office of Naval Research. We are indebted to Larry R. Cooper for providing the encouragement and the continuity of support necessary to develop backscattering spectrometry into an analytical technique. We are also indebted to the staff of the Kellogg Radiation Laboratory at Caltech for access to the 3-MeV van de Graaff accelerator and for generous support of our activities. In particular we express our gratitude to Charles A. Barnes, who gave freely of his time and talent to assist us and fulfilled the role of godfather to backscattering spectrometry. In all of our work, the assistance of Carol Norris, Rob Gorris, and Jeffrey Mallory was invaluable; it is our pleasure to acknowledge their help and to thank them.

In planning and writing this book, we benefited from the assistance of many of our colleagues: Ian V. Mitchell (Chalk River Nuclear Laboratories), who participated in the initial organization of the material (in 1971); Robert A. Langley, who wrote Chapter 6; Jon Mathews, Johnson O. Olowolafe, Tsu-wei Frank Lee, and Woon Tong Nathan Cheung for their contributions to the appendixes; and J. L. 'Ecuyer and R. F. Lever for helpful suggestions. Finally, we thank our many collaborators who were at Caltech, providing inspiration, hard work, and many unforgettable memories of good times.

Chapter

1

Introduction

1.1 INTRODUCTION

To obtain measurable effects, an intense pencil of alpha particles is required. It is further necessary that the path of the alpha particles should be in an evacuated chamber to avoid complications due to the absorption or scattering in air.

This is how Geiger and Marsden (1913)[†] describe the principal conditions that their experiment had to meet. With it they unambiguously confirmed the validity of the new model of an atom proposed by their leader Ernest Rutherford. Figure 1.1 shows a drawing of the simple apparatus that they built to meet these requirements. The year was 1911. The purpose was to test (and prove) a theory.

Figure 1.2 is a sketch of a similar apparatus. It is taken from the final report of the Surveyor Project (Turkevich *et al.*, 1968) and shows the sensor head of

[†] References are listed at the end of each chapter. We use the year of publication to identify a reference, followed by *a, b, ...*, if necessary to avoid ambiguities.

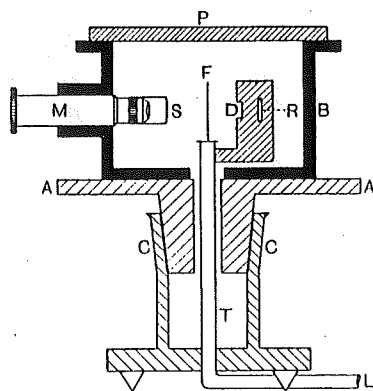


Fig. 1.1 Drawing of the apparatus used by Geiger and Marsden in 1911-1913 to test and confirm the new model of an atom conceived by Rutherford in 1911. "The apparatus . . . consisted of a strong cylindrical metal box B, which contained the source of alpha particles R, the scattering foil F, and a microscope M to which the zinc-sulphide screen S was rigidly attached. The box was fastened down to a graduated circular platform A, which could be rotated by means of a conical airtight joint C. By rotating the platform the box and microscope moved with it, whilst the scattering foil and radiation source remained in position, being attached to the tube T, which was fastened to the stand L. The box B was closed by the ground-glass plate P, and could be exhausted through the tube T." [from Geiger and Marsden (1913).]

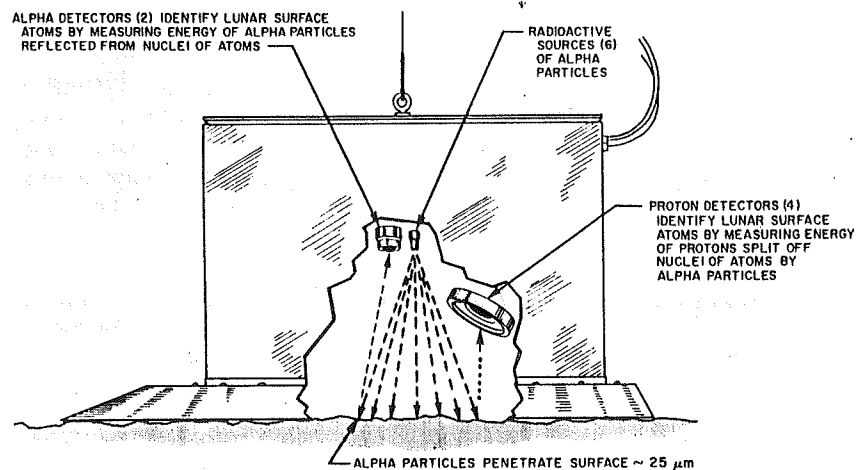


Fig. 1.2 Diagrammatic view of the internal configuration of the alpha-scattering sensor head deployed on the surface of the moon for the first analysis of the lunar soil, executed as part of the scientific mission of Surveyor V after its soft landing on September 9, 1967. [from Turkevich *et al.* (1968).] This experiment was the first widely publicized application to a problem of nonnuclear interest of the concept of Rutherford scattering introduced some 50 years earlier.

the "alpha-scattering experiment" which was part of the scientific payload of Surveyor V. The year was 1967. The purpose of the alpha-scattering experiment was to analyze the composition of the lunar soil. This experiment probably constitutes the first widely publicized practical application of the ideas of Rutherford, Geiger, and Marsden to a problem of nonnuclear interest.

In the rest of this introduction, we paint an overall picture of the analytical technique of backscattering spectrometry as it exists today. We do not dwell on the details, but rather present the idea of the method; what it can and what it cannot accomplish. The purpose of this chapter is to give a general picture of backscattering spectrometry, a few basic concepts, and some "rules of thumb" to guide in interpreting or reading spectra. Details are given in the following chapters as outlined in Section 1.7. However, the contents of this chapter are intended to convey an impression of the relative strengths and weaknesses of backscattering spectrometry in the framework of materials analysis.

1.2 CONCEPT OF A BACKSCATTERING EXPERIMENT AND ITS LAYOUT

Both in its concept and in its elementary execution, Rutherford scattering is quite a simple experiment. A beam of monoenergetic and collimated alpha particles (^4He nuclei) impinges perpendicularly on a target. When the sample that constitutes the target is thin, as in the experiment of Geiger and Marsden, almost all of the incident particles reappear at the far side of the target with some slightly reduced energy and only slightly altered direction; that is, the beam is transmitted through the thin target with only very little loss of particles. The situation is sketched in Fig. 1.3. The few alpha particles that are lost undergo large changes in energy and direction, changes due to close encounters of the incident particles with the nucleus of a single target atom. If the sample is thick, only the particles scattered backward by angles of more than 90° from the incident direction can be detected. This is the situation that prevailed in the Surveyor V experiment (Fig. 1.2). It is also that which is adopted in the analytical technique discussed in this book, hence the name *backscattering spectrometry*.[†]

The typical experimental system used today for routine backscattering analyses is considerably more elaborate than the setups shown in Figs. 1.1 and 1.2. Figure 1.4 gives a schematic outline of the major components of

[†] An alternative name is *Rutherford backscattering spectrometry*. However, since the scattering cross section can deviate from that given by the Rutherford formula, we use the more general term *backscattering spectrometry*.

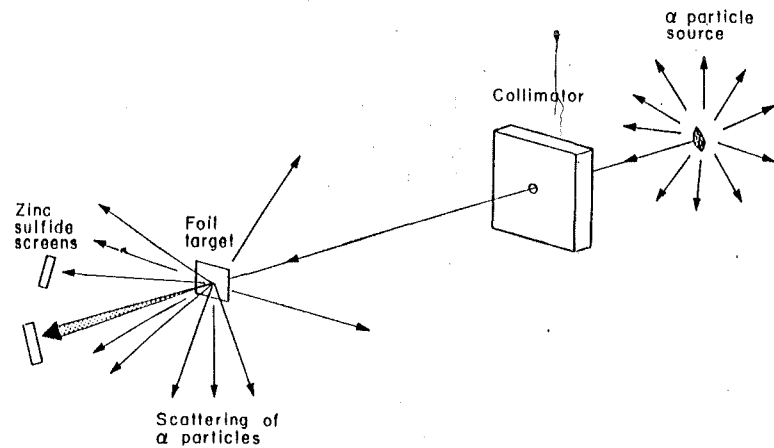


Fig. 1.3 Conceptual layout of a scattering experiment. In the experiment of Geiger and Marsden (Fig. 1.1) the source was a thin-walled glass tube filled with radon and enclosed in a lead box, shown shaded in the diagram. The collimator consisted of a simple diaphragm. In the experiment of Surveyor V, the six sources were of ^{242}Cm which emits alpha particles of 6.1 MeV. A short tubular extension of the stainless steel capsule that contained the curium acted as the collimator. The collimator opening was covered with a thin film of aluminum oxide plus polyvinylstyrene, totaling about 1000 Å in thickness, to prevent contamination of the lunar soil or the apparatus by radioactive material.

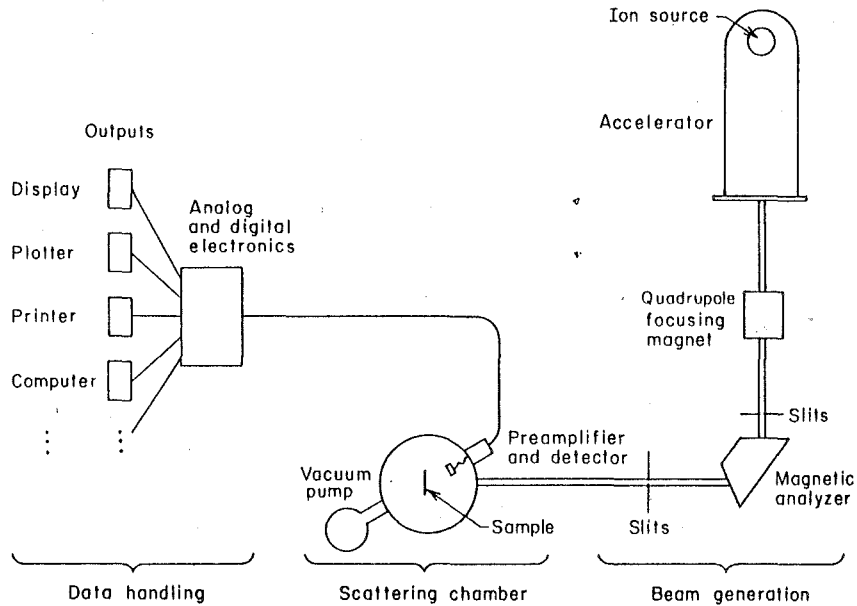


Fig. 1.4 Schematic diagram of a typical backscattering spectrometry system in use today.

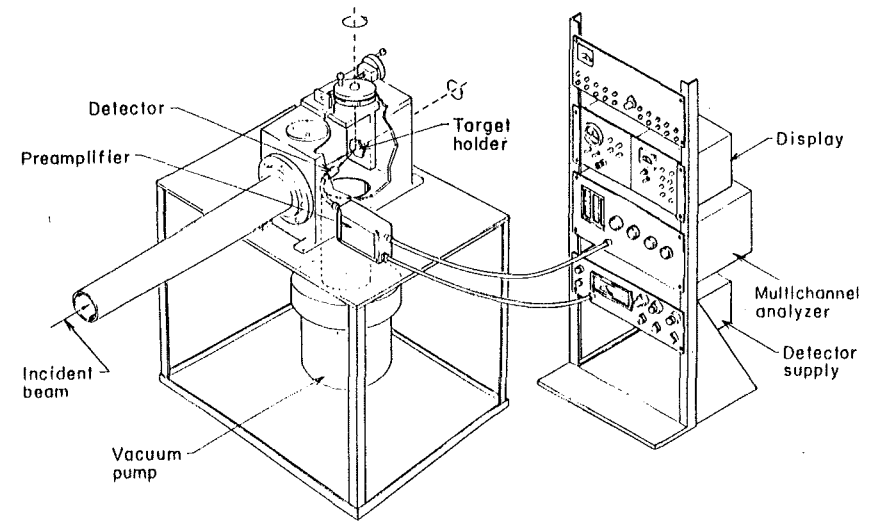


Fig. 1.5 Layout of the target chamber and electronics of a backscattering system. The ions impinge on the target in the vacuum chamber. Backscattered particles are analyzed by the detector, and the detector signal is magnified and reshaped in the preamplifier. The electronic equipment in the rack provides power to the detector and preamplifier and stores the data generated by the detector in the form of the backscattering spectra.

such a system. Charged particles are generated in an ion source. Their energy is then raised to several megaelectron volts by an accelerator, usually a van de Graaff (or a similar kind). The high-energy beam then passes through a series of devices which collimate or focus the beam and filter it for a selected type of particle and energy. This equipment replaces the simple source-and-diaphragm arrangement of Figs. 1.1 and 1.2. The immense advantage of this system over the natural source-and-diaphragm apparatus is that the beam parameters can now be varied over a wide range. In particular, higher particle fluxes can be obtained as compared to natural sources; this drastically shortens the measurement time. The beam then enters the scattering chamber and impinges on the sample to be analyzed (Fig. 1.5). Some of the backscattered particles impinge on the detector, where they generate an electrical signal. This signal is amplified and processed with fast analog and digital electronics. The final stage of the data usually has the form of a (digitized) spectrum, hence the name backscattering *spectrometry*.

In spite of the sophistication in the beam-generating parts and the data collection end of a backscattering spectrometry system, the chamber in which the backscattering experiment is performed remains simple (Fig. 1.6). Apart from the box and the sample themselves, it has only three elements: the beam, the detector, and the vacuum pump. The requirements on the

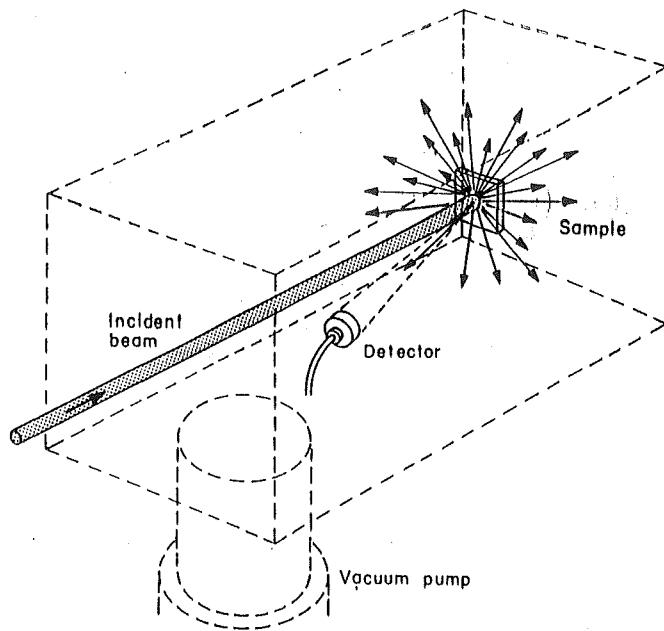


Fig. 1.6 Even in a sophisticated backscattering spectrometry system, the scattering chamber where the analysis/experiment is actually performed remains simple. Apart from the box forming the chamber and the sample, there are only three other elements: the beam, the detector, and the vacuum pump.

vacuum are quite modest by today's standards: 10^{-5} Torr is expedient, and 10^{-6} Torr is quite adequate. Such vacua allow simple handling procedures and rapid turn-around times for unloading and reloading samples. A well-functioning backscattering spectrometry system can analyze many samples a day. As a research tool, one system is able to satisfy the demands of a number of people and projects at a time. As a tool for routine surveys, a system can easily be automated for both the execution of the experiment and the reduction of the data.

1.3 BASIC PHYSICAL PROCESSES

The translation of individual signals in a backscattering spectrum to depth distributions of atomic concentrations in a sample rests on simple physical principles. Imagine a single self-supporting layer with two elements M and m in equal amounts, 10^{15} atoms/cm² each, as shown in Fig. 1.7. Imagine further that a flux of ⁴He particles of 1-MeV energy impinges on this layer. Those few ⁴He particles that do undergo close encounters will be deflected because of the enormous Coulombic force they encounter. If the energy of

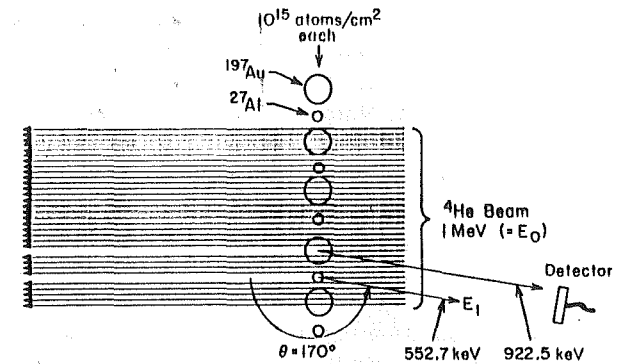


Fig. 1.7 The kinematic factor K_M gives the ratio of the energy after (E_1) to that before (E_0) an elastic collision of the projectile (here ⁴He) with an atom of mass M (197 amu for Au, 27 amu for Al). The heavier mass reflects the incoming particle more completely, energetically, than the lighter mass, as is the case with billiard balls. Two examples are shown and actual values are given.

the incident ⁴He ion is not too high, nuclear reactions can be ruled out during the collision process as well. The collision then must be an elastic one. The phenomenon is similar to the collision of two hard spheres and can be solved exactly. The kinematic factor K is the ratio of the energy of the projectile after to that before the collision. It is listed in Tables II and III for ¹H and ⁴He as projectiles.[†] As an example, assume that the two elements are Au and Al, whose atomic masses are 197 and 27 amu, respectively (see Table I). For a scattering angle of 170° , we find from Table III that $K_{Au} = 0.9225$ and $K_{Al} = 0.5527$. A 1-MeV ⁴He particle therefore, has an energy of 922.5 keV after a collision with Au, and an energy of 552.7 keV after a collision with Al.

The probability that a collision will result in a detected particle is given by the differential scattering cross section $d\sigma/d\Omega$, which is tabulated for all elements with ⁴He as a projectile in Table X. For Au, $d\sigma/d\Omega$ is 32.81×10^{-24} cm²/sr for each atom; for Al, $d\sigma/d\Omega$ is 0.8512×10^{-24} cm²/sr. To find the average scattering cross section σ over the field of view of the detector, we must multiply this differential scattering cross section with the solid angle of detection Ω , which we shall assume to be 10^{-3} sr (a typical order of magnitude for real systems). Adding up the scattering cross section of all atoms in the layer (10^{15} atoms/cm² each), we find for Au, 3.3×10^{-11} and for Al, 8.5×10^{-13} . These dimensionless numbers give the probability that a ⁴He projectile will undergo a close encounter with Au or Al in the layer[†] and end up in the detector. Assume that the integrated current of 1-MeV ⁴He⁺ ions during the exposure of the layer was $1 \mu\text{C}$ (which is a typical

[†] Tables I–XI are given in Appendix F.

number used to obtain a backscattering spectrum); the total number of ^4He ions that fell on the sample was then 6.2×10^{12} . The probable number of events counted after scattering from Au atoms is therefore about 200, and the number from Al is about five. Note that the charge state of the particles in the ion beam, whether $^4\text{He}^+$ or $^4\text{He}^{++}$ (alpha particles), relates integrated current to number of incident particles but does not influence scattering or energy loss cross sections.

Now imagine that the sample is a self-supporting Au film 1000 Å thick and that the analysis beam consists of 2.0-MeV ^4He ions (see Fig. 1.8). A scattering event at the front surface of the film is detected at an energy $K_M E_0$; the same event at the rear surface is registered at a lower energy. The energy difference $\Delta E = 133$ keV is nearly ten times the energy resolution of standard particle detection systems, and hence it is straightforward to determine whether particles were scattered at the front or rear surfaces of the film. Scattering events that take place somewhere between front and rear surfaces are recorded at some intermediate energies. Since the beam is unattenuated, the scattering probability at any depth is proportional to the number of atoms of a particular kind present there. This is the way a concentration profile of a given element is translated into a signal of corresponding height and decreasing energy in the backscattering spectrum.

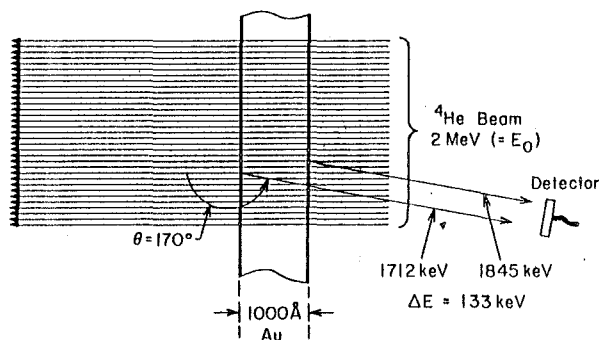


Fig. 1.8 A swift particle that passes through a dense medium loses some of its energy. As a consequence, a particle scattered back at the rear surface of a film has less energy when it is detected than a particle scattered at the front surface. Actual values are given for a 1000-Å-thick Au film.

The fact that the signal of ^4He particles scattered from the Au film has a finite energy width reflects the energy loss of the particles along their inward and outward paths. Such energy losses can be calculated from the stopping cross section ϵ , which is given for ^4He ions in Table VI in units of electron volts per 10^{15} atoms per square centimeter; for 2.0-MeV ^4He ions, the value of $\epsilon^{\text{Au}} = 115.5$. To determine the energy lost along the inward track to the rear

surface of a film of thickness t and atomic density N , one takes the product of ϵ and Nt , where Nt represents the number of atoms per square centimeter in the film. For the Au film (where $N_{\text{Au}} = 5.9 \times 10^{22}$ atoms/cm³ as given in Table I) the value of $Nt = 5.9 \times 10^{17}$ atoms/cm² and a particle would lose 68.1 keV along the inward path.

The detected energy difference between particles scattered from the front and back surfaces of the film is given by the product of Nt and $[\epsilon]$, where values of $[\epsilon]$, the stopping cross section factor, are listed in Table VIII for scattering angles of 170° . In Table VIII, the units of $[\epsilon_0]$ are electron volts per (10^{15} atoms per square centimeter) and the value for $[\epsilon_0]^{\text{Au}} = 226.2$. For a film with 5.9×10^{17} atoms/cm², the energy width $\Delta E = 133.4$ keV. This energy width could also have been found directly from the values of the energy loss factor $[S]$ given in Table IX for ^4He in units of electron volts per angstrom. However, the use of an energy-to-depth conversion with units of electron volts per angstrom overlooks the fact that backscattering spectrometry reflects the number of atoms per square centimeter traversed by a particle rather than the physical depth in centimeters. The conversion between the two is direct if the atomic density of the sample is known.

If the energy loss that the particle suffers as it traverses the sample were independent of energy, the relationship between the depth of the collision and the energy of a detected particle would be linear. As a matter of fact, the success of backscattering spectrometry in the analysis of thin films is partly attributable to the small relative change in the energy of the beam as it traverses the film. The energy dependence of the stopping cross section can then be replaced by two fixed values, one along the inward path and one along the backward path across the film. For very thick films where this approximation fails, the analysis of a spectrum is not as simple. However, a large part of this book discusses suitable approximations.

The fact that the projectile loses energy as it penetrates into the sample has another consequence. Scattering cross sections depend on the energy of the impinging projectile as $(\text{energy})^{-2}$. Deeper down in the sample, where the energy of the projectile decreases, the scattering probability increases. The signal of an element which is uniformly distributed in depth is therefore not flat-topped, but rises toward lower energies. This, too, complicates the quantitative analysis of a spectrum.

1.4 EXAMPLES AND APPLICATIONS

Applications date back to some of the early nuclear investigations with accelerators, when it was common practice to recognize contaminants of the target by an analysis of backscattered particles (Tollestrup *et al.*, 1949). The earliest applications to problems of nonnuclear interest were the analyses of smog (Rubin and Rasmussen, 1950) and of the bore surfaces of gun barrels

(Rubin, 1954). Other contributions were those of Rubin *et al.* (1957) and Mazari *et al.* (1959), who detected trace elements on thick and on thin targets, respectively, and of Sippel (1959), who measured the diffusion of Au into Cu. In 1960, S. K. Allison suggested the method for the remote analysis of surface composition. Following his suggestion, Turkevich (1961) proved in preliminary investigations that the method was feasible, and Patterson *et al.* (1965) laid the groundwork that culminated in the compositional analysis of the moon's soil by Surveyor V in 1967 (Turkevich *et al.*, 1968).

In this section, however, we present three more recent examples to give a feeling for backscattering spectrometry. The first deals with the detection of contaminants on the surface of Si, while the second shows the depth distribution of a dopant in Si, and the third shows examples of thin film analysis. Other examples are given in Chapter 5.

1.4.1 Surface Impurities

As a first example, we present in Fig. 1.9 a schematic energy spectrum of ^4He backscattered from a Si target with Cu, Ag, and Au on the surface, each in the amount of about 10^{15} atoms/cm 2 . This is of the order of one monolayer of surface coverage. The spectrum was taken with a ^4He beam of incident energy $E_0 = 2.8$ MeV. The lower abscissa gives the energy scale of the backscattering spectrum. The upper abscissa gives the mass M associated with the positions $K_M E_0$ for the three impurity elements and for Si. Note that the mass-to-energy conversion established via K_M is unique, but nonlinear. Au is the only element in this example that has only one stable isotope (see Table I) and produces only one signal in the spectrum. The two signals of the Ag

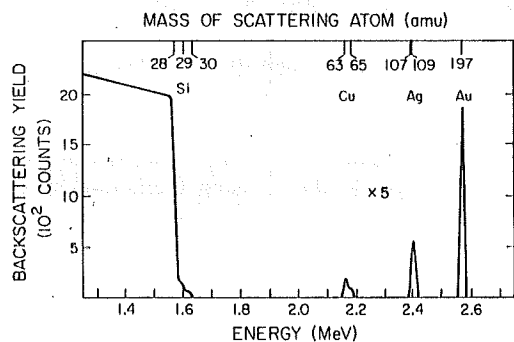


Fig. 1.9 Schematic energy spectrum of ^4He backscattered from a Si substrate with about 10^{15} atoms/cm 2 each of Cu, Ag, and Au (equivalent to approximately one monolayer of coverage). Projectile: $^4\text{He}^+$ of 2.8-MeV incident energy; scattering angle of detected particles: 170° ; solid angle of detection: 4 msr; total dose (integrated current of incident beam): $10 \mu\text{C}$; energy per channel: 5 keV; resolution: 12.5 keV (FWHM). The ordinate for the signals of Cu, Ag, and Au is magnified five times.

isotopes cannot be distinguished, because the energy resolution of the detection system is too coarse. The signals of the two Cu isotopes are just barely resolved.

The area under each impurity peak is proportional to the number of impurity atoms per unit area and the scattering cross section of the element. Since the surface coverage is about equal for all three impurities, the size of the signals reflects the change in cross section. We are thus able to determine the exact ratio of atoms per square centimeter between these impurities by dividing the area of the signals through the respective scattering cross sections and obtain quantitative results without using standards of calibration. The signals of the two Cu isotopes indicate directly their relative abundance. The Si part of the spectrum is characteristic of a thick sample. Here it is the height of each step at the appropriate energy edge $K_M E_0$ that is proportional to the isotopic abundance (92.2, 4.7, and 3.1% from Table I).

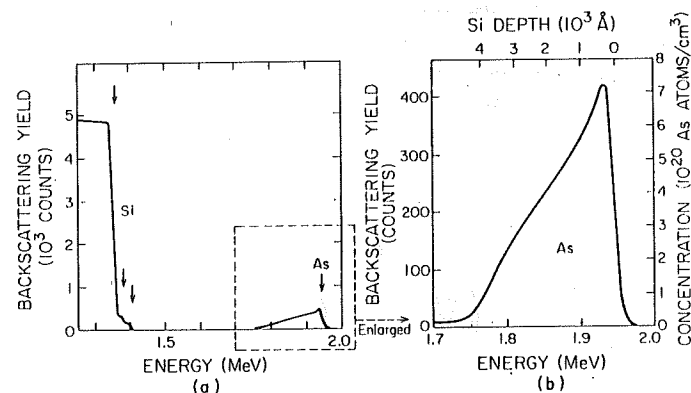


Fig. 1.10 Schematic energy spectrum of 2.4-MeV ^4He backscattered [part (a)] from a Si substrate doped with As. The As signal is magnified in a separate plot [part (b)], where the axis of energy (bottom) is converted to depth below the surface (top) and the axis of yield (left) is converted to atomic volume concentration (right). The spectrum was measured with the same system parameters as those given in Fig. 1.9, except for the incident energy ($E_0 = 2.4$ MeV) and the dose ($20 \mu\text{C}$).

1.4.2 Impurity Distribution in Depth

As a second example, Fig. 1.10 shows a schematic energy spectrum of ^4He backscattered from a Si sample implanted with As and then heat-treated to diffuse As deeper into the sample. The conversions of the backscattering yield of As to an As concentration as well as the energy axis to one giving the depth of As in Si are given in the enlarged part of the figure. Both conversion scales are linear with only minor corrections.

The concentration scale for the As signal conveys an idea of the sensitivity of backscattering spectrometry in detecting impurities. Compared to other

methods—for example, neutron activation analysis or secondary ion mass spectroscopy—backscattering spectrometry is not very sensitive. However, backscattering spectrometry is capable of quantitative measurements without recourse to standards. It can also furnish depth profiles without layer removal by ion sputtering or chemical stripping, which is generally required with other profiling methods.

1.4.3 Thickness Measurements

The measurement of film thicknesses is an obvious way of making use of backscattering spectrometry. Figure 1.11 shows schematic spectra of ^4He backscattered from Ta films of various thicknesses. Several spectra are plotted on the same axes to illustrate the relation between the energy shift and the film thickness: they are nearly proportional. The accuracy of the thickness measurement is directly determined by the accuracy of the energy loss values used for the analysis. Here we have used the values listed in Table IX. As stated previously, the area under each signal is proportional to the total number of Ta atoms in the film. Consequently, one can obtain the film thickness from the area of a signal as well.

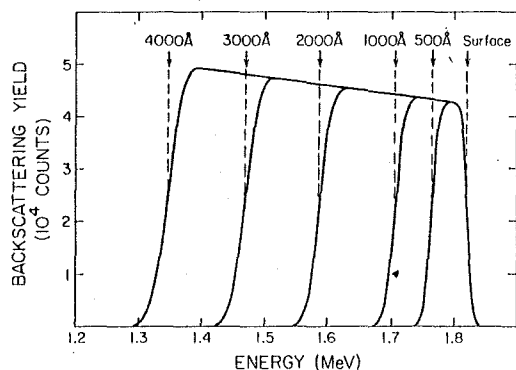


Fig. 1.11 Display of five backscattering spectra combined to show how the width of the signal from a thin film reflects the thickness of the films. The incident energy of the ^4He ions is 2.0 MeV and the five targets were Ta films deposited on SiO_2 substrates (the substrate signals are not shown in the spectra).

1.5 STRENGTHS AND WEAKNESSES OF BACKSCATTERING SPECTROMETRY

The strength of backscattering spectrometry (BS) resides in the speed of the technique, its ability to perceive depth distributions of atomic species below the surface, and the quantitative nature of the results. Furthermore, with single-crystal targets, the effect of channeling also allows the investigation of the crystalline perfection of the sample.

The speed of the data collection is possible in part because the modest requirements on the vacuum permit fast sample changing. The modest vacuum is admissible only because BS measures the bulk of the sample not its surface. Since the typical depth resolution of 100 to 200 Å precludes a study of the first few monolayers, vacua of 10^{-9} or 10^{-10} Torr, which true surface techniques demand, are unnecessary for BS.

The great increase in sensitivity for heavy elements is an asset for the detection of these elements, but a severe limitation for the detection of light elements. Carbon, nitrogen, and oxygen are ubiquitous elements and therefore of great significance in the near-surface regions of a solid; yet BS is nearly blind to trace quantities of them. This disadvantage is often overcome in studies of thin films by depositing the film on a low atomic mass substrate such as carbon. This approach allows ready identification of signals from oxygen contaminants, for example. Another weakness is the lack of specificity in the signal. After a scattering event, all backscattered particles are alike, save for their energy. Two elements of similar mass cannot be distinguished when they appear together in a sample. This lack of specificity of the signal can be resolved by other analytical tools, such as Auger electron spectroscopy. Finally, one must realize the stringent requirements on lateral uniformity that a sample must meet before the full capability of BS can be utilized. A typical ion beam diameter used for backscattering is 1 mm^2 . If the range of depth analyses is 2000 Å, the width of the beam spot is a factor of 5×10^3 larger than the thickness of the layers. Scratches, cavities, dust particles, and any other surface nonuniformities can drastically modify the spectrum, if present in sufficient amounts, even if they are of a submicron size. The lateral uniformity of a sample must therefore be assured on the surface as well as in depth.

The most convenient way to establish this uniformity is scanning electron microscopy (SEM), which has excellent lateral resolution and thus constitutes the normal complementary tool for BS. Unfortunately, SEM provides surface topography, without vision below, and with little elemental specificity. X-ray attachments can provide the missing elemental specificity. In this respect, an electron microprobe is an even superior counterpart to BS because it combines good elemental specificity and good lateral resolution. The drawback of the electron microprobe is that the x-ray signal reflects the average composition over depths quite large compared to the depth resolution of a backscattering spectrum.

Another limitation of BS is that chemical information is totally absent. X-ray diffraction of various sorts, in particular the Read camera, has been found most useful for the determination of crystallographic parameters. Usually the combination of atomic composition ratios furnished by BS and the knowledge of diffraction patterns give convincing evidence of the actual nature of the compound present.

Auger electron spectrometry (AES) and secondary ion mass spectroscopy (SIMS) are two other techniques that complement BS well. Both have elemental specificity; but their main drawback is their reliance on ion sputtering for depth profiling. Ion sputtering can modify the sample under investigation and lead to erroneous conclusions (e.g., laterally dissimilar erosion rates or preferential sputtering). The consequences can be particularly severe in AES, where the signal emanates from the uppermost layer of the sputtered area. AES, on the other hand, can be quantified by comparison with reference samples. In SIMS, quantification is still more difficult because the fraction of the ionized (and hence detected) atoms sputtered from the substrate depends on the chemical surrounding of that atom in the sample and on the sputtering gas. In sensitivity, however, SIMS far surpasses most other analytical techniques.

One of the advantages of BS is that it provides depth distributions without the requirements for destruction of the sample by layer removal as in the case of sputter sectioning used with AES or SIMS. However, BS will introduce damage. Whether BS should be considered destructive or not depends on the object analyzed and also on the questions asked. A shallow *pn* junction, for instance, is rapidly destroyed by small doses of irradiation if one looks at the reverse current, but remains essentially unaltered if one considers the doping profile. As a rule, metallurgical structures are quite insensitive to the irradiation doses used in BS.

It is clear that for a full characterization of a sample every possible tool must be brought to bear because each tool has limitations. Only a combination of techniques—fewer if those applied are well adapted to the problem or wisely selected and more of them otherwise—can permit hard conclusions. BS occupies a select place among these tools, in spite of having been a late-comer in the scene, because it is fast, ideally suited for large surveys or routine applications, and quantitative.

1.6 HOW TO READ A BACKSCATTERING SPECTRUM

One of the advantages of backscattering spectrometry is that the spectrum can be interpreted rather easily. In this section, we show how the form of a backscattering spectrum provides insight into the composition of a sample. Which physical process is actually responsible for the various characteristics of a spectrum does not concern us at this point. We shall actually proceed backward and assume that the composition of the sample is known, and show by what basic rules this information is translated into a backscattering spectrum. In a practical case, of course, the process is reversed.

Consider a thin film composed of a uniform mixture of two elements, as in the case of a binary compound or two fully miscible solids. To reduce the example to its simplest form, we shall ignore the substrate. For backscattering

ing spectrometry, the masses of the two elements and their atomic numbers are highly significant. We shall therefore characterize the two elements by their masses M and m , rather than by their chemical symbols. To start with, let us assume that the two elements are present in the film in the same proportion; i.e., the atomic concentrations of both elements are the same. This state of affairs is represented graphically in Figs. 1.12a and b. The profile of

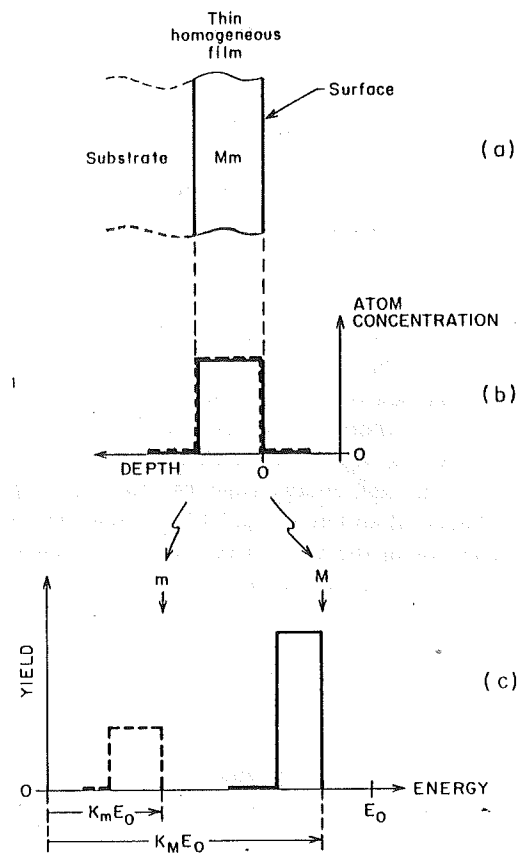


Fig. 1.12 (a) Translation of concentration profiles to signals in a backscattering spectrum, demonstrated for the example of a thin homogeneous film of a binary compound with elements of a heavy M and a light m atomic mass. (b) The atomic concentrations are the same for both elements. (c) In the backscattering spectrum, the two profiles reappear as two separate signals. The light mass gives a signal at low energies with a low yield. The heavy mass produces a signal at high energies of a high yield. The high-energy edge of each signal (arrows marked m and M) is pegged on the energy axis of the spectrum to the value given by the kinematic factor K , where E_0 is the energy of the incident particles. The yield ratio of the two signal heights is given (approximately) by the ratio of the scattering cross section σ_M/σ_m of the two elements, which is proportional to $(Z/z)^2$, the square of the ratio of the atomic numbers Z and z of the heavy and light elements.

atomic concentration versus depth given in Fig. 1.12b translates into the corresponding backscattering spectrum of Fig. 1.12c as follows:

1. The rectangular profile of the element with the *heavy* mass (M , say) reappears in the backscattering spectrum as a rectangular signal located on the energy axis at *high* energies; the profile of the element with the *light* mass (m , say) gets a place in the backscattering spectrum at *low* energies. The rule for the translation of the abscissas thus is *heavy masses go to high energies; light masses to low energies*.

2. Atomic concentrations of the same value in Fig. 1.12b are plotted at different levels on the yield axis of the backscattering spectrum in Fig. 1.12c. If the atomic number of the element is high, the yield is high too, and if the atomic number of the element is low, the yield is low. The rule for the translation of the ordinates reads: *High atomic numbers give high yield; low atomic numbers give low yields*. In effect, these two rules amount to saying that each element has its own coordinate system in the backscattering spectrum.

The discussion so far is qualitative. The power of backscattering spectrometry now resides in the fact that the two translations just described can be formulated in quantitative terms. For the x axis of the backscattering spectrum, for instance, there is the so-called *kinematic factor* K , which states where, exactly, the signal of an element of any given mass has its high-energy edge. (The high-energy edge, or "leading" edge, of the signals of the elements of mass M and m in Fig. 1.12 are indicated by arrows marked M and m .) The location of the high-energy edges are indicated by the length of the arrows labeled $K_m E_0$ below the energy axis of the spectrum of Fig. 1.12c.

In very similar fashion, the scattering cross section σ gives the scaling factor for the yield axis of different elements. The relative concentration ratio of two elements transforms into relative yields by a ratio given essentially by the cross section ratio of the elements or by $(Z/z)^2$. Some corrections must be applied. These are usually small (less than 10%), but the fact that they do exist has much to do with the reason this book is written. For example, the thicknesses that the two atomic species M and m occupy in the film (Figs. 1.12a and b) are the same; the widths that the signals of these two elements occupy on the energy scale of the backscattering spectrum are not. The range of depth in the film is thus translated into an energy interval on the energy axis of the spectrum, but that interval is not quite the same for each signal. If both intervals were identical, the scaling factor for the two yields would be correctly given by the ratio of the scattering cross sections of the two elements. Generally the intervals differ but not by much (about 10% or less); hence the correction on the yields.

To summarize, the translation of the concentration profiles of the two elements in the film (Fig. 1.12b) into the two signals of the backscattering spectrum of Fig. 1.12c may be viewed in the following way (see Fig. 1.13): There is a coordinate system for each mass in the target, plotting the atomic concentration of that mass as a function of increasing depth below the surface of the sample on which the analyzing beam impinges. Each profile

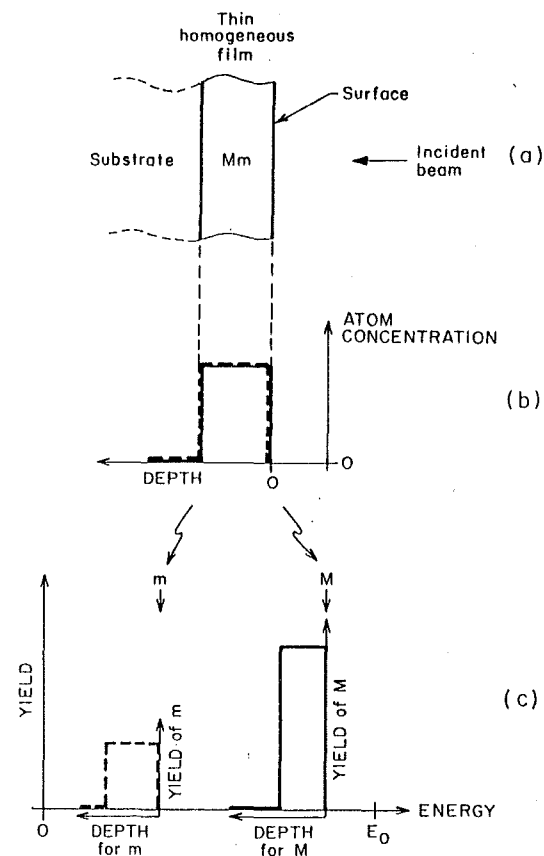


Fig. 1.13 (a) Translation of concentration profiles to signals in a backscattering spectrum, demonstrated for the example of a (thin homogeneous film of a binary compound with elements of a heavy M (solid line) and a light m (dashed line) atomic mass. (b) The atomic concentration profiles with depth are the same for both elements. (c) In the backscattering spectrum, the two profiles reappear as two separate signals. The position of the coordinate systems for the two signals, and the scaling factor for their ordinates are as described in Fig. 1.12. However, the conversion of the abscissas from depth to energy is generally not the same for the two signals, and the conversion is not exactly linear either. Usually, the nonlinearities are insignificant and the difference in the two scales is not more than 10%.

is reproduced independently of the other in the backscattering spectrum and generates the signal of that mass. The final backscattering spectrum is a linear superposition of these signals. When a concentration profile varies with depth, the height of a signal will vary accordingly. This means that a backscattering spectrum actually constitutes an image of the distribution with depth of the various elements in the sample. Each type of atom of a particular mass is displayed individually. The signal of each has an accurately defined position on the energy scale, which corresponds to the sample surface as a reference point.

If the sample of Figs. 1.12 and 1.13 is thick, the signals of the two masses M and m will extend down to zero energies. The spectrum then has the

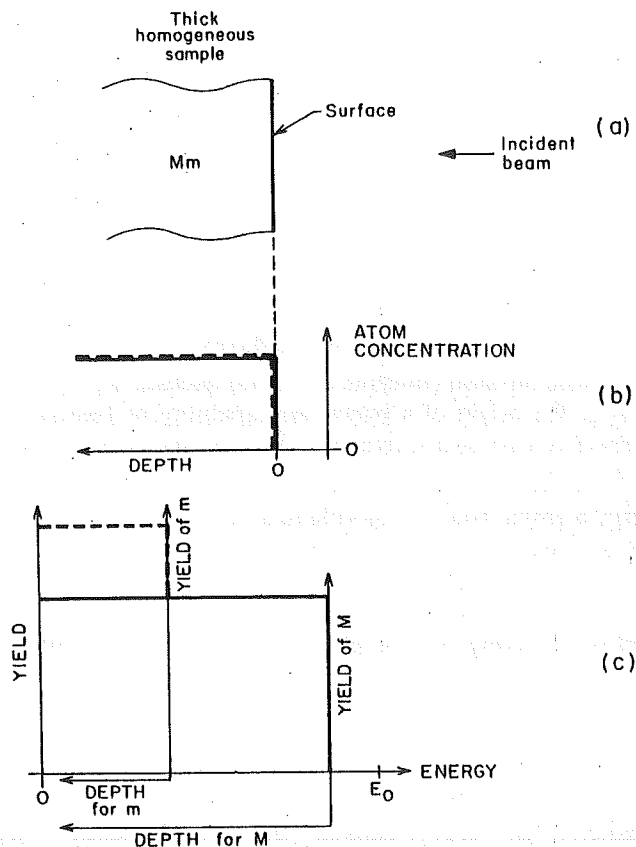


Fig. 1.14 (a) The signals of a thick sample extend all the way to zero energy. (b) Actual spectra never reach down to the origin of the energy axis, because near zero energy, the yield disappears in a large background of noise. (c) The construction of the spectrum follows exactly the same procedures outlined in Figs. 1.12 and 1.13.

steplike appearance shown in Fig. 1.14. Real spectra never extend to zero energy, because noise in the detection system dominates at these low energies and generates a huge background. Thick-target yields are also never flat-topped as shown here; the reason is the energy dependence of the scattering cross section.

In problems of analysis the situation is reversed. A backscattering spectrum is measured, and the elemental makeup of the sample with depth has to be determined. We shall treat more examples in Chapter 5 to illustrate some of the major characteristics of backscattering analysis. These examples will also demonstrate that backscattering spectrometry is, in essence, mass-sensitive depth microscopy capable of furnishing quantitative information on the sample under investigation.

1.7 BOOK OUTLINE

Starting with Chapter 2 we shall repeat the three basic concepts and their mathematical relations to the projectile and to the target parameters in detail. In addition to kinematics, scattering cross sections, and energy loss, we shall discuss energy straggling, which sets the ultimate limit on depth resolution.

Chapter 3 describes how the three basic concepts are combined to produce a backscattering spectrum. This concerns the relation of energy to depth. Also covered in the chapter is how the height of an energy spectrum is related to scattering cross section and energy loss. The emphasis in this chapter is on bulk samples.

Chapter 4 gives backscattering analyses of thin films of various degrees of complications: elemental films, multilayered elemental films, compound films, and layered compound films. Depth and composition analyses at various sophistication levels are given. Different approximations and their justification are also given.

Many examples of backscattering analysis are given in Chapter 5. Formulas developed in Chapters 3 and 4 are applied to real problems. Many examples were chosen to illustrate the capability and limitation of backscattering. Some of the approximations given in the previous two chapters are also used and compared to give the reader a feeling about the adequacy of the approximations. Since many of the examples have been taken from routine experiments, readers can use them as typical spectra to check their system and their analysis.

Chapter 6 describes the experimental setup. If you do not have a nuclear physics laboratory close by and want to set up a backscattering laboratory, this chapter gives the basic requirements for hardware and electronics. The

chapter is also useful in understanding the data-taking system: solid-state detector, preamp, amplifiers, multichannel analyzer, and so on.

Chapter 7 describes the influence of beam parameters. In all the discussions so far we emphasize megaelectron volt ^4He beams incident perpendicularly on the sample. In this chapter we discuss other alternatives. We shall present mass and depth resolutions and their relationships to the mass and energy of the projectiles. Different geometries for scattering and various problems are also discussed.

Chapter 8 is concerned with backscattering applications when combined with channeling effects. We start with the procedure used to align a crystal and then proceed to half-angle and minimum-yield calculations. The channeling applications dealing with lattice disorder, amorphous layers, and polycrystalline film are discussed. Lattice location and flux peaking of impurities in a crystal are also described.

In the body of the book, we assume that energy loss values are known in the analysis of a backscattering problem. In Chapter 9 we reverse the procedure and use the knowledge of the sample (composition and thickness) to determine stopping cross section values from backscattering measurements. Methods, formulas, and a few examples are given.

Chapter 10 gives a list of references on the applications of backscattering spectrometry. The cut-off date on the citations is August 1976. The references are listed according to various topics; surfaces, bulk, oxide and nitride layers, deposited and grown layers, thin film reactions, and ion implantation in metals and in semiconductors are the main section topics. Subdivision of the references by topic as well as listing the title of each paper provides a useful bibliography for a literature research.

In Appendix F, we provide tables of kinematic factors, scattering cross sections, and various forms of energy loss and energy loss factors. Analyses of examples given in the book are generated by using these tables.

REFERENCES

- Geiger, H., and Marsden, E. (1913). *Phil. Mag.* **25**, 606.
 Mazari, M., Velazquez, L., and Alba, F. (1959). *Revista Mexicana de Fisica* **VIII**, 1.
 Patterson, J. H., Turkevich, A. L., and Franzgrote, E. J. (1965). *J. Geophys. Res.* **70**, 1311.
 Rubin, S., Stanford Res. Inst. Tech. Rep., No. 1 (1954).
 Rubin, S., and Rasmussen, V. K. (1950). *Phys. Rev.* **78**, 83.
 Rubin, S., Passell, T. O., and Bailey, E. (1957). *Anal. Chem.* **29**, 736.
 Rutherford, E. (1911). *Phil. Mag.* **21**, 669.
 Sippel, R. F. (1959). *Phys. Rev.* **115**, 1441.
 Tollestrup, A. V., Fowler, W. A., and Lauritsen, C. C. (1949). *Phys. Rev.* **76**, 428.
 Turkevich, A. (1961). *Science* **134**, 672.
 Turkevich, A. L. *et al.* (1968). in Surveyor Project Final Report, Part II. Scientific Results, Nat. Aeronaut. and Space Administration Tech. Rep. 32-1265, pp. 303-387. Jet Propulsion Lab., California Inst. of Technol., Pasadena, California.

Basic Physical Concepts

2.1 INTRODUCTION

Only four basic physical concepts enter into backscattering spectrometry. Each one is at the origin of a particular capability or limitation of backscattering spectrometry and corresponds to a specific physical phenomenon. They are

1. Energy transfer from a projectile to a target nucleus in an elastic two-body collision. This process leads to the concept of the *kinematic factor* and to the capability of mass perception.
2. Likelihood of occurrence of such a two-body collision. This leads to the concept of *scattering cross section* and to the capability of quantitative analysis of atomic composition.
3. Average energy loss of an atom moving through a dense medium. This process leads to the concept of *stopping cross section* and to the capability of depth perception.
4. Statistical fluctuations in the energy loss of an atom moving through a dense medium. This process leads to the concept of *energy straggling* and to a limitation in the ultimate mass and depth resolution of backscattering spectrometry.

In this chapter an introductory treatment of these subjects is provided. Key formulas are given, and functional relationships are examined. The

discussion goes as far as the understanding of backscattering spectrometry demands. How these processes actually enter into a backscattering experiment and how they can affect a backscattering spectrum are examined in Chapter 3. When the target is a single crystal, or nearly so, the processes treated in this chapter are combined in a particular fashion, which results in the phenomenon of *channeling*. This effect is discussed in Chapter 8.

2.2 KINEMATIC FACTOR K

When a particle of mass M_1 , moving with constant velocity, collides elastically with a stationary particle of mass M_2 , energy will be transferred from the moving to the stationary particle. In backscattering analysis, mass M_1 is that of the projectile atom in the analyzing beam and mass M_2 is that of an atom in the target examined. The assumption that the interaction between the two atoms is properly described by a simple elastic collision of two isolated particles rests on two conditions:

(1) The projectile energy E_0 must be much larger than the binding energy of the atoms in the target. Chemical bonds are of the order of 10 eV, so that E_0 should be very much larger than that.

(2) Nuclear reactions and resonances must be absent. This imposes an upper limit to the projectile energy. Nuclear processes depend on the specific choice of projectile and target atoms, so that the upper limit of E_0 varies with circumstances. With a H^+ beam, nuclear effects can appear even below 1 MeV; with He^+ , they begin to appear at 2 to 3 MeV.

The simple elastic collision of two masses M_1 and M_2 can be solved fully by applying the principles of conservation of energy and momentum. Let v_0 , v_0 , and $E_0 = \frac{1}{2}M_1v_0^2$ be the velocity, its value, and the energy of a projectile atom of mass M_1 before the collision, while the target atom of mass M_2 is at rest. After the collision, let v_1 and v_2 be the velocities and $E_1 = \frac{1}{2}M_1v_1^2$ and $E_2 = \frac{1}{2}M_2v_2^2$ be the energies of projectile and target atoms, respectively. The notation and the geometry of this scattering problem are given in Fig. 2.1, where the scattering angle θ and the recoil angle ϕ are

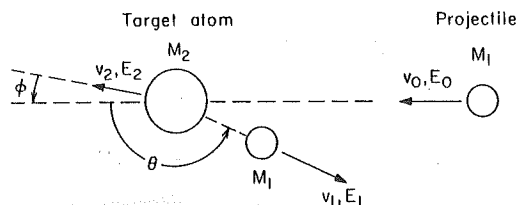


Fig. 2.1 Schematic representation of an elastic collision between a projectile of mass M_1 , velocity v_0 , and energy E_0 and a target mass M_2 which is initially at rest. After the collision, the projectile and the target mass have velocities and energies v_1 , E_1 and v_2 , E_2 , respectively. The angles θ and ϕ are positive as shown. All quantities refer to a laboratory frame of reference.

defined as positive numbers with the arrows as shown. All quantities refer to a laboratory system of coordinates.

Conservation of energy and conservation of momentum parallel and perpendicular to the direction of incidence are expressed by the equations

$$\frac{1}{2}M_1v_0^2 = \frac{1}{2}M_1v_1^2 + \frac{1}{2}M_2v_2^2, \quad (2.1)$$

$$M_1v_0 = M_1v_1 \cos \theta + M_2v_2 \cos \phi, \quad (2.2)$$

$$0 = M_1v_1 \sin \theta - M_2v_2 \sin \phi. \quad (2.3)$$

Eliminating ϕ first and then v_2 , one finds

$$v_1/v_0 = [\pm(M_2^2 - M_1^2 \sin^2 \theta)^{1/2} + M_1 \cos \theta]/(M_2 + M_1). \quad (2.4)$$

For $M_1 \leq M_2$ the plus sign holds. We now define the ratio of the projectile energy after the elastic collision to that before the collision as the *kinematic factor* K ,

$$K \equiv E_1/E_0. \quad (2.5)$$

From Eq. (2.4) one obtains

$$K_{M_2} = \left[\frac{(M_2^2 - M_1^2 \sin^2 \theta)^{1/2} + M_1 \cos \theta}{M_2 + M_1} \right]^2 \quad (2.6a)$$

$$= \left\{ \frac{[1 - (M_1/M_2)^2 \sin^2 \theta]^{1/2} + (M_1/M_2) \cos \theta}{1 + (M_1/M_2)} \right\}^2, \quad (2.6b)$$

where, following frequent practice, a subscript has been added to K to indicate the target mass M_2 for which the factor applies. Another custom uses the chemical symbol of the target atom as the subscript for K (e.g., K_{Si} instead of K_{28}). This procedure is less accurate, because elements can have isotopes, and isotopes have slightly different K values. In the center-of-mass system of reference, Eq. (2.6) can be simplified to (Marion and Young, 1968)

$$K = 1 - [2M_1M_2/(M_1 + M_2)^2](1 - \cos \theta_c), \quad (2.7)$$

where θ_c is the scattering angle in the center-of-mass coordinates.

The kinematic factor depends only on the ratio of the projectile to the target masses and on the scattering angle θ . The mass ratio M_1/M_2 will be abbreviated by x . A plot of K versus $M_2/M_1 = x^{-1}$ and θ as given by Eq. (2.6) is shown in Fig. 2.2. One sees that for any combination of projectile and target mass, i.e., for any value of x , K always has its lowest value at 180° . The value there is

$$K(\theta = 180^\circ) = [(M_2 - M_1)/(M_2 + M_1)]^2 = [(1 - x)/(1 + x)]^2. \quad (2.8)$$

At $\theta = 90^\circ$, K is

$$K(\theta = 90^\circ) = (M_2 - M_1)/(M_2 + M_1) = (1 - x)/(1 + x), \quad (2.9)$$

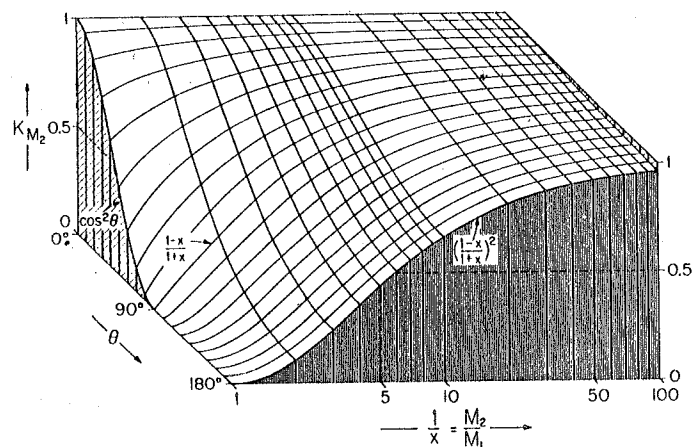


Fig. 2.2 The kinematic factor K of Eq. (2.6b) plotted as a function of the scattering angle θ and the mass ratio $x^{-1} = M_2/M_1$.

that is, the value of the kinematic factor at $\theta = 180^\circ$ is the square of its value at $\theta = 90^\circ$. When the projectile and the target mass are equal ($x = 1$), K is zero for angles larger than 90° and increases as $\cos^2 \theta$ when θ falls below 90° . This says that a projectile colliding with a stationary atom equal to its own mass cannot be scattered backward, but only forward. This is true also for $M_1 > M_2$ ($x > 1$).

In backscattering spectrometry, angles near 180° are of special interest. To describe the behavior of K there, it is convenient to introduce the difference δ between θ and 180° , expressed in units of radians of arc as

$$\delta = \pi - \theta, \quad (2.10)$$

so that δ measures the deviation of θ from π in units of arc. The kinematic factor then is approximated very well by the first term of an expansion in δ :

$$K \simeq \left(\frac{M_2 - M_1}{M_2 + M_1} \right)^2 \left(1 + \frac{M_1}{M_2} \delta^2 \right) = \left(\frac{1-x}{1+x} \right)^2 (1 + x \delta^2). \quad (2.11)$$

This equation describes the increase of K along the front edge of Fig. 2.2 for small decreases of θ from 180° . The approximation overestimates K by a relative amount which is less than $\delta^4 x (1-x)^{-2}$. As θ departs from 180° , K increases only quadratically with δ . This increase is proportional to the mass ratio $x = M_1/M_2$. When this ratio is small, the factor $[(1-x)/(1+x)]^2$ can be approximated by $1 - 4x$, so that in the right corner of Fig. 2.2 the kinematic factor is approximately described by

$$K \simeq 1 - 4x + \delta^2 x. \quad (2.12)$$

This is a convenient formula to estimate K in the region of θ and x values which are most relevant to backscattering spectrometry. Values of K and δ^2 are given in Tables II-V in Appendix F.

Equations (2.5) and (2.6) contain the essence of how backscattering spectrometry acquires its ability to sense the mass of an atom. Imagine that the primary energy E_0 of the projectile atom and its mass M_1 are known. Assume that the energy E_1 after the elastic scattering event is measured at a known angle θ . Then the mass M_2 of the target atom that prompted the scattering is the only unknown quantity in Eq. (2.6). The value of M_2 can thus be determined by measuring the energy E_1 after the collision if E_0 , M_1 , and θ are known. In effect, the technique amounts to mass spectrometry "by reflection." The method is based on the same laws that govern simple billiard ball physics.

In practice, when a target contains two types of atoms that differ in their masses by a small amount ΔM_2 , it is important that this difference produce as large a change ΔE_1 as possible in the measured energy E_1 of the projectile after the collision. As Fig. 2.2 shows, a change of ΔM_2 (for fixed M_1) gives the largest change of K when $\theta = 180^\circ$ for all but the smallest values of M_2 . Thus $\theta = 180^\circ$ is the preferred location for the detector. To place a normal detector exactly at $\theta = 180^\circ$ is not possible because the detector would obstruct the path of the incident particles. The detector is thus normally positioned at some steep backward angle, such as 170° . It is this particular experimental arrangement that has given the method its name of *backscattering* spectrometry. With annular detectors, scattering angles very near 180° can be reached; these special solid-state detectors have a hole along the center axis through which the primary beam passes before impinging on the target.

In quantitative terms, ΔE_1 and ΔM_2 are related to each other by

$$\Delta E_1 = E_0 (dK/dM_2) \Delta M_2. \quad (2.13)$$

In the vicinity of $\theta = 180^\circ$, i.e., $\theta = \pi - \delta$, K is very closely approximated by Eq. (2.11), so that

$$\frac{\Delta E_1}{E_0} = \frac{1-x}{(1+x)^3} [4(1+x\delta^2) - \delta^2(1-x^2)] x \frac{\Delta M_2}{M_2}. \quad (2.14)$$

For $M_2 \gg M_1$, which is most often the case, this reduces further to

$$\Delta E_1 = E_0 (4 - \delta^2) (M_1/M_2^2) \Delta M_2. \quad (2.15)$$

Every practical detection system has a finite resolution. If ΔE_1 falls below this limit, the distinction between two masses is lost. To obtain good mass resolution, it is therefore desirable that the coefficient of ΔM_2 be as large as

possible. To accomplish this, one can

- (i) Increase the primary energy E_0 ;
- (ii) Use a projectile of large mass M_1 (Note, however, that M_2 masses smaller than M_1 will not produce any backscattering signal.);
- (iii) Measure at scattering angles approximately 180° (small δ).

We also notice that mass resolution is inherently better for light target atoms than for heavy ones, the effect going as M_2^{-2} .

2.3 SCATTERING CROSS SECTION σ

The preceding section established the connection between the energy E_0 of the incident particle of mass M_1 and the energy $K_{M_2} E_0$ that this particle possesses at any angle θ after an elastic collision with an initially stationary mass M_2 . How frequently such a collision actually occurs and ultimately results in a scattering event at a certain angle θ remains open.

The differential scattering cross section $d\sigma/d\Omega$ is the concept introduced to answer this. Its definition is derived from a simple conceptual experiment. A narrow beam of fast particles impinges on a thin uniform target that is wider than the beam. At an angle θ from the direction of incidence, let an ideal detector count each particle scattered in the differential solid angle $d\Omega$ (see Fig. 2.3). If Q is the total number of particles that have hit the target and dQ is the number of particles recorded by the detector, then the *differential scattering cross section* $d\sigma/d\Omega$ is defined as

$$d\sigma/d\Omega = (1/Nt)[(dQ/d\Omega)/Q], \quad (2.16)$$

where N is the volume density of atoms in the target and t is its thickness. Thus Nt is the number of target atoms per unit area (areal density). The

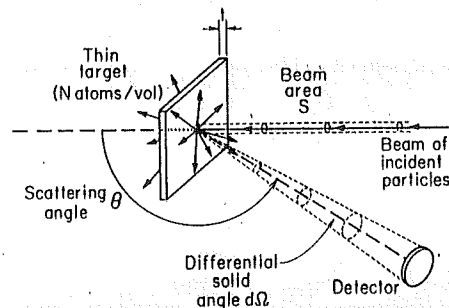


Fig. 2.3 Simplified layout of a scattering experiment to demonstrate the concept of the differential scattering cross section. Only primary particles that are scattered within the solid angle $d\Omega$ spanned by the detector are counted.

definition implies that the solid angle $d\Omega$ is so small that the scattering angle θ is well defined. The definition also assumes that the thickness t is minimal and that, therefore, the energy loss of the particles in the target is so small that the energy of the particles is virtually the same at any depth in the target. Finally, the total number of incident particles Q must be so large that the ratio dQ/Q has a well-determined value.

The differential scattering cross section $d\sigma/d\Omega$ has the dimension of an area ("cross section") whose meaning is based on a geometrical interpretation of the probability that the scattering will result in a signal at the detector. One imagines that each nucleus of an atom presents an area $d\sigma/d\Omega$ to the beam of incident particles. It is also assumed that this area is quite small and that the atoms within the target are randomly distributed in such a way that the differential cross sections $d\sigma/d\Omega$ of the nuclei do not overlap. Let S be the surface area of the target illuminated uniformly by the beam. Then the total number of atoms eligible for a scattering collision in the target is $S N t$.[†] The ratio of the total cross-sectional area of all eligible atoms $S N t d\sigma/d\Omega$ to the area S actually exposed is then interpreted as the probability that the scattering event will be recorded by the detector; that is, this ratio is set equal to $(1/d\Omega) dQ/Q$. Equation (2.16) then follows. The multiplication with $(d\Omega)^{-1}$ is introduced because doubling the solid angle $d\Omega$ would obviously double the number of counts dQ . By dividing dQ with $d\Omega$, this geometrical contribution to the number of counts dQ is eliminated. The cross section defined in this way thus becomes a value per unit of solid angle; hence the name *differential scattering cross section*, and therefore the notation $d\sigma/d\Omega$. Other equally valid interpretations of the meaning of a differential scattering cross section can be found in various textbooks (Leighton, 1959; Goldstein, 1959).

When one inquires as to the number of scattering events falling within a finite solid angle Ω rather than a differential solid angle $d\Omega$, the probability of a successful event is described by the *integral scattering cross section* Σ :

$$\Sigma = \int_{\Omega} (d\sigma/d\Omega) d\Omega. \quad (2.17)$$

Its geometrical interpretation is analogous to that of the differential scattering cross section. In backscattering spectrometry, the solid angle Ω of a typical detector system with a surface-barrier detector is fairly small (10^{-2} sr or less)

[†] One can also conceive of situations where the picture of randomly distributed cross sections over an area S and a uniform illumination of this area S by the incident particles breaks down. When the target is single-crystalline, the cross sections are clustered along sets of lines in space. If the incident particles move in a direction parallel to such lines, and if the flux of these particles is concentrated in the voids ("channels") surrounding these lines, the probability of a scattering collision is obviously reduced. This is the situation commonly referred to as "channeling" (see Chapter 8).

and the scattering angle θ is well defined. It is then convenient[†] to introduce the *average differential scattering cross section* σ :

$$\sigma \equiv (1/\Omega) \int_{\Omega} (d\sigma/d\Omega) d\Omega. \quad (2.18)$$

For very small detector angles Ω , $\sigma \rightarrow d\sigma/d\Omega$. The average differential scattering cross section is the value ordinarily used in backscattering spectrometry. It is usually called *scattering cross section* in the literature. We follow this convention.

For the experimental condition given in Fig. 2.4, in which a uniform beam impinges at normal incidence on a uniform target that is larger than the area of the beam, the *total number of detected particles* A can be written from Eqs. (2.16) and (2.18) as

$$A = \sigma\Omega \cdot Q \cdot Nt. \quad (2.19)$$

$$\left(\begin{array}{c} \text{number of} \\ \text{detected particles} \end{array} \right) = \sigma\Omega \cdot \left(\begin{array}{c} \text{total number of} \\ \text{incident particles} \end{array} \right) \cdot \left(\begin{array}{c} \text{number of target} \\ \text{atoms per unit area} \end{array} \right).$$

This equation shows that when σ and Ω are known and the numbers of incident and detected particles are counted, the number of atoms per unit area in the target, Nt , can be determined. The ability of backscattering spectrometry to provide quantitative information on the number of atoms present per unit area of a sample stems from Eq. (2.19) and the fact that the average scattering cross section σ of the elements is known quite accurately.

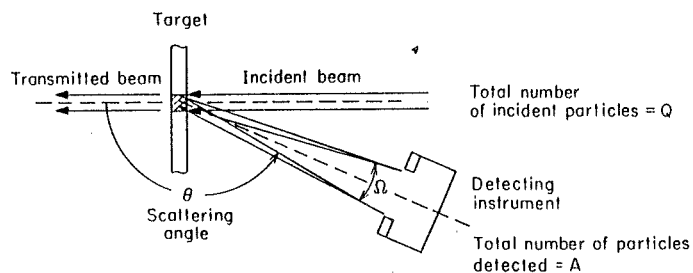


Fig. 2.4 Schematic layout of a backscattering experiment, showing a thin target, the transmitted portion of the beam, and the fraction of the backscattered beam that is intercepted and counted by the detector.

[†] In nuclear physics, the symbol σ is used to refer to the integral ("total") scattering cross section, called Σ in Eq. (2.17). The use of σ for the right-hand side of Eq. (2.18) is inconsistent with this older tradition, which would have required a symbol such as $\langle d\sigma/d\Omega \rangle$ instead. On the other hand, the newer (inconsistent) convention of Eq. (2.18) simplifies the writing of many equations to $\sigma\Omega$ rather than the clumsy $\langle d\sigma/d\Omega \rangle\Omega$.

To calculate the differential cross section for an elastic collision, the principles of conservation of energy and momentum must be complemented by a specific model for the force that acts during the collision between the projectile and the target masses. In most cases, this force is very well described by the Coulomb repulsion of the two nuclei as long as the distance of closest approach is large compared with nuclear dimensions, but small compared with the Bohr radius $a_0 = h/m_e e = 0.53 \text{ \AA}$. When these assumptions are made, the differential scattering cross section is given by Rutherford's formula (Rutherford, 1911; Goldstein, 1959; Leighton, 1959):

$$(d\sigma/d\Omega)_c = \left[\frac{Z_1 Z_2 e^2}{4E_c \sin^2(\theta_c/2)} \right]^2, \quad (2.20)$$

where the subscript c indicates that the values are given with respect to the center-of-mass coordinates. Here Z_1 is the atomic number of the projectile atom with mass M_1 , Z_2 is the atomic number of the target atom with mass M_2 , e is the electronic charge ($e = 4.80 \times 10^{-10} \text{ statC}$),[†] and E is the *energy of the projectile immediately before scattering*. This formula is valid also for values in the laboratory frame of reference, but only when $M_1 \ll M_2$. For the general case, the transformation of this formula from the center-of-mass to the laboratory frame of reference yields (Darwin, 1914)

$$\frac{d\sigma}{d\Omega} = \left(\frac{Z_1 Z_2 e^2}{4E} \right)^2 \frac{4}{\sin^4 \theta} \frac{\{ [1 - ((M_1/M_2) \sin \theta)^2]^{1/2} + \cos \theta \}^2}{[1 - ((M_1/M_2) \sin \theta)^2]^{1/2}}. \quad (2.22)$$

A detailed execution of this transformation is given in Appendix A. The order of magnitude of this differential scattering cross section is predominantly given by the first factor $(Z_1 Z_2 e^2 / 4E)^2$. As an example, consider 1-MeV He ($Z_1 = 2$) impinging on Ni ($Z_2 = 28$); then $(Z_1 Z_2 / 4)^2 = 196$. In electrostatic cgs units, the electronic charge has the value $e = 4.80286 \times 10^{-10} \text{ statC}$ and the unit of potential is the statV = 299.79 V. For 1 MeV, the value of $(e^2/E)^2$ is therefore $(e/10^6 \text{ V})^2 = (4.80286 \times 10^{-10} \times 299.79/10^6)^2 (\text{statC})^2 / (\text{statV})^2 = 2.0731 \times 10^{-26} (\text{statC}/\text{statV})^2$. The ratio $\text{statC}/\text{statV}$ has the value of the

[†] It is customary in the nuclear physics literature to use cgs units. To avoid confusion and to help in identifying the system of units adopted for an equation, we shall use e throughout when electrostatic units are assumed and q throughout when mks units are used. To translate an equation from one set of units to another, one substitutes

$$e^2 \rightleftharpoons q^2 / 4\pi\epsilon_0 \quad (2.21)$$

where $e = 4.80286 \times 10^{-10} \text{ statC}$, where $q = 1.60206 \times 10^{-19} \text{ C}$, and $\epsilon_0 = 8.85434 \times 10^{-12} \text{ Asec/V m}$. A convenient constant to remember in connection with Eq. (2.21) is that $e^2 = 1.4398 \times 10^{-13} \text{ MeV cm} \approx 1.44 \times 10^{-13} \text{ MeV cm}$. This permits quick estimates of $d\sigma/d\Omega$ when E is given in mega electron volts, as usual.

unit length 1 cm, so that $(e^2/E)^2 = 2.0731 \times 10^{-26} \text{ cm}^2 = 0.020731 \text{ b}$. Note that the conversion $e^2 = 1.4398 \times 10^{-13} \text{ MeV cm}$ yields this result directly. The product $(Z_1 Z_2/4)^2 \cdot (e^2/E)^2$ thus is $196 \times 0.020731 \text{ b} = 4.06328 \text{ b}$ for a unit steradian. Performed in mks units, the same calculation starts from the formula $(Z_1 Z_2 q^2/4\pi\epsilon_0 4E)^2$, where the electronic charge has the value $q = 1.60206 \times 10^{-19} \text{ A sec}$ and $\epsilon_0 = 8.85434 \times 10^{-12} \text{ A sec/V m}$. The ratio $(q^2/4\pi\epsilon_0 E)^2$ for $E = 10^6 \text{ qV}$ then becomes $(1.60206 \times 10^{-19}/4\pi \times 8.85434 \times 10^{-12} \times 10^6)^2 (\text{A sec})^2/(\text{A sec/V m})^2 = 2.0731 \times 10^{-30} \text{ m}^2$, which is again 0.020731 b . (1 b = 1 barn = 10^{-24} cm^2)

If we disregard the factor $(Z_1 Z_2 e^2/4E)^2$, the Rutherford differential scattering cross section depends only on the ratio M_1/M_2 of the projectile and target masses and on the scattering angle θ . A plot of $d\sigma/d\Omega$ versus $M_2/M_1 = x^{-1}$ and θ as given by Eq. (2.22) is shown in Fig. 2.5. For any combination of projectile and target mass, $d\sigma/d\Omega$ always has its lowest value at 180° . Expressed in units of $(Z_1 Z_2 e^2/4E)^2$, this minimum value is $[1 - (M_1/M_2)^2]^2 = (1 - x^2)^2$. In the vicinity of 180° , i.e., along the front edge of Fig. 2.5, where $\theta = \pi - \delta$, the Rutherford differential cross section increases quadratically with δ :

$$(d\sigma/d\Omega)/(Z_1 Z_2 e^2/4E)^2 = (1 - x^2)^2 + \frac{1}{2} b \delta^2, \quad (2.23)$$

where $b = 1 - 3x^4 + 2x^6$. The formula shows that near 180° , the scattering cross section does not change much with the scattering angle. This fact enables one to use the average acceptance angle of the particle detector and still obtain an accurate value for the calculated cross section near 180° [see

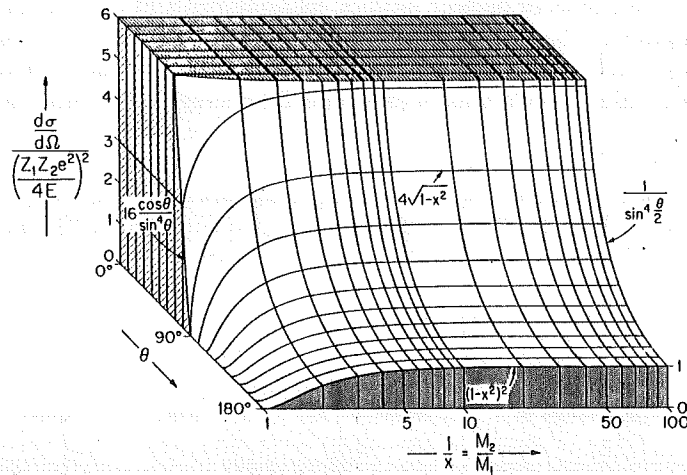


Fig. 2.5 The dependence of the Rutherford differential scattering cross section given by Eq. (2.22) as a function of the scattering angle θ and the mass ratio $x^{-1} = M_2/M_1$.

Eq. (2.18)]. For $M_1 \ll M_2$, i.e., in the lower right corner of Fig. 2.5, the angular dependence of the right-hand side of Eq. (2.22) can be expanded in the power series (Marion and Young, 1968)

$$\frac{d\sigma}{d\Omega} \approx \left(\frac{Z_1 Z_2 e^2}{4E} \right)^2 \left[\sin^{-4} \frac{\theta}{2} - 2 \left(\frac{M_1}{M_2} \right)^2 + \dots \right], \quad (2.24)$$

where the first omitted term is of the order of $(M_1/M_2)^4$. The last expression reveals the significant functional dependences of the Rutherford differential scattering cross sections:

(i) $d\sigma/d\Omega$ is proportional to Z_1^2 . The backscattering yield obtained from a given target atom with a He beam ($Z_1 = 2$) is four times as large as with a proton beam ($Z_1 = 1$) but only a ninth of that produced by a carbon beam ($Z_1 = 6$).

(ii) $d\sigma/d\Omega$ is proportional to Z_2^2 . For any given projectile, heavy atoms are very much more efficient scatterers than light atoms. Therefore, backscattering spectrometry is much more sensitive to heavy elements than to light ones.

(iii) $d\sigma/d\Omega$ is inversely proportional to the square of the projectile energy ($\propto E^{-2}$). The yield of scattered particles rises rapidly with decreasing bombarding energy.

(iv) $d\sigma/d\Omega$ is axially symmetrical with respect to the axis of the incident beam; i.e., $d\sigma/d\Omega$ is a function of θ only.

(v) $d\sigma/d\Omega$ is approximately inversely proportional to the fourth power of $\sin(\theta/2)$ when $M_1 \ll M_2$. This dependence gives rapidly increasing yields as the scattering angle θ is reduced.

Values of $d\sigma/d\Omega$ for various elements Z_2 and energies are tabulated in Table X. For He in the MeV energy range, Rutherford differential scattering cross sections are typically within an order of magnitude or two of barns ($1 \text{ b} = 10^{-24} \text{ cm}^2$) per unit steradian. A monolayer of a solid typically contains about 10^{15} atoms/cm². A 1-MeV He particle will thus typically traverse very many monolayers before being scattered out of its path by a nuclear collision.

Deviations of the differential scattering cross section from the Rutherford formula do exist.

For $\theta \rightarrow 0$, the Rutherford cross section tends to infinity, which of course violates the initial assumption that the cross sections of the target nuclei should be so small that they do not overlap. Small scattering angles correspond to large fly-by distances between the projectile and the target nuclei, that is, distances greater than the radius of the innermost electron shell of the target atom. At these distances the electrostatic interaction does not take place between bare nuclei as Rutherford's formula assumes ($d\sigma/d\Omega \approx Z_1 Z_2 e^2$).

A similar situation exists when a low-energy projectile collides with a heavy atom. In such instances, one must use scattering cross sections derived from a potential which includes electron screening. Examples are the Born potential (Everhart *et al.*, 1955), the Born-Mayer potential (Abrahamson, 1969; Robinson, 1974) or the Firsov potential (Firsov, 1959). The validity of the Rutherford scattering approximation has been tested by calculation using different potentials (Everhart *et al.*, 1955) and by measurements with 100-keV $^1\text{H}^+$ and $^4\text{He}^+$ on Au (Van Wijngaarden *et al.*, 1970). Barely detectable departure from the Rutherford differential cross section was obtained in the latter case.

For sufficiently high energies E , the distance of closest approach between the projectile and the target nuclei reduces to the dimensions of nuclear sizes. The short-range nuclear forces then begin to influence the scattering process, and deviations from the Rutherford scattering cross sections appear. When the scattering process is inelastic, the energy of the scattered particle differs from KE_0 as well. In other cases, the scattering process is elastic still, but the differential scattering cross section departs from the Rutherford value, sometimes by a large factor. In either case, the value of the differential scattering cross section is strongly dependent on energy, on the scattering angle, and on the particular combination of projectile and target nuclei.

Apparent deviations from the Rutherford differential cross section can occur with electrostatic and magnetic analyzers. These analyzers are often desirable at low energies because of their good resolution and precision. In contrast to solid-state detectors, however, they detect particles of only one charge state at a time. The charge of the projectile atom after backscattering and escape from the target is a strong function of the escape velocity of the projectile (Marion and Young, 1968). Adjustments are therefore required to correct the observed particle counts for the undetected fraction of the scattered particles at any given energy for a given target.

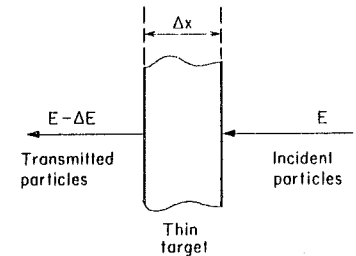
2.4 ENERGY LOSS AND STOPPING CROSS SECTION

2.4.1 Energy Loss dE/dx

An energetic particle that impinges on a target will penetrate into it. This is so because the large-angle Rutherford scattering collision discussed in the previous section is highly unlikely. The fate of an impinging particle is overwhelmingly determined by the processes that control the penetration into the target, rather than by the large-angle scattering collisions. Backscattering spectrometry is an analytical method to secondary process; the first-order process is the implantation of the beam particles into the target.

The concepts used to describe how a swift particle penetrates into matter arise from energetic considerations. As the particle pushes its way through

Fig. 2.6 Schematic of a transmission experiment to measure the $\Delta E/\Delta x$ loss of a swift particle in a dense medium.



the target, it slows down and its kinetic energy $E = \frac{1}{2}M_1v^2$ decreases. The amount of energy ΔE lost per distance Δx traversed depends on the identity of the projectile, on the density and composition of the target, and on the velocity itself. The simplest experiment that can be conceived to determine this energy loss is to take a very thin target of thickness Δx and of known composition. A beam of monoenergetic particles is directed at this target (see Fig. 2.6). The energy difference ΔE of the particles before and after transmission through the target is measured. The energy loss per unit length, also called sometimes the *specific energy loss*, and frequently abbreviated dE/dx loss, at the energy E of the incident beam is then defined as

$$\lim_{\Delta x \rightarrow 0} \Delta E/\Delta x \equiv \frac{dE}{dx}(E) \quad (2.25)$$

for that particular particle and energy in that medium. Note that this expression gives an energy loss that is a positive quantity.

Since the early days of nuclear physics, measurements of the energy loss per unit length have been performed for many projectile atoms, for a multitude of compounds, for most elements, and over a very wide range of energies. A list of available compilations of experimental energy loss information is given in Appendix D. For backscattering spectrometry, it is the energy loss of ^4He in the elements at energies between 0.5 and 3 MeV that is of chief concern, because beams of ^4He in that energy range are most frequently used. Typical dE/dx values for ^4He of that energy range lie between 10 and 100 eV/Å. Additional information on the subject is provided in Section 2.4.2.

For the present we shall assume that dE/dx is known at any energy, and we wish to establish the energy E of the projectile at any depth x below the surface of a thick sample into which the particle penetrates with an initial energy E_0 . Generally, dE/dx is a function of energy and has the form sketched in Fig. 2.7a. The energy E at any depth x below the surface is then given by

$$E(x) = E_0 - \int_0^x (dE/dx) dx. \quad (2.26)$$

As the functional parentheses (E) in Eq. (2.25) point out, dE/dx is defined and normally given as a function of E , not of x . The preceding integral thus

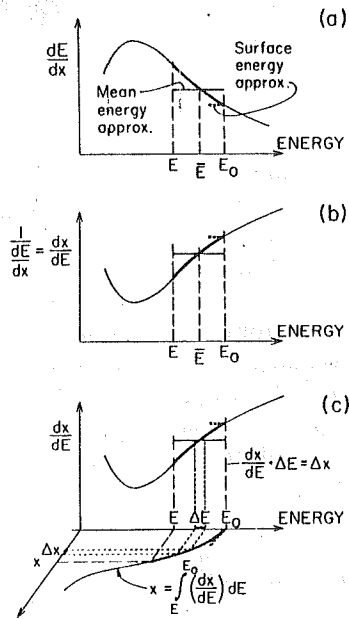


Fig. 2.7 (a) Typical dependence of dE/dx as a function of the kinetic energy E of the projectile. To obtain the depth of penetration x at which the particle energy has been reduced from E_0 to $E < E_0$, one takes the reciprocal of dE/dx , as shown in (b), and integrates this function from E to E_0 , as represented in (c). In the surface energy approximation, dE/dx is replaced by its value at E_0 (heavy dashed line). In the mean energy approximation, the constant value of dE/dx is chosen at the mean energy $\bar{E} = \frac{1}{2}(E + E_0)$.

cannot be evaluated without the knowledge of the energy as a function of x , $E(x)$. But $E(x)$ is the unknown in the equation. The difficulty is resolved by regarding x as a function of E , rather than E as a function of x ; then

$$dx = \frac{dx}{dE}(E) \cdot dE, \quad (2.27)$$

so that

$$x = \int_E^{E_0} (dx/dE) dE = \int_E^{E_0} (dE/dx)^{-1} dE. \quad (2.28)$$

To find $x(E)$, one thus integrates over the function $(dE/dx)^{-1}$. The situation is sketched graphically in Figs. 2.7b and c. Note that the upper limit E_0 is fixed and the lower limit E varies; hence x increases as E decreases.

It is frequently convenient to replace the actual dE/dx function by an approximation. The simplest procedure is to replace dE/dx by its value at the energy E_0 of the incident particle, as indicated by the dashed line in Fig. 2.7. Either Eq. (2.26) or Eq. (2.28) can then be used to determine $x(E)$:

$$E = E_0 - \frac{dE}{dx} \Big|_{E_0} x \quad \text{or} \quad x = (E_0 - E) \left(\frac{dE}{dx} \right)^{-1} \Big|_{E_0} \quad (2.29)$$

This method provides good estimates only in the uppermost or surface region of the target, and is thus called the *surface energy approximation*.

Another approximation replaces dE/dx by its value at the energy $\bar{E} = \frac{1}{2}(E + E_0)$. One then obtains, from Eq. (2.26) or Eq. (2.28),

$$E = E_0 - \frac{dE}{dx} \Big|_{\bar{E}} x \quad \text{or} \quad x = (E_0 - E) \left(\frac{dE}{dx} \right)^{-1} \Big|_{\bar{E}}, \quad (2.30)$$

so that x again increases linearly with $(E_0 - E)$. This procedure is called the *mean energy approximation* and is sketched in Fig. 2.7 as well. The mean energy approximation provides good estimates at intermediate depths of penetration. Figure 2.7c shows how the two approximations are related to the exact solution given by Eq. (2.28).

The accuracy of the linear approximation can obviously be increased by selecting the specific value for dE/dx that reproduces the magnitude of x when this specific value is substituted for the integrand in Eq. (2.28). The dE/dx curve takes on this specific value at some suitably selected energy \bar{E} intermediate to E and E_0 . As an example, Warters (1953) assumes that the functional dependence of dE/dx can be approximated by

$$dE/dx = CE^{-a(E)}, \quad (2.31)$$

where C is a constant and the exponent $a(E)$ varies only slowly, so that it may be set to a fixed value for any given energy interval $\Delta E = E_0 - E$. According to Eqs. (2.28) and (2.30), the specific value \bar{E} to choose is that which will satisfy the condition

$$\Delta x = \int_{E_0 - \Delta E}^{E_0} dE/CE^{-a} = \Delta E/CE^{-a}. \quad (2.32)$$

The integration over dE yields, as the condition that \bar{E} must meet,

$$(a + 1)^{-1} E_0^{a+1} \{1 - [1 - (\Delta E/E_0)]^{a+1}\} = \Delta E \bar{E}^a. \quad (2.33)$$

Expanding the left-hand side to second orders of $\Delta E/E_0$, dividing by E_0^a , and extracting the root gives

$$[1 - \frac{1}{2}a(\Delta E/E_0)]^{1/a} = \bar{E}/E_0 \quad (2.34)$$

or

$$\bar{E}/E_0 = 1 - \frac{1}{2}(\Delta E/E_0) + \dots \quad (2.35)$$

To the extent that Eq. (2.31) approximates dE/dx adequately and as long as $\Delta E \ll E_0$, the best choice of \bar{E} is thus midway between E_0 and $E_0 - \Delta E$. This is the same value specified in the mean energy approximation.

2.4.2 Stopping Cross Section ϵ

The energy loss dE/dx accounts for the energy a fast particle expends as it passes through the electron cloud of the atoms that lie along its path or as it suffers numerous small-angle collisions with nuclei lying along its route. The value of dE/dx can be viewed as an average over all possible energy-dissipative processes activated by the projectile on its way past a target atom. It is natural, then, to interpret dE/dx as the result of independent contributions of every atom exposed to the beam. This number is $S N \Delta x$ if Δx is the thickness of the target, S is the target area illuminated by the beam, and N the atom density in the target. The projection of all these atoms on the area S produces a surface density of atoms $S N \Delta x / S = N \Delta x$. This quantity increases linearly with Δx , as does the energy loss $\Delta E = (dE/dx) \Delta x$. We therefore set ΔE proportional to $N \Delta x$ and define the proportionality factor as the *stopping cross section* ϵ :

$$\epsilon \equiv (1/N)(dE/dx). \quad (2.36)$$

The conventional unit for ϵ is electron volts · square centimeters per atom usually abbreviated eV cm^2 .

The distinction between dE/dx and ϵ is most evident when one considers two targets made up of the same number of atoms per unit area. Assume that in one case the atoms are closely packed and form a high volume density. In the other case they are loosely assembled in a spongelike structure of low volume density. The energy ΔE transferred to the target by a fast particle must be the same in both cases as long as the energy loss is an atomic property, that is, independent of the packing density of the atoms. A larger value of dE/dx will be assigned to the denser target, however, because that energy ΔE is deposited over the shorter distance Δx . But $\Delta E / N \Delta x$ has the same value in both instances since the difference in the densities is caused by the different values of Δx in the two cases; in other words, $N \propto 1/\Delta x$, so that $N \Delta x = \text{const}$. Hence $\Delta E / N \Delta x = \epsilon$ is constant in the two cases. The subject is discussed also in Section 3.9.

Another definition which is used predominantly in the nuclear physics literature sets

$$\epsilon^* \equiv (1/\rho)(dE/dx), \quad (2.37)$$

where ρ is the mass density (grams per cubic centimeter) of the target and ϵ^* is usually given in units of kiloelectron volts · square centimeters per gram. The symbol ϵ^* is introduced here to distinguish between the two definitions of Eqs. (2.36) and (2.37), but the literature does not make that differentiation. Which definition applies in a particular case can always be established from dimensional considerations. The two quantities can be converted into each

2.4 Energy Loss and Stopping Cross Section

other by the relationship

$$\rho = N(M/N_0), \quad (2.38)$$

so that $\epsilon^* = \epsilon N_0 / M$. Here M is the atomic weight (grams per mole) of the element and $N_0 = 6.025 \times 10^{23}$ atoms/mole is Avogadro's number.

The advantage of using the stopping cross section ϵ rather than the dE/dx is evident when one compares the energy loss of neighboring elements in the periodic table. Table 2.1 lists data for Na and Al for 2-MeV ^4He . The ratios of the atomic numbers Z_2 and of the atomic masses M_2 are within 4% of the ϵ ratio, but the dE/dx ratio is larger by more than a factor of two. It is mainly the difference in the atomic density of Na and Al that is responsible for this difference. Atomic densities vary over almost an order of magnitude. Interpolations from one element to another are thus much more reliably performed on ϵ than on dE/dx when direct information is unavailable.

TABLE 2.1
Comparison of Energy Loss per Unit Length dE/dx and
Stopping Cross Section ϵ for 2.0-MeV ^4He in Na and Al

	Z_2	M_2	N (atoms/cm ³)	ϵ (eV cm ²)	dE/dx (eV/Å)
Na	11	22.99	2.65×10^{22}	39.6×10^{-15}	10.5
Al	13	26.98	6.02×10^{22}	44.3×10^{-15}	26.6
$\frac{\text{Al}}{\text{Na}}$ ratio	1.18	1.17	2.27	1.12	2.53

For backscattering spectrometry, interest in stopping cross-section values centers predominantly on ^4He because this is the most frequently used ion for the analyzing beam. Ziegler and Chu (1974) have surveyed the literature and tabulated semiempirical tables of stopping cross sections for ^4He in all elements and from 0.4 to 4.0 MeV. Their tables are reproduced as Table VI of Appendix F. A graphical display of the values from 0.4 to 2.0 MeV is shown in Fig. 2.8. As can be seen, the stopping cross section of all elements vary with energy in much the same way. The curves have a broad maximum somewhere near 1 MeV. For constant energy, ϵ tends to increase with Z_2 , but there are strong variations superimposed on this trend. In their fine structure these variations are irregular, but their overall features are closely correlated with the electronic configuration of the element. This is particularly pronounced at 400 keV, where the three transition metal groups show up as regions of reduced ϵ values.

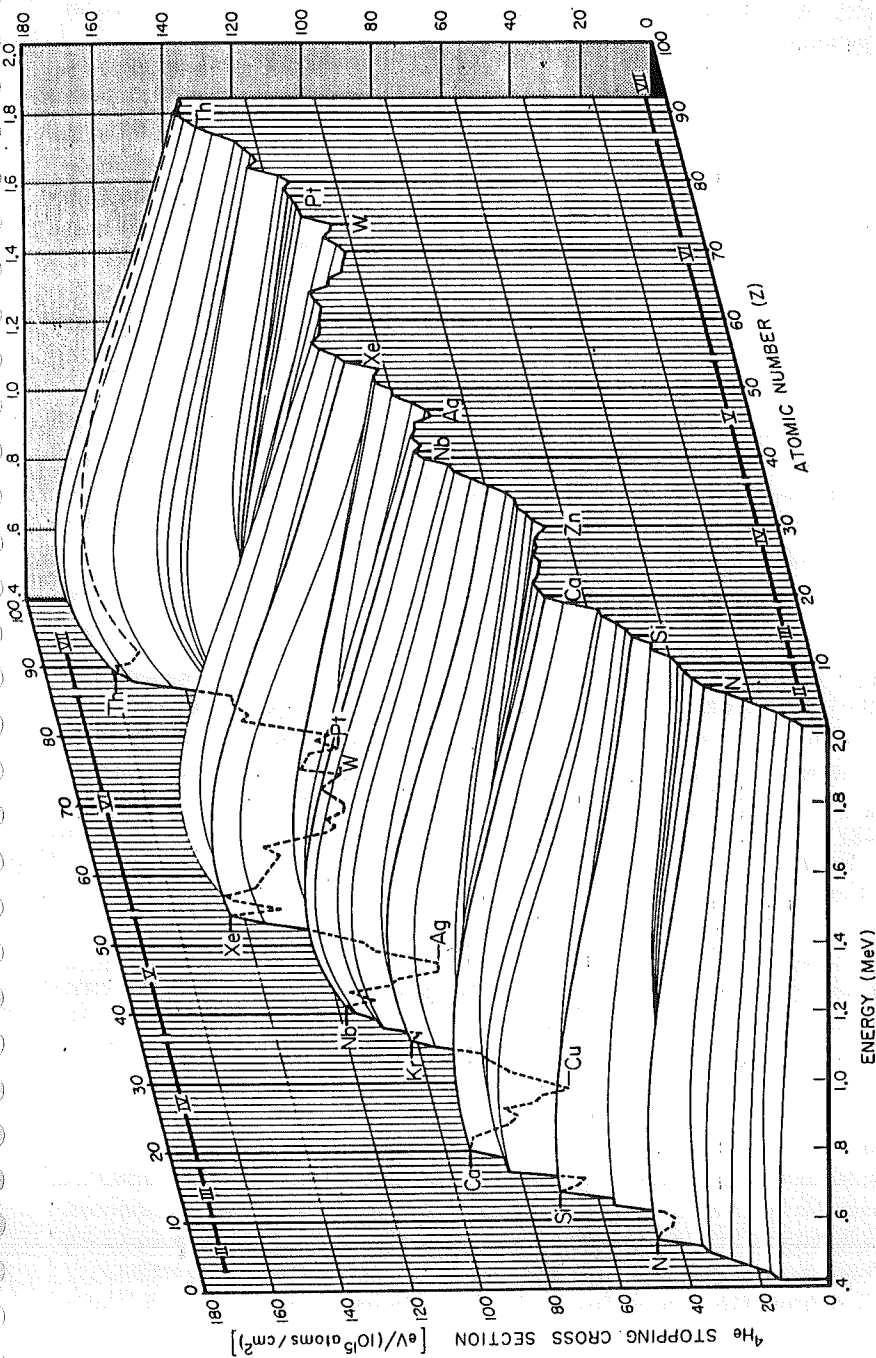


Fig. 2.8 Stopping cross sections for ${}^4\text{He}$ in all elements from 0.4 to 2.0 MeV. The plot gives the semiempirical values of the tables of Ziegler and Chu (1974), here reproduced as Table VI in Appendix F.

Many sections of this figure have been obtained by interpolation to fill in nonexistent data, and some of the data available may be revised in the future. Details in Fig. 2.8 will then change; but it is clear that as a whole the dependence of the stopping cross section on energy and target element in the range of interest to backscattering spectrometry is complicated. This is the reason why theoretical calculations of stopping cross sections turn out to be difficult to do accurately. The following subsection therefore presents in detail only the simplest classical picture of electronic energy loss. The approach offers some physical insight but no quantitative accuracy.

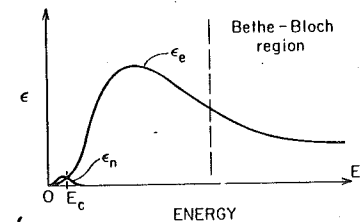
2.4.3 Physical Models

The theory of the fast particle interaction in dense media began with the work of Bohr (1913) and is still an active field of investigation. Much is now known, particularly for amorphous materials. For the light projectile atoms and the energy range of interest to backscattering spectrometry, the two dominant processes of energy loss are the interactions of the moving ion with the bound or free electrons in the target, and the interactions of the moving ion with the screened or unscreened nuclei of the target atoms. One can thus set

$$\varepsilon = \varepsilon_e + \varepsilon_n. \quad (2.39)$$

Figure 2.9 shows schematically how these two contributions depend on the projectile energy. Nuclear stopping originates from the multitude of small-angle scattering collisions of the projectile with the atomic nuclei of the target. Electronic stopping comes from the "frictional resistance" that the projectile encounters on its pass through the electron clouds surrounding each target atom.

Fig. 2.9 Typical dependences of electronic ε_e and nuclear ε_n contributions to the stopping cross section ε as a function of the incident particle energy E . The Bethe-Bloch equation [Eq. (2.46)] is a good approximation only at high energies beyond the maximum in the stopping cross section.



In very simplified terms, both interactions may be viewed as taking place between two isolated particles that interact electrostatically. Assume that the direction and speed of the incident particle are perturbed only slightly by the interaction. If the projectile has a mass M_1 , a charge Z_1e , and a velocity v_1 , and if the target particle of mass M_2 and charge Z_2e is initially stationary, then the momentum transferred to the mass M_2 in a direction perpendicular

to the path of the projectile is

$$P_{\perp} = 2(Z_1 Z_2 e^2 / b v_1) \quad (2.40)$$

for this simplified model. Here, the *impact parameter* b is the distance of closest approach between the two particles if the mass M_2 were held fixed in place while the projectile flew past it along a straight trajectory. The energy transferred to the stationary particle thus is

$$E_{\perp} = P_{\perp}^2 / 2M_2 \quad (2.41)$$

$$= (2/M_2)(Z_1 Z_2 e^2 / b v_1)^2. \quad (2.42)$$

The energy lost by the projectile is very closely equal to E_{\perp} when the perturbation is small, as presently assumed. It is thus evident that electrons with their light mass ($M_2 = m_e$) absorb much more energy per encounter than the nuclei do.

From this value of E_{\perp} one can readily obtain the electronic energy loss ΔE incurred by the projectile over a length Δx of the target. Statistically, the probability of an encounter with the impact parameter between b and $b + db$ is $2\pi b db$ per unit area, since the electron may lie anywhere on a circle of radius $2\pi b$ around the particle track. The number of electrons per unit area over the length Δx of the track is $N Z_2 \Delta x$. The average number $d\Delta n(E_{\perp})$ of encounters that will generate a quantum E_{\perp} of energy loss is therefore

$$d\Delta n(E_{\perp}) = N Z_2 \Delta x \cdot 2\pi b db. \quad (2.43)$$

Together, these losses contribute the average differential amount $d\Delta E$ to the total energy loss ΔE across Δx ; hence,

$$d\Delta E = N Z_2 \Delta x [2(Z_1 e^2)^2 / m_e v_1^2] 2\pi (db/b). \quad (2.44)$$

If the impact parameter can range from b_{\min} to b_{\max} , and Δx tends to the limit $d\Delta x$, one finds after integration:

$$(dE/dx)|_e = N Z_2 [4\pi(Z_1 e^2)^2 / m_e v_1^2] \ln(b_{\max}/b_{\min}). \quad (2.45)$$

This result closely matches the Bethe-Bloch formula (2.46).

This simple picture of scattering in a cloud of free electrons neglects the fact that electrons are bound to atomic nuclei. Even in a metal, most electrons are bound to atoms. The ionization energy required to separate the electron from the atom has to be accounted for, and the scattering process becomes an inelastic one. The correct calculation of the average energy transferred to an electron is thus a problem for which we must consider every possible energetic state of an electron in the target and which depends additionally on the average population of each of these states. Also, the problem has to be treated quantum mechanically.

A number of approximations have been developed over the years to perform this averaging. They provide very useful analytical expressions for

$dE/dx|_e$. A well-known result is that the electronic stopping can be cast in the general form

$$(dE/dx)|_e = N Z_2 [4\pi(Z_1 e^2)^2 / m_e v_1^2] L, \quad (2.46)$$

where L is called the *stopping number*. According to quantum-mechanical calculations of Bethe (1930), its value is given by

$$L = \ln(2m_e v_1^2 / I), \quad (2.47)$$

where the energy I is an average over the various excitations and ionizations of the electrons in a target atom. Exact calculations of this *mean excitation potential* are difficult to perform, and I is usually regarded as an empirical parameter. Bloch (1933) also made a quantum mechanical analysis and showed that I is approximately proportional to Z_2 ; that is, $I = K Z_2$, where K is an empirical parameter known as *Bloch's constant* and is of the order of approximately 10 eV. Equation (2.46) is commonly referred to as the Bethe-Bloch formula for the specific energy loss. The formula describes the experimental energy loss well only at energies beyond the maximum of the dE/dx curve (see Fig. 2.9). Equations (2.46) and (2.47) state that for any elemental target the electronic component of dE/dx has the generic form

$$\left\{ \begin{aligned} dE/dx|_e &= N Z_2 (Z_1 e^2)^2 f(v_1^2) \\ &= N Z_2 (Z_1 e^2)^2 f(E/M_1), \end{aligned} \right. \quad (2.48)$$

$$\left. \right\} \quad (2.49)$$

where $f(E/M_1)$ is a function that depends only on the target element, not on the type of projectile, and also describes the energy dependence of $dE/dx|_e$. Equation (2.49) states that dE/dx is proportional to the atomic density N (as discussed in connection with Table 2.1). The equation also states that in any given element the electronic energy loss of ${}^4\text{He}$ ($M_1 = 4$, $Z_1 = 2$) at an energy E is four times larger than the energy loss of protons at an energy $E/4$. Neither statement is exactly correct, but both are very useful rules.

Electronic stopping depends on the electronic states in the target so that, in principle, the gaseous, liquid, and solid phases of the same element must have different stopping cross sections. The nature of the chemical binding in a target affects the electronic states and should thus also affect electronic stopping. Such effects, although they have been reported (Matteson *et al.*, 1976) are weak. They are ignored in the theoretical treatments previously discussed. These effects are expected to be significant mainly at low projectile energies and for light targets, where the number of core electrons are few. One theoretical model of $dE/dx|_e$ actually assumes that the valence electrons may be treated as a Fermi gas with a plasma frequency $\omega_p = (4\pi n_e e^2 / m_e)^{1/2}$, where n_e is the density of the electron gas (Lindhard *et al.*, 1964). The analysis, performed in terms of a complex dielectric constant, again leads to Eq. (2.46) for high energies, where $N Z_2$ stands for n_e and L now has the value $\ln(2m_e v_1^2 / \hbar \omega_p)$. Recent calculations based on wavefunctions of a Hartree-Fock-Slater

model have proven fruitful in explaining the systematic variations of $dE/dx|_e$ with Z_2 for a fixed projectile (Rousseau *et al.*, 1971; Chu and Powers, 1972), as shown for ${}^4\text{He}$ in Fig. 2.8. The rather remarkable decrease in the stopping cross section shown in Fig. 2.8 from Ca to Cu, Nb to Ag, and past Xe is due to the fact that when d -shell electrons are added in the sequence of transition elements, the electron density near the atom increases enough to reduce the average electron density seen by an energetic particle traversing the material.

As long as the particle moves through matter so fast that the velocity v_1 is large compared with the speed $Z_1 v_0$ of its electrons in their innermost orbit, where $v_0 = e^2/\hbar = 2.2 \times 10^8$ cm/sec, the particle is effectively stripped of electrons and moves as an ion through the medium. At these velocities the simple model of charge $Z_1 e$ interacting elastically (or inelastically) with free (or bound) electrons in the target applies [Eq. (2.49)]. As the particle slows down, however, the probability that an electron is captured by the moving ion increases (Bohr, 1940, 1941; Northcliffe, 1960) and the effective charge of the projectile decreases. Also, the most tightly bound electrons of the target atoms play a gradually declining role in the stopping process. As a result, $dE/dx|_e$ increases less rapidly with falling energy E , and eventually turns around and actually decreases. The maximum of the stopping curve lies in the general vicinity of the "Thomas-Fermi" velocity $Z_1^{2/3} v_0$ and usually somewhat above it. This velocity is a convenient reference point when comparing the electronic energy loss of different projectiles.[†]

At these low energies, the Bethe-Bloch formula [Eq. (2.49)] breaks down. The reduction of the number of electrons contributing to the energy loss gives very large corrections. Also, the neutralization probability of the projectile becomes large. In this low energy range, the electronic energy loss becomes proportional to the velocity of the projectile. Lindhard *et al.*, (1963, abbreviated as LSS in the literature), and Firsov (1959) gave theoretical descriptions for this energy range. The LSS expression is based on elastic scattering of free target electrons in the static field of a screened point charge which describes the projectile. Firsov's expression is based on a simple geometric model of momentum exchange between the projectile and the target atom during the interpenetration of the electron clouds surrounding the two colliding atoms. Both theories adequately describe the general behavior of the stopping power with regard to the energy dependence and the magnitude.

[†] The velocity $v_0 = e^2/\hbar = 2.2 \times 10^8$ cm/sec imparted to one nucleon corresponds to 25 keV of energy. The Thomas-Fermi velocity $Z_1^{2/3} e^2/\hbar$ thus corresponds to $Z_1^{4/3} \times 25$ keV per nucleon of the projectile. This amounts to 25 keV for ${}^1\text{H}$ and 250 keV for ${}^4\text{He}$. Maxima of electronic stopping for ${}^4\text{He}$ occur more typically at 0.6 to 1.0 MeV (see Fig. 2.8).

At very low velocities, an additional energy loss process occurs. Energy can be transferred from the nucleus of the projectile to that of a target atom by electrostatic interaction between the screened charges of the two nuclei. This *nuclear energy loss*, as it is usually called, may be viewed as an elastic interaction between two free particles, except for the very last collisions, where the chemical binding energy (~ 10 eV) must be considered. As suggested by Bohr (1948) and later developed by Lindhard *et al.* (1963), the nuclear energy loss becomes another major component of energy loss at low energies, especially for heavy projectile atoms. To a good approximation, nuclear and electronic energy loss are roughly independent of each other, as is stated by Eq. (2.39).

With regard to megaelectron volt backscattering spectrometry, the situation is that, for ${}^1\text{H}$ and ${}^4\text{He}$ as projectiles, nuclear stopping is negligible everywhere except at the very lowest energies, that is, at the very end of the track of the projectile in the material.

In summary, it is fair to say that accurate numerical predictions of stopping cross sections from theory are difficult, at best, because of the large number of possible interactions that can conceivably take place. Atomic collisions are violent disturbances of atoms, and one would expect that effects due to chemical bonding and shell structure should normally be of minor importance. It has indeed turned out that approximate results come out rather easily, but accurate calculations are exceedingly difficult to obtain. The most trustworthy values of ϵ are therefore semiempirical compilations that combine theoretically evaluated dependences with the most reliable experimental data, such as the recent table of Ziegler and Chu reproduced in Table VI of Appendix F.

A number of reviews and reports on the subject of energy loss of charged particles in matter have been written over the years. The reader is referred to these and their references for further information on the subject (Bohr, 1948; Fano, 1963; Lindhard *et al.*, 1963; Lindhard, 1969; Northcliffe, 1963; Datz *et al.*, 1967; Sauter and Bloom, 1972; Schiøtt, 1973) and to the bibliography of published tables given in Appendix D.

Special effects occur in dE/dx when the beam is channeled in a single crystal target. The subject is treated in recent reviews (Gibbons, 1968; Mayer *et al.*, 1970; Dearnaley *et al.*, 1973; Gemmel, 1974).

2.5 LINEAR ADDITIVITY OF STOPPING CROSS SECTIONS (BRAGG'S RULE)

The preceding section on energy loss is restricted to elemental targets. The present section deals with energy loss in compound targets.

To a simple approximation, the process by which a particle loses energy when it moves swiftly through a medium consists of a random sequence of independent encounters between two particles: the moving projectile and an electron attached to an atom in the case of electronic energy loss, or the moving projectile and an atomic core in the case of nuclear energy loss. To the extent that this picture is correct, the situation presented by a target that contains more than one element differs only with respect to the type of atoms the projectile encounters. The energy lost to the electrons or to the atomic core in each encounter should be the same at a given projectile velocity, regardless of the further surrounding of the target atoms, since the interaction is considered to take place with only one atom at a time. This is, in essence, the idea contained in the principle of additivity of stopping cross sections, according to which the energy loss in a medium composed of various atomic species is the sum of the losses in the constituent elements, weighted proportionately to their abundance in the compound. The principle was postulated first by Bragg and Kleeman (1905) for the special case of molecules. Their postulate is now known as *Bragg's rule*. It states that the stopping cross section $\epsilon^{A_mB_n}$ of a molecule A_mB_n or a mixture with an equivalent composition of A_mB_n is given by[†]

$$\epsilon^{A_mB_n} = m\epsilon^A + n\epsilon^B, \quad (2.50)$$

where ϵ^A and ϵ^B are the stopping cross sections of the atomic constituents A and B. Let the volume density of the molecular units A_mB_n in a compound be $N^{A_mB_n}$; then the specific energy loss of the material is

$$dE^{A_mB_n}/dx = N^{A_mB_n}\epsilon^{A_mB_n}. \quad (2.51)$$

This formula, completely analogous to Eq. (2.36) for an element, states that the energy dE dissipated over the distance dx is proportional to the number of molecular units A_mB_n traversed over this distance, the proportionality constant being $\epsilon^{A_mB_n}$. Often, to simplify notation, the clumsy form A_mB_n as a superscript or subscript is abbreviated AB, e.g., ϵ^{AB} for $\epsilon^{A_mB_n}$, or N^{AB} for $N^{A_mB_n}$; the symbol AB then refers to a molecular unit of the compound composed of atoms of A and B.

For high-velocity protons ($v \gg v_0$), the rule is valid within about 1% (Fano, 1963; Burlin, 1968). For ${}^4\text{He}$ in the 1–2-MeV range, good agreement has been reported in metallic alloys and compounds (Feng *et al.*, 1973;

[†] We prefer superscripts to denote the stopping medium. Subscripts then always indicate the identity of the partner in a collision (as in $K_{st}, [e]_{st}^{(10)}$). Since this convention is not followed consistently in the literature, some care is indicated when formulas of different sources are compared.

Baglin and Ziegler, 1974). There are indications that violations can occur in gaseous organic compounds (Lodhi and Powers, 1974) and in oxides, nitrides, or other compounds in which one element is a gas in elemental form (Ziegler *et al.*, 1975). Generally, the departures are 10% or less.

2.6 ENERGY STRAGGLING

An energetic particle that moves through a medium loses energy via many individual encounters. Such a quantized process is subject to statistical fluctuations. As a result, identical energetic particles, which all have the same initial velocity, do not have exactly the same energy after passing through a thickness Δx of a homogeneous medium. The energy loss ΔE is subject to fluctuations. The phenomenon, sketched in Fig. 2.10, is called *energy straggling*. Energy straggling places a finite limit for the precision with which energy losses, and hence depths can be resolved by backscattering spectrometry. The ability to identify masses is also impaired, except for atoms located at the surface of the target. The reason is that the beam energy E before a collision with a specific mass M_2 at some depth within the target is no more monoenergetic, even if it was so initially, so that the ratio E_1/E_0 , and hence the identification of M_2 , become uncertain as well. For these reasons, it is important to have quantitative information on the magnitude of energy straggling for any given combination of energy, target material, target thickness, and projectile.

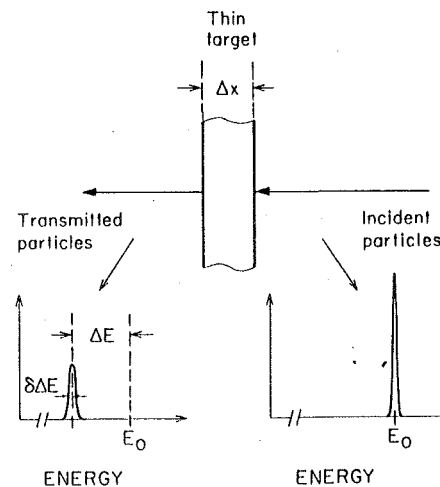


Fig. 2.10 A monoenergetic beam of energy E_0 loses energy ΔE in traversing a thin film of thickness Δx . Simultaneously, energy straggling broadens the energy profile.

Light particles such as ^1H or ^4He in the megaelectron volt range lose energy primarily by encounters with the electrons in the target, as discussed in Section 2.4. One would thus expect that the dominant contribution to energy straggling is the consequence of these electronic interactions too. This is indeed the case. One can therefore calculate the main contribution to energy straggling with the help of the same classical model employed in Section 2.4 to describe the process of electronic energy loss. It is shown there [Eq. (2.43)] that the average number $d\Delta n(E_\perp)$ of encounters that generate an energy loss E_\perp over the distance Δx is $NZ_2 \Delta x \cdot 2\pi b db$, where b is the impact parameter for such an encounter. The actual number of encounters will fluctuate statistically about this average value $d\Delta n(E_\perp)$. If one assumes that the actual numbers of these encounters have a Poisson distribution, the standard deviation of $d\Delta n(E_\perp)$ is $[d\Delta n(E_\perp)]^{1/2}$. In turn, the deviation of these numbers from their average value causes deviations from the average differential value $d\Delta E$ that these encounters contribute to ΔE . Let the deviations from the average contribution $d\Delta E$ be called $d\delta\Delta E$. Their standard deviation will be $E_\perp [d\Delta n(E_\perp)]^{1/2}$. The variance of encounters with an impact parameter between b and $b + db$ is therefore

$$d\langle(\delta\Delta E)^2\rangle = E_\perp^2 NZ_2 \Delta x 2\pi b db. \quad (2.52)$$

Encounters with other impact parameters produce similar fluctuations. As long as these fluctuations are independent, their corresponding variances add up incoherently, and the overall variance $\langle(\delta\Delta E)^2\rangle$ of $\delta\Delta E$ will be given by

$$\langle(\delta\Delta E)^2\rangle = NZ_2 \Delta x 2\pi \int_{b_{\min}}^{b_{\max}} E_\perp^2 b db. \quad (2.53)$$

For an impact parameter b , the energy loss E_\perp has the value $E_\perp = (2/m_e)(Z_1 e^2/bv_1)^2$ [see Eq. (2.42)]. The integral thus yields

$$\langle(\delta\Delta E)^2\rangle = NZ_2 \Delta x 2\pi \frac{(Z_1 e^2)^2}{m_e v_1^2} (E_{\max} - E_{\min}), \quad (2.54)$$

where E_{\max} and E_{\min} are the energy losses corresponding to encounters with minimum and maximum impact parameters b_{\min} and b_{\max} , respectively. The largest possible energy transfer in a collision between the ion of mass M_1 and an electron of mass $m_e \ll M_1$ is $2m_e v_1^2$, so that if $E_{\min} \ll E_{\max}$, then

$$\langle(\delta\Delta E)^2\rangle = NZ_2 4\pi(Z_1 e^2)^2 \Delta x. \quad (2.55)$$

This result was first derived by Bohr (1915) with the help of the same simple classical model discussed here. It is usually referred to as the *Bohr value* Ω_B^2 of *energy straggling*.[†] For a layer of thickness t , Bohr straggling thus

[†] The common notation in the literature is Ω_B . We use Ω_B to distinguish between the standard deviation of an energy distribution Ω and a solid angle of detection Ω .

has a variance

$$\Omega_B^2 = 4\pi(Z_1 e^2)^2 NZ_2 t. \quad (2.56)$$

We introduce the abbreviation

$$s^2 = 4\pi(Z_1 e^2)^2 NZ_2 \quad (2.57)$$

with which the Bohr value of energy straggling has the simple form

$$\Omega_B^2 = s^2 t. \quad (2.58)$$

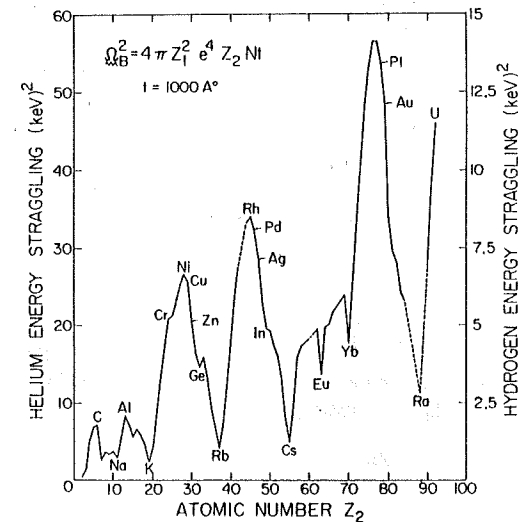


Fig. 2.11 The value of the variance $\Omega_B^2 = 4\pi Z_1^2 e^4 Z_2 N t$ for $t = 1000 \text{ \AA}$ for energy straggling according to the classical model of Bohr for electronic energy loss versus the atomic number of the target atom. The pronounced structure reflects the difference in the atomic density of the elements.

Bohr's theory predicts that energy straggling does not depend on the energy of the projectile and that the rms value of the energy variation increases with the square root of the electron density per unit area $NZ_2 t$ in the target. A plot of Ω_B^2 as a function of Z_2 is given in Fig. 2.11. The proportionality with the number of electrons per atom Z_2 accounts for the general increase of Ω_B^2 with Z_2 , but the pronounced structure in the plot is caused by the differences in the density N of the elements. This variation is removed by considering Ω_B^2/Nt . One finds that this quantity is numerically equal to Z_2 within 4% when expressed in units of $10^{-12} (\text{eV cm})^2$. This fact can be remembered for quick estimates of energy straggling.

TABLE 2.2
Experimentally Observed Values of the Standard Deviation Ω_{exp} of
Energy Straggling Compared to the Energy Loss ΔE of ^4He Traversing Films of
Al, Ni, or Au at an Energy E of 1.0 and 2.0 MeV^a

	Thickness Δx traversed		ΔE (keV)	Ω_{exp} (keV)	$\Omega_{\text{exp}}/\Delta E$ (%)	$(\bar{E}/\Delta E)^{1/2}$ (%)	E (MeV)
	($\mu\text{gm}/\text{cm}^2$)	(\AA)					
Al	120	4300	125	7.0	5.6	4	2.0
Ni	180	2000	125	5.6	4.5	4	2.0
Au	370	1900	125	5.1	4.1	4	2.0
Al	60	5900	200	7.0	3.5	2.2	1.0
Ni	260	2900	200	5.6	2.8	2.2	1.0
Au	520	2700	200	5.1	2.6	2.2	1.0

^a The film thicknesses are chosen to produce the same ΔE in all three elements. Experimental values are derived from Harris and Nicolet (1975a).

Another useful relationship can be obtained by comparing the variations in ΔE given by the value of Ω_B with ΔE itself. For an estimate, one uses the Bethe-Bloch formula [Eq. (2.46)] for dE/dx and substitutes some average value v_1^2 for the velocity along the track, say, $\bar{E} = \frac{1}{2}M_1 v_1^2$, and compares this with the value of Ω_B ; the result is

$$\frac{\Omega_B}{\Delta E} = \left(\frac{\bar{E}}{\Delta E} \frac{2 m_e}{L M_1} \right)^{1/2} \quad (2.59)$$

For ^4He , the ratio $(m_e/M_1)^{1/2}$ is about 10^{-2} . In this case, neglecting the factor $2/L$, one thus finds

$$\Omega_B/\Delta E \simeq (\bar{E}/\Delta E)^{1/2} \times 10^{-2}, \quad (2.60)$$

so that Ω_B itself is approximately 1% of the geometrical mean of ΔE and \bar{E} . Helium ions of 2 MeV undergoing an energy loss of 125 keV thus have a standard deviation of energy straggling that is about $(2.0/0.125)^{1/2}\% = 4\%$. Table 2.2 shows the experimentally observed values of $(\Omega_{\text{exp}}/\Delta E)^{1/2}$ for this and another example, with Al, Ni, and Au as targets. As can be seen, this ratio is indeed quite constant; it agrees in the order of magnitude predicted by the formula above, although the actual value differs from the estimate. The formula is thus a good rule of thumb, but does not yield quantitatively trustworthy numbers.

Bohr's model assumes that an individual energy transfer takes place between a free stationary electron and a fully ionized projectile of charge $Z_1 e$. These assumptions are fulfilled only in the Bethe-Bloch region (see Fig. 2.9).

At energies in the vicinity of the maximum of the dE/dx curve and below, the assumption of a fully ionized projectile is no longer valid. The fact that electrons are bound to atoms and are not free and stationary, as assumed, also becomes increasingly important as the projectile energy decreases. To account for this, Lindhard and Scharff (1953) extended Bohr's theory and derived a correction factor for low- and medium-energy projectiles. They obtained

$$\begin{aligned} \Omega^2 &= \Omega_B^2 \frac{1}{2} L(\chi) & \text{for } \chi \leq 3, \\ \Omega^2 &= \Omega_B^2 & \text{for } \chi \geq 3, \end{aligned} \quad (2.61)$$

where χ , a reduced energy variable, is

$$\chi = v^2/Z_2 v_0^2. \quad (2.62)$$

Here v is the velocity of the projectile, $v_0 \equiv e^2/\hbar = 2.2 \times 10^8$ cm/sec, and $L(\chi)$ is the stopping number, which appears in the Bethe-Bloch formula, Eq. (2.46). Bonderup and Hvelplund (1971) have improved Lindhard and Scharff's expression by using a more refined description than had been used previously for the atomic charge distribution and for the process of energy straggling. They compare their calculations with experimental results of energy straggling for ^1H and ^4He in various gases (Bonderup and Hvelplund 1971; Hvelplund, 1971) and conclude that the Lindhard-Scharff formulation gives a fair account of the observed overall energy dependence of straggling. They also observe that when one plots Ω_{exp}^2/Nt against the projectile energy for various gases, the curve exhibits oscillations versus Z_2 similar to those observed in Fig. 2.8 for the stopping cross sections. These oscillations have been explained both for dE/dx (Chu and Powers, 1972) and for energy straggling (Chu, 1976) by using atomic charge distributions of the Hartree-Fock-Slater type and incorporating them into the theory of Lindhard and Winther (Lindhard and Winther, 1964) for dE/dx , and the theory of Bonderup and Hvelplund (1971) for energy straggling. Where the measurements of energy straggling are sufficiently reliable, an acceptable agreement with these calculations is obtained.

In the energy range 1–2 MeV, which is of primary interest to backscattering spectrometry, almost all of the available experimental data on energy straggling pertain to ^1H in gases. The advent of backscattering spectrometry as an analytical tool has generated renewed interest in experimental information on straggling in this energy range, particularly for ^4He in solids. Presently, the only data available are for Al, Ni, Pt, and Au (Harris and Nicolet, 1975a,b). The results show only a weak energy dependence which is in qualitative agreement with the theories of Lindhard and Scharff, of Bonderup and Hvelplund, and of Chu. Numerically, Bohr's value Ω_B is within 40% of the data. Until more experimental data are available, the

standard deviation Ω_B thus is the most appropriate value to use in estimating energy straggling in solids in the 1 to 2 MeV range.

Bohr's theory of energy straggling not only gives the standard deviation Ω_B of a beam which has traversed a medium, but also predicts that the distribution is Gaussian. This is a consequence of the assumption that the number of collisions is large and follows a Poisson distribution. The result is clearly approximate, as a Gaussian has a finite amplitude at any energy, but the transmitted beam surely cannot contain particles of energy larger than E_0 . An accurate description of energy straggling must therefore necessarily lead to a distribution function that is not symmetrical with respect to the mean. This is born out by theoretical studies of energy straggling in beams passing through very thin absorbers (Landau, 1944; Vavilov, 1957; Tschalär, 1968; Kolata, 1968; and others; for a recent contribution, with references, see Bichsel and Saxon, 1975; Deconninck and Foulhe, 1976), and by recent transmission measurements of protons through Si. In the energy range of 1 to 2 MeV for ^1H and ^4He , the effect is below the resolution of conventional solid-state detection systems. For the purposes of backscattering spectrometry, the Gaussian distribution thus describes energy straggling satisfactorily (also see Appendix B).

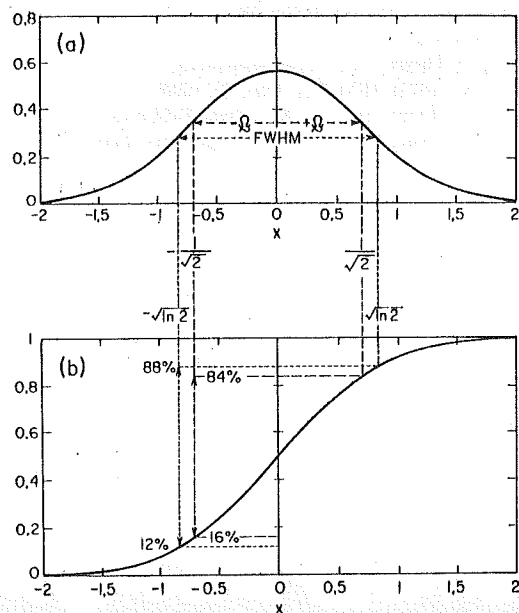


Fig. 2.12 Plot of (a) the Gaussian distribution $(2\pi\Omega^2)^{-1/2} \exp[-(x^2/2\Omega^2)]$ with $\Omega = 1/\sqrt{2}$, and (b) the corresponding error function integral $\text{erf}(x) = (2\pi\Omega^2)^{-1/2} \int_{-\infty}^x \exp[-(x^2/2\Omega^2)] dx$ with $\Omega = 1/\sqrt{2}$.

Backscattering spectra most often display the integral of the Gaussian distribution, the error function

$$\text{erf}(x) = (2\pi\Omega^2)^{-1/2} \int_{-\infty}^x \exp[-(x^2/2\Omega^2)] dx \quad (2.63)$$

rather than the Gaussian distribution

$$(2\pi\Omega^2)^{-1/2} \exp[-(x^2/2\Omega^2)]. \quad (2.64)$$

The relation between the two is graphically shown in Fig. 2.12a and b for $\Omega^2 = \frac{1}{2}$. As can be seen, the full width at half maximum (FWHM) of a Gaussian corresponds to the 12 to 88% range of the error function and the $\pm\Omega$ points in the Gaussian correspond to the 16 to 84% points. The FWHM is wider than Ω by a factor of $2(2 \ln 2)^{1/2} = 2.355$.

2.7 LINEAR ADDITIVITY OF ENERGY STRAGGLING

Experimental data on energy straggling below 2 MeV for ^1H and ^4He in solid elemental targets are few. For solid compound targets, no experimental data exist at all. The need for information is obvious. Until such results become available, statements on energy straggling in solid compounds must necessarily be conjectural.

The most obvious suggestion as to how energy straggling behaves in a compound or a mixture $A_m C_n$ proceeds as follows (Chu, 1976). Let N_A and N_C be the volume densities of the individual elements A and C, and let $N^{A_m C_n}$ be the volume density of compositional units $A_m C_n$ in the mixture or compound. Assume that for a thickness t , the energy straggling in elements A and C individually is [Eq. (2.56)]:

$$(\Omega_B^A)^2 = 4\pi(Z_1 e^2)^2 N_A Z_A t, \quad (2.65)$$

$$(\Omega_B^C)^2 = 4\pi(Z_1 e^2)^2 N_C Z_C t. \quad (2.66)$$

This means that $(\Omega_B^A)^2/N_A Z_A t = (\Omega_B^C)^2/N_C Z_C t = 4\pi(Z_1 e^2)^2$ is independent of the target, the ratio being simply the square of the energy variance per electron in a unit area of the target with thickness t . An extension of Bohr's model to a compound target then predicts that this quantity should apply independently of the composition of the target, or

$$\frac{(\Omega_B^{A_m C_n})^2}{\left(\frac{\text{number of electrons per unit area of the target of thickness } t}{\text{area of the target of thickness } t}\right)} = 4\pi(Z_1 e^2)^2, \quad (2.67)$$

and therefore

$$(\Omega_B^{A_m C_n})^2 = 4\pi(Z_1 e^2)^2 N^{A_m C_n} (mZ_A + nZ_C) t. \quad (2.68)$$

The last three factors give the number of electrons per unit area in the target. This equation can also be written as

$$\frac{(\Omega_B^{\Lambda_m C_n})^2}{N^{\Lambda_m C_n t}} = m \frac{(\Omega_B^{\Lambda})^2}{N_{\Lambda t}} + n \frac{(\Omega_B^C)^2}{N_{Ct}}, \quad (2.69)$$

which clearly bears out the assumption of additivity. Until measurements are made, these equations must be considered as hypothetical and should be used as guidelines only. Their validity has yet to be tested.

REFERENCES

- Abrahamson, A. A. (1969). *Phys. Rev.* **178**, 76.
 Baglin, J. E. E., and Ziegler, J. F. (1974). *J. Appl. Phys.* **45**, 1413.
 Bethe, H. A. (1930). *Ann. Phys.* **5**, 325.
 Bichsel, H., and Saxon, R. P. (1975). *Phys. Rev. A* **11**, 1286.
 Bloch, F. (1933). *Ann. Phys.* **16**, 285; *Z. Phys.* **81**, 363.
 Bohr, N. (1913). *Phil. Mag.* **25**, 10.
 Bohr, N. (1915). *Phil. Mag.* **30**, 581.
 Bohr, N. (1940). *Phys. Rev.* **58**, 654.
 Bohr, N. (1941). *Phys. Rev.* **59**, 270.
 Bohr, N. (1948). *Mat. Fys. Medd. Dan. Vid. Selsk.* **18**, No. 8.
 Bonderup, E., and Hvelplund, P. (1971). *Phys. Rev. A* **4**, 562.
 Bourland, P. D., and Powers, D. (1971). *Phys. Rev. B* **3**, 3635.
 Bourland, P. D., Chu, W. K., and Powers, D. (1971). *Phys. Rev. B* **3**, 3625.
 Bragg, W. H., and Kleeman, R. (1905). *Phil. Mag.* **10**, S318.
 Burlin, T. E. (1968). in "Radiation Dosimetry" (F. H. Attix and W. C. Roesch, eds.), Vol. I, p. 331. Academic Press, New York.
 Chu, W. K. (1976). *Phys. Rev. A* **13**, 2057.
 Chu, W. K., and Powers, D. (1972). *Phys. Lett.* **38A**, 267.
 Darwin, C. G. (1914). *Phil. Mag.* **28**, 499.
 Datz, S., Erginsoy, C., Leibfried, G., and Lutz, H. O. (1967). *Ann. Rev. Nucl. Sci.* **17**, 129.
 Dearnaley, G., Freeman, J. H., Nelson, R. S., and Stephen, J. (1973). "Ion Implantation." North-Holland Publ., Amsterdam.
 Deconninek, G., and Foulhe, Y. (1976). In "Ion Beam Surface Layer Analysis" (O. Meyer, G. Linker, and F. Käppeler, eds.), p. 87. Plenum Press, New York.
 Everhart, E., Stone, G., and Carbone, R. J. (1955). *Phys. Rev.* **99**, 1287.
 Fano, U. (1963). *Ann. Rev. Nucl. Sci.* **13**, 1.
 Feng, J. S.-Y., Chu, W. K., and Nicolet, M.-A. (1973). *Thin Solid Films* **19**, 227.
 Feng, J. S.-Y., Chu, W. K., and Nicolet, M.-A. (1974). *Phys. Rev. B* **10**, 3781.
 Firsov, O. B. (1959). *Zh. Eksp. Teor. Fiz.* **36**, 1517.
 Gemmell, D. S. (1974). *Rev. Mod. Phys.* **46**, 129.
 Gibbons, J. F. (1968). *Proc. IEEE* **56**, 295.
 Goldstein, H. (1959). "Classical Mechanics." Addison-Wesley, Reading, Massachusetts.
 Harris, J. M., and Nicolet, M.-A. (1975a). *Phys. Rev. B* **11**, 1013.
 Harris, J. M., and Nicolet, M.-A. (1975b). *J. Vac. Sci. Technol.* **12**, 439.
 Hvelplund, P. (1971). *Mat. Fys. Medd. Dan. Vid. Selsk.* **38**, 4.
 Kolata, J. J. (1968). *Phys. Rev.* **176**, 484.
 Landau, L. (1944). *J. Phys.* **8**, 201.

- Leighton, R. B. (1959). "Principles of Modern Physics." McGraw-Hill, New York.
 Lindhard, J. (1969). *Proc. Roy. Soc. London A* **311**, 11.
 Lindhard, J., and Scharff, M. (1953). *Mat. Fys. Medd. Dan. Vid. Selsk.* **27**, No. 15.
 Lindhard, J., Scharff, M., and Schiøtt, H. E. (1963). *Mat. Fys. Medd. Dan. Vid. Selsk.* **33**, No. 14.
 Lindhard, J., and Winther, A. (1964). *Mat. Fys. Medd. Dan. Vid. Selsk.* **34**, No. 4.
 Lodhi, A. S., and Powers, D. (1974). *Phys. Rev. A* **10**, 2131.
 Marion, J. B., and Young, F. C. (1968). "Nuclear Reaction Analysis, Graphs and Tables." Wiley, New York.
 Matteson, S., Chau, E. K. L., and Powers, D. (1977). *Phys. Rev. A* **15**, 856.
 Mayer, J. W., Eriksson, L., and Davies, J. A. (1970). "Ion Implantation in Semiconductors." Academic Press, New York.
 Northcliffe, L. C. (1960). *Phys. Rev.* **120**, 1744.
 Northcliffe, L. C. (1963). *Ann. Rev. Nucl. Sci.* **13**, 67.
 Powers, D., Chu, W. K., Robinson, R. J., and Lodhi, A. S. (1972). *Phys. Rev. A* **6**, 1425.
 Powers, D., Lodhi, A. S., Lin, W. K., and Cox, H. L. (1973). *Thin Solid Films* **19**, 205.
 Robinson, M. T., (1974). Oak Ridge Rep. ONRL-4556.
 Rousseau, C. C., Chu, W. K., and Powers, D. (1971). *Phys. Rev. A* **4**, 1066.
 Rutherford, E., (1911). *Phil. Mag.* **21**, 669.
 Sauter, G. D., and Bloom, S. C. (1972). *Phys. Rev. B* **6**, 669.
 Schiøtt, H. E. (1973). Interaction of Energetic Charged Particles with Solids, p. 6. Brookhaven Nat. Lab. Rep. No. BNL-50336.
 Thompson, D. A., and Mackintosh, W. D. (1971). *J. Appl. Phys.* **42**, 3969.
 Tschalär, C. (1968). *Nucl. Instrum. Methods* **61**, 141.
 Van Wijngaarden, A., Brimmer, E. J., and Baylis, W. E. (1970). *Can. J. Phys.* **48**, 1835.
 Vavilov, P. V. (1957). *JETP* **5**, 749.
 Warters, W. D. (1953). Ph. D. Thesis, Caltech (unpublished).
 Ziegler, J. F., and Chu, W. K. (1973). IBM Res. Rep. RC 4288.
 Ziegler, J. F., and Chu, W. K. (1974). *At. Data Nuc. Data Tables* **13**, 463.
 Ziegler, J. F., Chu, W. K., and Feng, J. S.-Y. (1975). *Appl. Phys. Lett.* **27**, 387.

Concepts of Backscattering Spectrometry

The purpose of this and the following chapter is to describe in principle how a backscattering spectrum is generated and how it is interpreted in terms of the basic concepts introduced in Chapter 2. The concern here is with general notions. In Chapter 4 these concepts are applied to thin films and layered structures. Detailed examples are presented in Chapter 5.

3.1 INTRODUCTION

The components of a backscattering system are shown in Fig. 3.1. The source generates a beam of collimated and monoenergetic particles of energy E_0 . A typical case is a current of 10 to 100 nA of 2.0-MeV He^+ ions in a

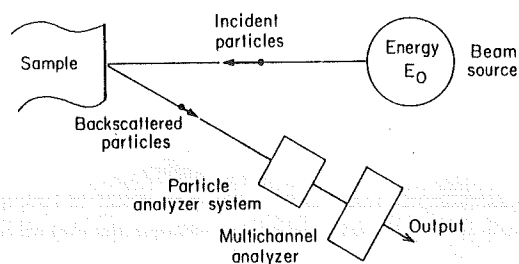


Fig. 3.1 Conceptual layout of a backscattering spectrometry system.

1-mm² area. These particles impinge on the sample (or target) which is the object to be analyzed. Almost all of the incident particles come to rest within the sample. A very few (much less than one in 10^4) are scattered back out of the sample. Of these, a small fraction is incident on the area defined by the aperture of an analyzing system. The output of that system is an analog signal. This signal is processed by a multichannel analyzer, which subdivides its magnitude into a series of equal increments. Each increment is numbered and referred to as a *channel*. Modern multichannel analyzers contain thousands of channels. An event whose magnitude falls within a particular channel is registered there as a *count*. At the termination of the experiment, each channel has registered a certain number of counts. The output of the multichannel analyzer is thus a series of counts contained in the various channels.

A segment of such a series from channels 132–136 is shown in Fig. 3.2. We shall refer to the counts contained in channel i as H_i . This digital information can be recorded in various ways. The graphical display is advantageous for quick interpretation. Digital outputs are used for numerical

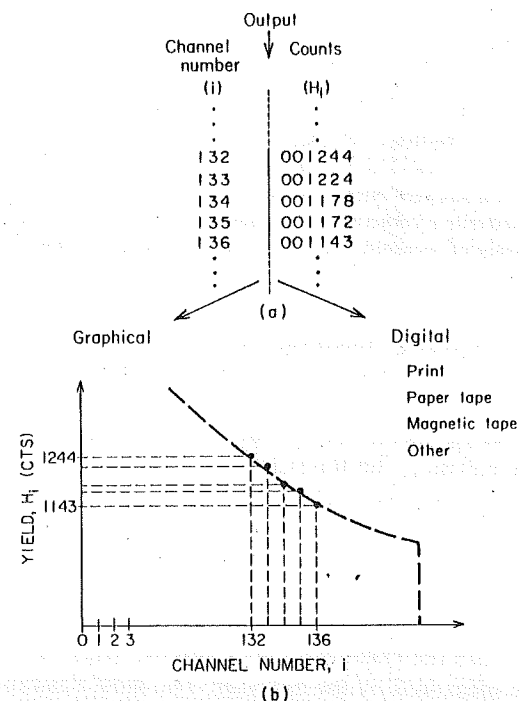


Fig. 3.2 Basic content of a backscattering spectrum and some methods of recording. (a) The ordinal number (left) identifies each channel, which contains a certain number of counts. (b) Various ways of recording a spectrum.

analysis. Computer facilities with graphical display terminals can combine both. Such a series of counts versus channel number constitutes a *backscattering spectrum*. In the graphical display, the ordinate is frequently labeled *yield* or *backscattering yield*.

The analog signal generated by the analyzer contains quantitative information on one particular parameter of the detected particle. As shown in Fig. 3.3, there are a number of parameters—energy, momentum, etc.—that can be used to characterize the backscattered particles. For example, magnetic spectrometers measure momentum. The backscattering spectrum obtained with such an analyzer is a *backscattering momentum spectrum*. A semiconductor particle detector produces an analog signal proportional to the energy of the backscattered particle. Correspondingly, a spectrum obtained with such a detector is a *backscattering energy spectrum*.

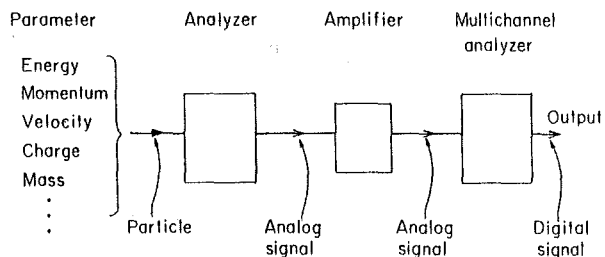


Fig. 3.3 The particle analyzer system of Fig. 3.1 may measure any one of several distinct parameters that characterize a backscattered particle. This analyzer generates an analog signal. The multichannel analyzer measures that signal and registers the value as a count in the appropriate channel.

The particular analyzing system assumed in the rest of this book consists of an energy-sensitive analyzer followed by amplifiers and a multichannel analyzer, as shown in Fig. 3.3. This analyzing system is the most commonly used in backscattering spectrometry, but there are other methods to obtain a spectrum. For instance, the multichannel analyzer can be replaced by a single channel whose position is changed sequentially so as to scan the range of the parameter measured. Regardless of their inner working, the common feature of all such systems is an output consisting of a set of counts corresponding to a sequence of channels.

In general, whatever the analyzer, there should exist a one-to-one correspondence between the channel number and the magnitude of the particle parameter to be measured by the analyzer. The most desirable property of this relationship is that it be exactly linear and stable in time. Additionally, for convenience, one likes fast acquisition of data and detectors of small physical size. The semiconductor surface-barrier detector combined with a

3.1 Introduction

charge-sensitive preamplifier meets these criteria best among current options. It is therefore used almost universally in backscattering spectrometry. Consequently, in this book we shall be concerned almost exclusively with backscattering energy spectra. The descriptive term, "backscattering energy spectrum," will thus often be shortened to *backscattering spectrum* or *spectrum*. In those rare cases where energy is not displayed, one should explicitly identify the parameter measured.

The relation between the energy of a backscattered and detected particle and the channel number in which that particle is counted is a characteristic of the system and must be determined experimentally (as described in Section 5.2). Figure 3.4 shows this relation schematically. The abscissa gives the channel number i . The ordinate gives the energy E_i of a detected particle, where $E_{1,i}$ is the energy of particles that produce counts in channel i . We shall assume a linear relationship, as indicated in the figure. The slope of the line will be denoted by \mathcal{E} , the *energy interval corresponding to one channel*. The offset of the line is always adjustable by changing the gain settings of the electronics in the analyzer system. This allows one to display a selected part of the energy spectrum over the full range of the multichannel analyzer. (Typical numbers for \mathcal{E} are about 4 keV with megaelectron volts He ions, and the offset is some hundreds of kiloelectronvolts.) As defined previously, \mathcal{E} is the slope of a straight line, and hence constant. In the rest of the book we shall assume that this holds in a given experimental situation. When \mathcal{E} is a function of energy, i.e., when the relation between channel number and particle energy is not a linear one as shown in Fig. 3.4, equations describing an energy spectrum must be modified.

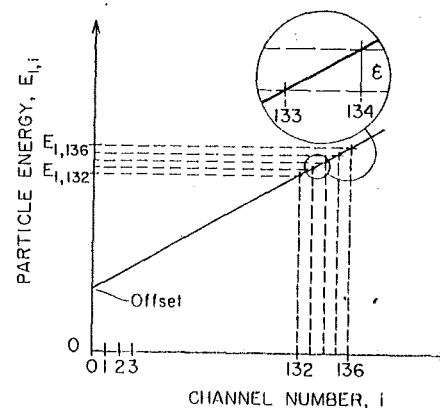


Fig. 3.4 Ideally, in an analyzer that senses energy, the energy E_i of a detected particle is related exactly linearly to the channel number that identifies the channel in which the event is registered as one count. The slope of the line is characterized by the energy interval \mathcal{E} of one channel.

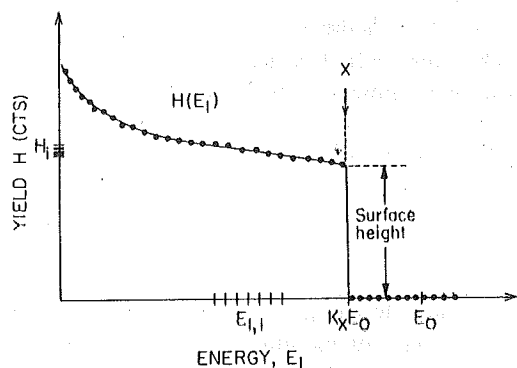


Fig. 3.5 The conversion of channel number to energy E_1 (shown in Fig. 3.4) transforms the abscissa of a backscattering spectrum (as shown in Fig. 3.2) from channel number to energy E_1 , where E_0 gives the energy of the incident particles and KE_0 is called the *edge* of element X in the spectrum.

With the relation of channel number to energy established, one can convert the abscissa of a backscattering spectrum from channel numbers to particle energy E_1 , as shown in Fig. 3.5. This plot is a typical form of a backscattering energy spectrum. Sometimes spectra are plotted in terms of channel numbers only. In such a case, one should specify \mathcal{E} and the energy offset; otherwise the information provided is not complete.

One frequently interprets such a spectrum in terms of a continuous function H of the continuous variable E_1 .[†] The expression $H(E_1)$ then stands for the counts H_i in channel i which corresponds to the energy $E_{1,i}$. The terms H_i and H are both referred to as the *height of the spectrum*. The terms *yield* and *backscattering yield* are sometimes used with the same meaning.

In Section 2.2 it is shown that the energy of particles scattered from an atom at rest cannot have energies above KE_0 , where E_0 is the energy of the incident particle. For particles backscattered from a monoisotopic elemental sample, the spectrum has a step at an energy $E_1 = KE_0$ corresponding to scattering from surface atoms; this step is referred to as the edge of the element and is frequently indicated with an arrow or a line, as in Fig. 3.5. In the vicinity of KE_0 , the height of the spectrum is frequently called the *surface height*.

If there is more than one element in the sample, the spectrum contains counts generated by particles scattered from the different elements. The counts generated from a given element are called the *signal* of this element in the spectrum.

[†] Certain analyzing methods actually generate a permanent continuous record whose ordinate gives an analog signal of H (e.g., photographic records). A digital output can then be formed by subsequent digitalization and multichannel analysis.

The purpose of backscattering spectrometry is to extract quantitative information on the elemental composition of the sample. Since the edges are well defined, one can usually readily identify some of the elements present in the outermost layers of the sample. Since the primary particles penetrate into the sample virtually unattenuated, scattering occurs from atoms located below the surface as well. The energy immediately before the scattering is less than E_0 because energy is lost along the incident path. After scattering, the particles escaping the sample lose energy along the outward path. Consequently, the energy of the detected particles depends on the depth at which scattering occurred. The backscattering yield at that energy depends on the number of atoms present at that depth. The problem in backscattering analysis, therefore, consists of properly interpreting the measured backscattering spectrum in terms of distributions of atoms in depth below the surface. This, then, is the topic to which we shall address ourselves in the rest of this chapter.

We assume, of course that the sample is laterally uniform. When that assumption cannot be made, the analysis of the spectrum becomes vastly more difficult.

3.2 DEPTH SCALE FOR AN ELEMENTAL SAMPLE

This section describes how one relates the energy E_1 of the detected particle to the depth x at which the backscattering event occurs in a monoisotopic elemental sample. In Fig. 3.6 the energy of the incident particles is E_0 , the *energy immediately before scattering at a depth x* is E , and the energy of the particle emerging from the surface is E_1 . The incident beam is smaller than the target. The incident particle, the exiting particle and the normal of the sample are all contained in one plane, so that the scattering angle in the laboratory frame of reference is given by $\theta = 180^\circ - \theta_1 - \theta_2$, where θ_1 and θ_2 are the angles between the sample normal and the direction of the incident beam and of the scattered particle, respectively. Note that

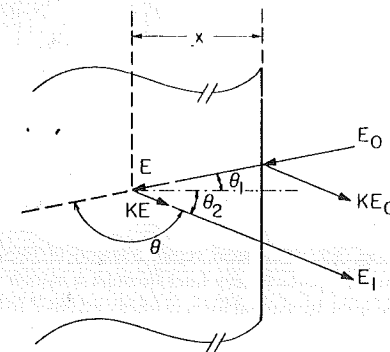


Fig. 3.6 Symbols used in the description of backscattering events in a sample (or target) consisting of a monoisotopic element. The angles θ_1 and θ_2 are positive regardless of the side on which they lie with respect to the normal of the sample. The incident beam, the direction of detection, and the sample normal are coplanar.

both θ_1 and θ_2 are defined as positive numbers whether they are located on one or the other of the sample normal. (Other geometrical arrangements are described in Section 7.5.) According to Section 2.4, we can relate the energy E to the length $x/\cos\theta_1$ of the incident path by

$$x/\cos\theta_1 = -\int_{E_0}^E dE/(dE/dx), \quad (3.1)$$

where the negative sign arises because E is smaller than E_0 and dE/dx is taken as a positive quantity. Similarly, the path length $x/\cos\theta_2$ of the outward path is related to KE and E_0 by

$$x/\cos\theta_2 = -\int_{KE}^{E_1} dE/(dE/dx), \quad (3.2)$$

A graphical interpretation of these two equations is given in Fig. 3.7. Part (a) shows dE/dx as a function of energy as a light line. The heavy segments give the dE/dx values for the inward path from E_0 to E and for the outward

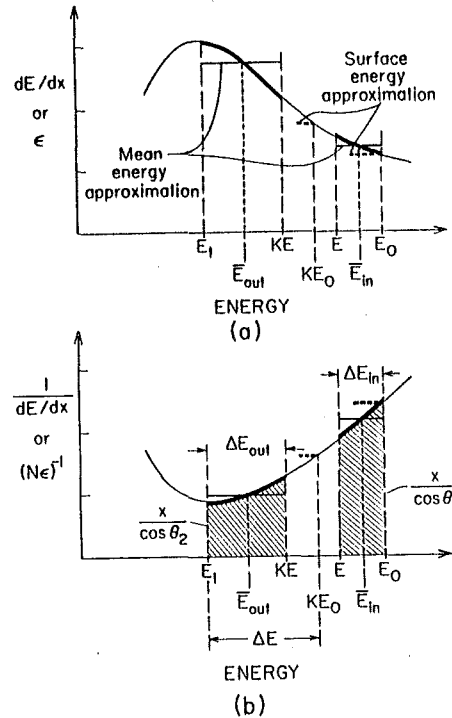


Fig. 3.7 Graphical representation of the energy loss of particles along their inward and outward paths (heavy line) through a sample consisting of a monoisotopic element. The light line is the functional form of dE/dx versus E in (a) and of $(dE/dx)^{-1}$ versus E in (b). Since $dE/dx = Ne$, the plot in (a) applies to e versus E as well.

path from KE to E_1 . The difference $E_0 - E$ is the energy loss along the inward path ΔE_{in} ; similarly, $KE - E_1$ is the energy loss along the outward path ΔE_{out} . According to Eqs. (3.1) and (3.2), it is the reciprocal of dE/dx that must be integrated over these two segments. This reciprocal curve is shown in part (b) of Fig. 3.7, with the heavy segments again indicating values for the inward and outward paths. By Eqs. (3.1) and (3.2), the two shaded areas give the path lengths $x/\cos\theta_1$ for the inward path and $x/\cos\theta_2$ for the outward path. If $\theta_1 = \theta_2$, these two areas are exactly equal.

To relate the energy E_1 of the detected particle to the depth x at which the backscattering event occurs, it is necessary to find the value of the shaded areas. The problem is that the energy E before scattering is not an experimentally accessible quantity, but E_0 and E_1 are. One thus desires to find x in terms of E_0 and E_1 . There are three ways of doing this:

1. Use tabulated values of dE/dx and execute the integrations numerically to find corresponding sets of E and x , and subsequently KE and E_1 . This approach, generally carried out with computers, is described in Section 3.4.
2. Assume that dE/dx is constant over each path. Equations (3.1) and (3.2) can then be integrated and E can be eliminated. This is discussed in the following section.
3. Assume some functional dependence for dE/dx . Matching pairs of E and x and of x and E_1 can then be obtained analytically.

3.2.1 Energy Loss Factor $[S]$ and Stopping Cross Section Factor $[s]$

If one assumes a constant value for dE/dx along the inward and outward paths, the two integrals in Eqs. (3.1) and (3.2) reduce to

$$E = E_0 - \frac{x}{\cos\theta_1} \frac{dE}{dx} \Big|_{in} \quad (3.3)$$

and

$$E_1 = KE - \frac{x}{\cos\theta_2} \frac{dE}{dx} \Big|_{out}, \quad (3.4)$$

where the subscripts "in" and "out" refer to the (constant) values of dE/dx along the inward and outward paths (Fig. 3.7). By eliminating E from these two equations, we have

$$KE_0 - E_1 = \left[\frac{K}{\cos\theta_1} \frac{dE}{dx} \Big|_{in} + \frac{1}{\cos\theta_2} \frac{dE}{dx} \Big|_{out} \right] x. \quad (3.5)$$

The energy KE_0 is the edge of the backscattering spectrum (Fig. 3.5) and corresponds to the energy of particles scattered from atoms at the surface

of the target. The energy E_1 is the measured value of a particle scattered from an atom at depth x . If one introduces the symbol ΔE for the energy difference between E_1 and KE_0 (Fig. 3.7), i.e.,

$$\Delta E = KE_0 - E_1, \quad (3.6)$$

then one can write

$$\Delta E = [S]x, \quad (3.7)$$

where

$$[S] \equiv \left[\frac{K}{\cos \theta_1} \frac{dE}{dx} \Big|_{in} + \frac{1}{\cos \theta_2} \frac{dE}{dx} \Big|_{out} \right] \quad (3.8)$$

is called the *energy loss factor* or *S factor*. An equivalent set of equations can be given in terms of stopping cross sections rather than dE/dx :

$$\Delta E = [\epsilon]Nx, \quad (3.9)$$

where

$$[\epsilon] = \left[\frac{K}{\cos \theta_1} \epsilon_{in} + \frac{1}{\cos \theta_2} \epsilon_{out} \right] \quad (3.10)$$

is called the *stopping cross section factor* or *ϵ factor*.

The assumption of constant values for dE/dx or ϵ along each track thus leads to a linear relationship between the energy ΔE below the edge KE_0 and the depth at which scattering occurs. One can therefore assign a linear depth scale to the energy axis, as indicated in Fig. 3.8.

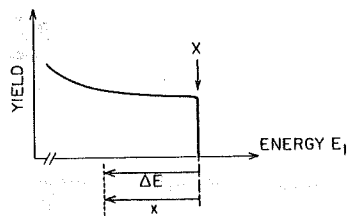


Fig. 3.8 When one assumes the energy loss to be constant along the inward and outward paths, then the energy ΔE can be linearly related to the depth x through $\Delta E = [S]x$ as indicated in the abscissa of the backscattering spectrum.

This result is derived under the assumption that dE/dx or ϵ is constant along the inward and outward path. Since this is an approximation, the resulting depth scale also applies only approximately. However, it is also clear from inspection of Fig. 3.7 that for any given E_0 and E_1 a pair of unique values of $(dE/dx)_{in}$ and $(dE/dx)_{out}$ exist for which this linear scale gives one exact value of depth at which scattering occurs. These two particular values of dE/dx are those for which the product of $(dE/dx)^{-1}$ and the energy intervals ΔE_{in} and ΔE_{out} exactly coincide with the values of the corresponding integrals (shaded areas in Fig. 3.7). In Section 3.3 an iterative procedure is described

by which these particular values of dE/dx can be sought. By applying this procedure point by point, an accurate relation between the backscattering depth and E_1 can be constructed. In the next subsection, useful approximation methods of finding values of $(dE/dx)_{in}$ and $(dE/dx)_{out}$ or ϵ_{in} and ϵ_{out} are discussed. We also use $\epsilon(E_{in})$ and $\epsilon(E_{out})$ to indicate the energy at which ϵ is evaluated.

Figure 3.9 describes graphically the connection between the energy loss factor $[S]$ and the actual depth x at which backscattering occurs for a given energy loss ΔE . The exact relationship between ΔE and x derived from Eqs. (3.1) and (3.2) is generally not linear. The energy loss factor provides a linear approximation [Eq. (3.7)] which is exact at one point.

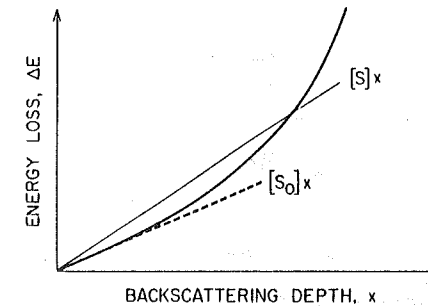


Fig. 3.9 The solid curve shows the general relation between the energy loss ΔE and the depth x at which backscattering occurs. The linear relation $\Delta E = [S]x$ is exact at one depth. The symbol $[S_0]$ refers to the surface energy approximation discussed in Section 3.2.2, with the dashed line representing $[S_0]x$. The incident energy is E_0 .

3.2.2 Approximations to $[S]$ and $[\epsilon]$

a. Surface Energy Approximation. For regions near the surface, the thickness x is small and the relative change of energy along the incident path is small also. Therefore $(dE/dx)_{in}$ is evaluated at E_0 . Similarly, $(dE/dx)_{out}$ is taken at KE_0 (see heavy dotted lines in Fig. 3.7). In this *surface energy approximation*, one thus sets

$$[S_0] = \left[\frac{K}{\cos \theta_1} \frac{dE}{dx} \Big|_{E_0} + \frac{1}{\cos \theta_2} \frac{dE}{dx} \Big|_{KE_0} \right] \quad (3.11)$$

or

$$[\epsilon_0] = \left[\frac{K}{\cos \theta_1} \epsilon(E_0) + \frac{1}{\cos \theta_2} \epsilon(KE_0) \right] \quad (3.12)$$

where the stopping cross sections $\epsilon(E_0)$ and $\epsilon(KE_0)$ are evaluated at energies E_0 and KE_0 , respectively. This particular approximation is used so frequently

that the symbols $[S_0]$ and $[\epsilon_0]$ are introduced to refer to it. The connection between $[S_0]$ and the exact ΔE versus x dependence is shown in Fig. 3.9.

b. Mean Energy Approximation. When the path length becomes appreciable, the surface approximation degrades (Fig. 3.9). As can be seen from Fig. 3.7, a better approximation can be obtained by selecting a constant value of dE/dx or ϵ at an energy \bar{E} intermediate to that which the particle has at the end points of each track. We define

$$[\bar{S}] \equiv \left[\frac{K}{\cos \theta_1} \frac{dE}{dx} \Big|_{\bar{E}_{in}} + \frac{1}{\cos \theta_2} \frac{dE}{dx} \Big|_{\bar{E}_{out}} \right] \quad (3.13)$$

or

$$[\bar{\epsilon}] \equiv \left[\frac{K}{\cos \theta_1} \epsilon(\bar{E}_{in}) + \frac{1}{\cos \theta_2} \epsilon(\bar{E}_{out}) \right]. \quad (3.14)$$

In the *mean energy approximation*, one assumes that

$$\bar{E}_{in} = \frac{1}{2}(E + E_0) \quad (3.15)$$

and

$$\bar{E}_{out} = \frac{1}{2}(E_1 + KE). \quad (3.16)$$

The value of E in the preceding equations is unknown, but can be estimated in various ways. General methods are described in Section 3.3.

For quick estimates one can assume that the energy difference $\Delta E = KE_0 - E_1$ is known and that this loss is subdivided symmetrically between the incident path and the outward path, so that E is approximately $E_0 - \frac{1}{2}\Delta E$. The values \bar{E}_{in} and \bar{E}_{out} are then given by

$$\bar{E}_{in} \simeq E_0 - \frac{1}{4}\Delta E \quad (3.17)$$

and

$$\bar{E}_{out} \simeq E_1 + \frac{1}{4}\Delta E. \quad (3.18)$$

When these values are used to complete the definitions of $[\bar{S}]$ or $[\bar{\epsilon}]$, the method is called the *symmetrical mean energy approximation*. This approximation, which is particularly good when $K \simeq 1$ and $\theta_1 \simeq \theta_2$, has the advantage of simplicity. It serves well as a quick estimate of the probable error of the surface approximation.

3.3 ENERGY E BEFORE SCATTERING

In the previous section the energy E immediately before scattering at the depth x is needed for the mean energy approximation. This energy E is needed not only for depth calculations, but also to evaluate the scattering

cross section $\sigma(E)$ in depth profile applications. In that latter case, fairly accurate estimates are required because scattering cross sections vary inversely with the square of the energy E . Cruder approximations to E suffice for the evaluation of the depth at which scattering occurs, since dE/dx is not a strong function of energy. In this section we enumerate methods for finding E that have been used in the analysis of backscattering spectra.

3.3.1 Energy Loss Ratio Method

A simple but very useful procedure to obtain E as a function of E_1 and E_0 has been described by Lever (1976). One assumes that the ratio α of the energy lost along the outward track ΔE_{out} to that lost along the inward track ΔE_{in} is independent of depth, i.e.,

$$\alpha = \Delta E_{out}/\Delta E_{in} = \text{const} \quad (3.19)$$

(see Fig. 3.7). The energy losses ΔE_{out} and ΔE_{in} are $\Delta E_{out} = KE - E_1$ and $\Delta E_{in} = E_0 - E$. The ratio α then is $\alpha = (KE - E_1)/(E_0 - E)$, which gives

$$E = (E_1 + \alpha E_0)/(K + \alpha). \quad (3.20)$$

An approximate value for α can be determined from the surface energy approximation, which assumes that Eqs. (3.1) and (3.2) can be written as $(E_0 - E)/\epsilon(E_0)N = x/\cos \theta_1$ and $(KE_0 - E_1)/\epsilon(KE_0)N = x/\cos \theta_2$, respectively, so that

$$\alpha \simeq [\epsilon(KE_0)/\epsilon(E_0)]\beta, \quad (3.21)$$

where

$$\beta \equiv \cos \theta_1/\cos \theta_2. \quad (3.22)$$

This value of α can readily be computed from tabulated stopping cross sections and substituted into Eq. (3.20) to find E . This method is most accurate for the analysis of thin-film spectra where the surface approximation holds. It is also useful for thicker films where the surface approximation is poor, because the ratio α of the energy losses changes less rapidly than ϵ .

3.3.2 Iterative Method

This method starts with the surface energy approximation in which $\bar{E}_{in} \simeq E_0$ and $\bar{E}_{out} \simeq KE_0$ and sets $[\bar{S}] = [S_0]$ or $[\bar{\epsilon}] = [\epsilon_0]$ to obtain a zeroth-order depth x at which scattering occurs by using Eq. (3.7) and a given value of $\Delta E = KE_0 - E_1$. Then, one calculates a zeroth-order E using dE/dx or ϵ evaluated at E_0 [Eq. (3.3)]. With this value of E , a new and improved estimate of \bar{E}_{in} and \bar{E}_{out} is obtained with Eqs. (3.15) and (3.16). These improved values of \bar{E}_{in} and \bar{E}_{out} define a first-order $[\bar{S}]$ or $[\bar{\epsilon}]$ [Eqs. (3.13)

and (3.14)]. The process can now be iterated to find still better estimates of x , E , and $[\bar{S}]$ or $[\bar{\epsilon}]$. The method converges rapidly and an accurate depth scale can be established.

3.3.3 Analytical Methods

To obtain analytical formulas for E , the functional dependence of dE/dx or $(dE/dx)^{-1}$ must be known analytically. Two methods have been described in the literature.

a. Taylor Expansion of ϵ . Since E_0 and E_1 are the experimentally accessible energies, it is natural to expand ϵ around those two points. These expansions can be used to find the values of ϵ at the mean energies \bar{E}_{in} and \bar{E}_{out} . It is assumed that these energies are given by the mean energy approximation, i.e., $\bar{E}_{in} = \frac{1}{2}(E + E_0)$ and $\bar{E}_{out} = \frac{1}{2}(E_1 + KE)$. By eliminating x from Eqs. (3.3) and (3.4) one obtains

$$\frac{(E_0 - E)}{(KE - E_1)} = \frac{(dE/dx)|_{E_{in}}}{(dE/dx)|_{E_{out}}} \beta^{-1} = \frac{\epsilon(\bar{E}_{in})}{\epsilon(\bar{E}_{out})} \beta^{-1}. \quad (3.23)$$

Note that the energy loss ratio method of Section 3.3.1 is based on the same relationship [Eq. (3.21)] except that \bar{E}_{in} and \bar{E}_{out} are evaluated at the surface values E_0 and KE_0 .

The Taylor expansion of ϵ below E_0 gives

$$\epsilon(\bar{E}_{in}) = \epsilon(E_0) - \frac{1}{2}(E_0 - E)\epsilon'(E_0) + \dots, \quad (3.24)$$

where $\epsilon'(E_0)$ is the derivative of ϵ with respect to energy taken at E_0 . The expansion of ϵ above E_1 gives, similarly,

$$\epsilon(\bar{E}_{out}) = \epsilon(E_1) + \frac{1}{2}(KE - E_1)\epsilon'(E_1) + \dots \quad (3.25)$$

By substituting these expansions for the ratio $\epsilon(\bar{E}_{in})/\epsilon(\bar{E}_{out})$, one obtains a quadratic expression for E :

$$aE^2 + bE + c = 0, \quad (3.26)$$

where

$$a = \frac{1}{2}K[\epsilon'(E_0)\beta^{-1} + \epsilon'(E_1)], \quad (3.27)$$

$$b = [K\epsilon(E_0)\beta^{-1} + \epsilon(E_1)] - \frac{1}{2}(KE_0 + E_1)[\epsilon'(E_1) + \epsilon'(E_0)\beta^{-1}], \quad (3.28)$$

and

$$c = \frac{1}{2}E_0E_1[\epsilon'(E_0)\beta^{-1} + \epsilon'(E_1)] - E_0\epsilon(E_1) - E_1\epsilon(E_0)\beta^{-1}. \quad (3.29)$$

The coefficients a , b , and c are expressed in terms of the known quantities E_0 , E_1 , K , β , and ϵ and ϵ' at E_0 and E_1 . Values of ϵ and ϵ' are given in Tables VI and VII. Therefore, a , b , and c can be written in terms of E_0 and E_1 , and E can be solved from Eq. (3.26). The method was introduced by Chu and Ziegler (1975).

b. Power Law Assumption for dE/dx . Another way to obtain the relation between the energy E before scattering and the depth x at which scattering takes place is to assume a functional dependence for ϵ or dE/dx such that the integrals in Eqs. (3.1) and (3.2) can be solved analytically. One approach (Behrisch and Scherzer, 1973) assumes that dE/dx can be approximated over an energy region by a power law in E , as $dE/dx = A_\nu E^\nu$. They assume that the exponent ν of the power dependence is a constant with values equal to $\frac{1}{2}$, 0, or -1 depending on the energy region where dE/dx is evaluated. When this power law expression for dE/dx is substituted into Eqs. (3.1) and (3.2) and the variable x is eliminated, one obtains

$$E = \left(\frac{E_1^{1-\nu} + \beta E_0^{1-\nu}}{K^{1-\nu} + \beta} \right)^{1/(1-\nu)}. \quad (3.30)$$

3.4 NUMERICAL METHODS TO FIND THE ENERGY E BEFORE SCATTERING

Numerical methods proceed from Eqs. (3.1) and (3.2) with tabulated values for dE/dx . With the first equation, (3.1), one computes a table of x values versus E values for the incident path. With the second equation, (3.2), one computes E_1 for each pair of values of x and E . This establishes a set of corresponding values of x , E , and E_1 for a given E_0 .

In practice, there are two different ways to do the numerical calculation. One approach is to divide the depth into many slabs of equal width Δx , as shown in Fig. 3.10. The calculation starts from the surface layer. The thickness Δx is made thin enough so that dE/dx is practically constant over the width Δx . The energies at the two boundaries of the $(n+1)$ th slab can be related to each other by the recursion relation

$${}_{(n+1)}E = {}_nE - \frac{dE}{dx} \Big|_{{}_nE} \left(\frac{x}{\cos \theta_1} \right). \quad (3.31)$$

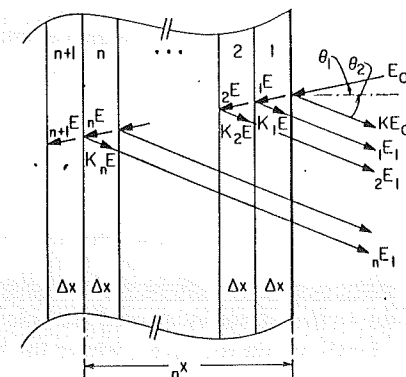


Fig. 3.10 Concept and symbols used in the numerical method of calculating the energy E before scattering at depth x and the corresponding detected energy E_1 at the detector.

In this way one obtains the energy of the incident particles before scattering at each slab boundary. Upon scattering, the energy of the particle is reduced by the kinematic factor K . Along the outgoing path, the energy lost in each slab is equal to the product of dE/dx evaluated at the local energy and the effective path length $x/\cos\theta_2$. The emerging particles will have energies ${}_1E_1, {}_2E_1, \dots, {}_nE_1$, and ${}_{n+1}E_1$, etc., where ${}_nE_1$ is the energy of a particle emerging after a collision in the n th slab; therefore,

$${}_1E_1 = K {}_1E - \frac{\Delta x}{\cos\theta_2} \frac{dE}{dx} \Big|_{K {}_1E} \quad (3.32)$$

The energy ${}_2E_1$ of an emerging particle scattered after traversing inward and outward through two slabs is

$${}_2E_1 = \left(K {}_2E - \frac{\Delta x}{\cos\theta_2} \frac{dE}{dx} \Big|_{K {}_2E} \right) - \frac{\Delta x}{\cos\theta_2} \frac{dE}{dx} \Big|_{\text{energy at 1,2 interface}} \quad (3.33)$$

The energy at the 1,2 interface at which the last term must be evaluated is identical to that given in the parentheses preceding that last term. Iterating this procedure, one can write

$${}_nE_1 = \left(\left(\left(\left(K {}_nE - \frac{\Delta x}{\cos\theta_2} \frac{dE}{dx} \Big|_{K {}_nE} \right) - \frac{\Delta x}{\cos\theta_2} \frac{dE}{dx} \Big|_{(E)} \right) - \frac{\Delta x}{\cos\theta_2} \frac{dE}{dx} \Big|_{((E))} \right) - \frac{\Delta x}{\cos\theta_2} \frac{dE}{dx} \Big|_{(((E)))} \right) \dots \quad (3.34)$$

where each dE/dx is evaluated at a local energy which is given in the parentheses preceding the term and from which it is subtracted.

The other approach is to divide the sample into thin slabs of differing thicknesses chosen such that particles scattered from the two boundaries of all slabs have a fixed energy difference \mathcal{E} at the detector. This procedure has the advantage that it reproduces the subdivision of the energy E_i into equal increments, as a multichannel analyzer really does.

It is also convenient to perform numerical calculations when dE/dx can be expressed as a function of E analytically. This is usually done by fitting a polynomial to dE/dx or ϵ . For the purpose of numerical calculations such fits are presented in Table VII.

3.5 HEIGHT OF AN ENERGY SPECTRUM FOR AN ELEMENTAL SAMPLE

In the previous sections we have discussed the relation between the energy of the detected backscattered particle (abscissa of an energy spectrum) and the depth within the target where the backscattering events occurred. In the

next few sections we develop the relation between the height of the energy spectrum (ordinate of an energy spectrum) and the number of scattering centers per unit area within the sample where backscattering occurs. In the remaining sections of this chapter, only stopping cross sections ϵ and stopping cross section factors $[S]$ will be used. A conversion to dE/dx or $[S]$ can always be made [Eqs. (3.7) and (3.9)].

According to the preceding sections, the energy axis of a backscattering spectrum and the depth below the surface of a sample are uniquely related to each other by a functional dependence such as that shown in Fig. 3.9. Each energy width \mathcal{E} of a channel i in the multichannel analyzer is thus imaged within the sample by a slab i of thickness τ_i from which all the backscattering events recorded in channel i emanate. The number of counts H_i in channel i is thus determined by two factors: the thickness τ_i of the slab and the number of scattering centers (atoms) in that slab. The basic problem then is to relate the number of counts H_i to the number of scattering centers per unit area $N\tau_i$ in the slab of thickness τ_i at depth x_i which corresponds to the energy width \mathcal{E} and the position $E_{1,i}$ of channel i in the energy spectrum, as indicated in Fig. 3.11.

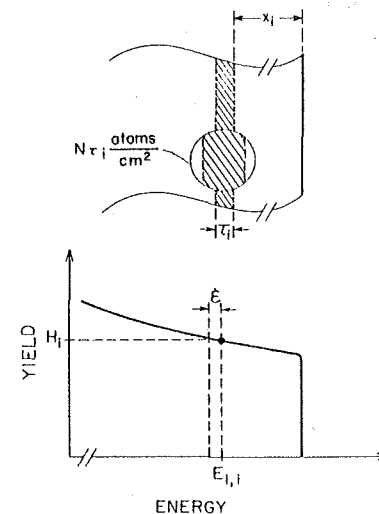


Fig. 3.11 Schematic showing the correspondence between (a) slab i at depth x_i in a monoisotopic sample and (b) channel i at energy $E_{1,i}$. The width \mathcal{E} of every channel is the same, but the width τ_i of the slabs is not.

Assume for the time being that the width τ_i is known. (The method for determining this width is explained later in this section.) It then follows from Eq. (2.19) that for a beam of normal incidence the total number of particles detected in channel i is $H_i = \sigma(E_i)\Omega Q N\tau_i$, where $\sigma(E_i)$ is the differential cross section evaluated at energy E_i and averaged over the finite solid angle Ω spanned by the detector, Q is the total number of particles incident on the

sample, and N is the atomic density of the sample element. This result is correct only for a normal incidence of the beam, because then $N\tau_i$ correctly gives the number of target atoms in a unit of area perpendicular to the beam. For other angles of incidence, i.e., for $\theta_1 > 0$, the trajectory of the beam across the slab i has a length $\tau_i/\cos\theta$, not τ_i . The number of atoms per unit area as seen by the beam is therefore increased by $1/\cos\theta_1$, so that for this general case

$$H_i = \sigma(E_i)\Omega Q N \tau_i / \cos\theta_1. \quad (3.35)$$

It will be seen that the value and the position of τ_i also change as the beam is tilted from a normal to a slanted incidence, e.g., (3.35) holds for the value of τ_i applicable to the particular geometrical arrangement under consideration.

The shape and the height of the backscattering energy spectrum were first treated in the early 1950s (Wenzel, 1952). Several different versions of the analytical form of the backscattering yield exist and are well documented (Wenzel and Whaling, 1952; Van Wijngaarden *et al.*, 1970; Powers, 1961). Although the notation differs, all the approaches are conceptually the same. Approximations have been applied in some cases to simplify the problem and the mathematics. We will start with the simplified case and progress to the general form.

3.5.1 Spectrum Height for Scattering from the Top Surface Layer

Consider the backscattering spectrum obtained from a thick sample and focus attention on the backscattering events that take place either at the surface of the sample or near the surface region. For this region the analysis is simplified because the energy before scattering can be taken as E_0 and is therefore known. Figure 3.12 gives a schematic of the backscattering processes in this surface region, and the resulting spectrum. The notation adopted for the near-surface region is H_0 and τ_0 in contrast to H_i and τ_i for regions within the sample. For the surface region Eq. (3.35) then becomes

$$H = \sigma(E_0)\Omega Q N \tau_0 / \cos\theta_1 \equiv H_0. \quad (3.36)$$

The subscript is often dropped from H because of the widespread use of this symbol in this particular context. The thickness τ_0 is defined by the energy width \mathcal{E} of a channel. Particles scattered from atoms within τ_0 will have energies between KE_0 and $KE_0 - \mathcal{E}$. From Eqs. (3.9) and (3.12) the depth scale at the surface is given by

$$\mathcal{E} = [\varepsilon_0] N \tau_0. \quad (3.37)$$

The corresponding expression in terms of the energy loss factor is $\mathcal{E} = [S_0]\tau_0$. As stated previously, we shall retain only the formulation in terms of ε and

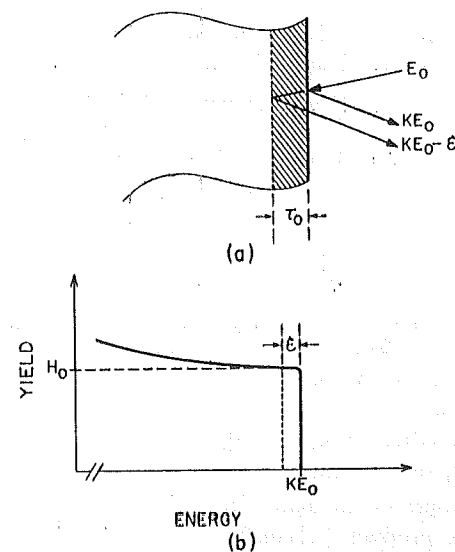


Fig. 3.12 Schematic of the backscattering process in the surface region of a sample consisting of a monoisotopic element (a) and the resulting spectrum (b).

$[\varepsilon]$ in the remainder of this chapter. Substituting Eq. (3.37) in (3.36) to eliminate $N\tau_0$ yields

$$H_0 = \sigma(E_0)\Omega Q \mathcal{E} / [\varepsilon_0] \cos\theta_1. \quad (3.38)$$

This equation states that the height of the energy spectrum at the surface is directly proportional to

- (i) Q , the total number of incident projectiles bombarding the sample;
- (ii) $\sigma(E_0)$, the average differential scattering cross section between the projectile and the sample evaluated at the incident energy E_0 ;
- (iii) Ω , the solid angle spanned by the detector aperture;
- (iv) \mathcal{E} , the energy width of a channel, which is determined by the electronic setting of the detecting system; and
- (v) $([\varepsilon_0] \cos\theta_1)^{-1}$, the inverse of the stopping cross section factor evaluated at the surface for a given scattering geometry multiplied by the cosine of the angle of incidence of the beam against the sample normal.

The direct proportionality of H_0 to Q , σ , Ω , and \mathcal{E} is physically evident. The inverse proportionality of H_0 to $[\varepsilon_0] \cos\theta_1$ can be understood by considering the energy that particles lose on their inward and outward paths through the surface layer. Consider first the case of normal incidence. If the stopping cross section is high, then so is the stopping cross section factor $[\varepsilon_0]$. A fixed energy is then dissipated by the moving particle over fewer

atomic layers than if $[\epsilon_0]$ were small. This means that the larger $[\epsilon_0]$ is, the smaller will be the number of scattering processes for the fixed energy interval \mathcal{E} . For example, compare two target materials A and B, where A has a larger stopping cross section factor than B. For the same energy loss, the projectile will have fewer encounters with A atoms than B. Thus there will be fewer backscattering events that produce counts within a given channel for target A than for target B (neglecting differences in σ).

Consider next the case of fixed stopping cross section but varying angle of incidence θ_1 . Changing θ_1 has a twofold effect: the thickness of the slab corresponding to the single channel of the multichannel analyzer undergoes a change expressed by the factor $[\epsilon_0]^{-1}$, and the number of atoms per unit of an area perpendicular to the beam undergoes a change expressed by the factor $(\cos \theta_1)^{-1}$. These two effects tend to cancel because one of the two terms of $[\epsilon_0]$ goes as $(\cos \theta_1)^{-1}$ [Eq. (3.11)]. This is the reason for considering the product $[\epsilon_0] \cos \theta_1$ rather than the individual terms when discussing the dependence on the angle of incidence θ_1 of the beam. In general, signal heights depend on the product $([\epsilon] \cos \theta_1)^{-1}$, whereas depth-to-energy-loss conversions depend on $[\epsilon]$ only [compare, e.g., Eqs. (3.7) or (3.9) and (3.44)]. Because signal heights depend on the product $[\epsilon] \cos \theta_1$, some authors introduce the *effective stopping cross section factor* $\epsilon_{\text{eff}} \equiv [\epsilon] \cos \theta_1$, which is the natural parameter to introduce when the interest focuses on the height of a spectrum.

Observe that the height H_0 does not depend on the atom density N of the sample. This is a general property of backscattering yields. The matter is discussed in Section 3.9.

3.5.2 Spectrum Height for Scattering at a Depth

The essence of depth profiling is to relate a spectrum height H_i to a slab of material with thickness τ_i and number of atoms per unit area $N\tau_i$ at depth x_i . From Eq. (3.35) the height is

$$H_i = \sigma(E_i) \Omega Q N \tau_i / \cos \theta_1. \quad (3.39)$$

The cross section σ is evaluated here at the energy E_i of the projectile immediately before scattering at depth x_i (see Section 3.3). The amount of material $N\tau_i$ is defined by the energy width \mathcal{E} such that the particles backscattered from the slab will emerge from the sample with energies between $E_{1,i}$ and $E_{1,i} - \mathcal{E}$. It would be wrong to conclude therefore that the energy width \mathcal{E}' of these particles immediately after scattering is also \mathcal{E} . The reason is that particles with slightly different energies after scattering at x_i undergo slightly different energy losses on their outward path, so that $\mathcal{E}' \neq \mathcal{E}$. To be precise, the energy lost along the outgoing path reduces KE_i to $E_{1,i}$ while $(KE_i - \mathcal{E}')$ is reduced to $(E_{1,i} - \mathcal{E})$. This is sketched in Fig. 3.13a.

etc!

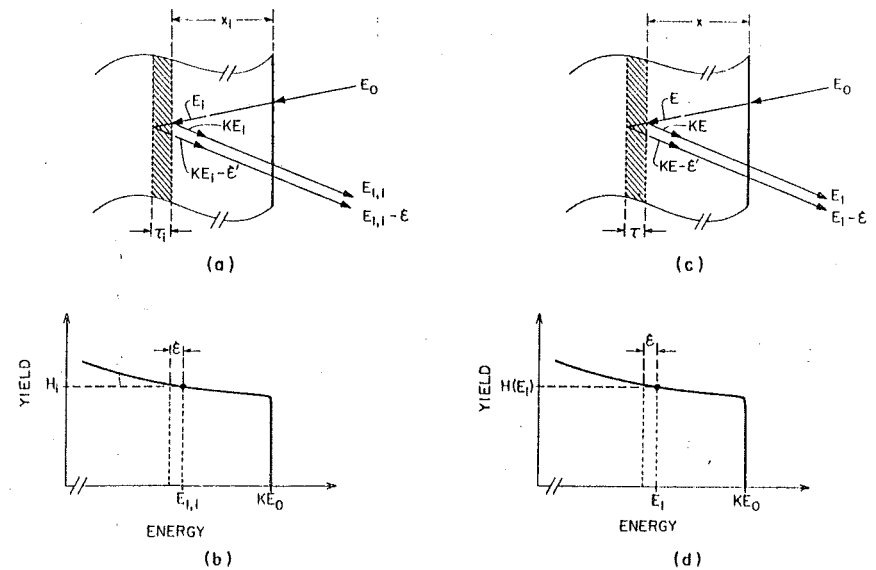


Fig. 3.13 Schematics of and nomenclature for (a) the backscattering process at depth x_i within a monoisotopic sample in the language of discrete functions, and (b) the resulting spectrum. (c) and (d) give the corresponding schematics and nomenclature in the language of continuous functions.

Before developing further the subject of the spectrum height for scattering below the surface, it is appropriate at this point to introduce a more efficient notation. The subscript i in the preceding equations indicates that the quantities considered refer to a specific slab i and its corresponding channel i at energy $E_{1,i}$ in the multichannel analyzer. With this subscript, the equations are cumbersome to read and to write. When it is understood that the quantities discussed here are really discrete, the subscript i need not be retained, and Eq. (3.39) can be written as

$$H(E_1) = \sigma(E) \Omega Q N \tau / \cos \theta_1. \quad (3.40)$$

The cross section σ is now a function of a continuous variable E , the energy of the particle immediately before scattering at any depth x within the sample. Similarly, H is a function of the continuous variable E_1 , the energy of a detected particle, and τ is the thickness of a slab (at any depth x) that produces particles detected in the energy interval \mathcal{E} , the energy width of a channel in the multichannel analyzer. As was previously explained, this energy interval differs from the interval \mathcal{E}' that these same particles span immediately after scattering from a slab of thickness τ at depth x . These definitions and the new notation are explained in Figs. 3.13c and d.

We now return to the derivation of the spectrum height $H(E_1)$ for scattering at a depth x below the surface. The surface energy approximation cannot be used, since the energy E before the collision may differ noticeably from E_0 . Consequently, the thickness τ of a slab at depth x may differ from that of τ_0 at the surface. We shall therefore solve the problem by first calculating the thickness τ of a slab in terms of the energy interval \mathcal{E}' . Then we shall express the energy interval \mathcal{E}' in terms of the interval \mathcal{E} located at an energy E_1 in the energy spectrum.

To find the relation between τ and \mathcal{E}' , note that the particles scattered at opposite interfaces of the slab at depth x can be viewed as a backscattering process at a surface covered by a layer of thickness x . The particles incident on this surface have an energy E , and the energy difference corresponding to scattering at the opposite interfaces of the slab there is \mathcal{E}' . Exactly the same condition would prevail at the actual surface of the sample if the incident energy E_0 were reduced to E and the energy width per channel were set to \mathcal{E}' rather than \mathcal{E} at the multichannel analyzer. It therefore follows from Eq. (3.37) that

$$\mathcal{E}' = [\varepsilon(E)]N\tau. \quad (3.41)$$

The stopping cross section factor $[\varepsilon(E)]$ which appears in this equation is defined in analogy to Eq. (3.12) as

$$[\varepsilon(E)] \equiv \frac{K}{\cos \theta_1} \varepsilon(E) + \frac{1}{\cos \theta_2} \varepsilon(KE) \quad (3.42)$$

and there exists a corresponding energy loss factor

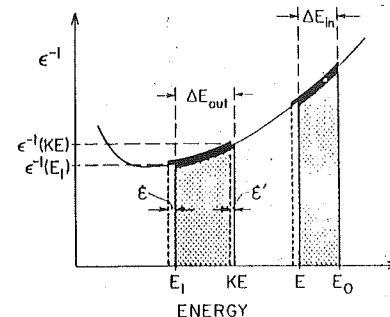
$$[S(E)] \equiv \frac{K}{\cos \theta_1} \frac{dE}{dx} \Big|_E + \frac{1}{\cos \theta_2} \frac{dE}{dx} \Big|_{KE} \quad (3.43)$$

defined in analogy to Eq. (3.11). The interpretation of this energy loss factor in terms of Fig. 3.9 is as follows: $[S(E)]$ is the slope (dashed curve) at the origin of the energy loss versus depth curve, which is measured for particles of incident energy E , rather than E_0 . In other words, $[S(E)]$ gives the depth scale of a spectrum in the surface energy approximation when the incident energy of the particles is E . With τ expressed in terms of \mathcal{E}' , the height $H(E_1)$ of the spectrum becomes

$$H(E_1) = \sigma(E)\Omega Q(\mathcal{E}'/[\varepsilon(E)] \cos \theta_1). \quad (3.44)$$

This expression for H is incomplete in that \mathcal{E}' is not an experimentally accessible quantity, while \mathcal{E} is. The second step is thus to express \mathcal{E}' in terms of the energy interval \mathcal{E} at a position E_1 on the energy scale of a spectrum. The answer is obtained by considering the energy loss of backscattered particles along their outward path. Consider two particles whose energies

Fig. 3.14 Graphical interpretation of Eq. (3.46). The light line gives ε^{-1} versus energy. The heavy segments indicate the ε^{-1} and energy values for two particles along their inward and outward tracks. One particle loses slightly more energy than the other. A difference \mathcal{E}' in the particle energy immediately after scattering produces an energy difference \mathcal{E} when the particles emerge from the sample. The two shaded areas for the outward paths must be equal.



immediately after backscattering at depth x differ by \mathcal{E}' . The energy loss along the outward path is given by Eq. (3.2) or

$$\frac{\partial E}{\partial x} = -EN\frac{K}{\cos \theta_2} \quad N\tau/\cos \theta_2 = -\int_{KE}^{E_1} dE/\varepsilon. \quad (3.45)$$

Since the slab τ is very thin compared to the depth of scattering, one can assume that scattering from the same depth with different energies approximates closely the real situation where particles scatter from the front and rear surfaces of the slab. The outward path thus is essentially the same for both particles and the right-hand side has the same value in both cases; hence

$$\int_{KE}^{E_1} dE/\varepsilon = \int_{KE-\mathcal{E}'}^{E_1-\mathcal{E}'} dE/\varepsilon \quad (3.46)$$

must hold. By assumption of the model, \mathcal{E}' and \mathcal{E} are small compared to KE and E_1 and can be treated as differentials, so that $\mathcal{E}'/\varepsilon(E_1) = \mathcal{E}'/\varepsilon(KE)$, or

$$\mathcal{E}'/\mathcal{E} = \varepsilon(KE)/\varepsilon(E_1). \quad (3.47)$$

The graphical interpretation of this result is sketched in Fig. 3.14. Because the two particles traverse the same layer on their outward path, it is the area under the ε^{-1} curve that must be conserved. Equation (3.47) then follows at once.

If there is little difference between $\varepsilon(KE)$ and $\varepsilon(E_1)$, a linear interpolation between these two values provides a reasonable approximation to ε . Then $\varepsilon(KE) \approx \varepsilon(E_1) + \Delta E_{out} \varepsilon'(\bar{E}_{out})$, where $\varepsilon'(\bar{E}_{out})$ is the derivative of ε with respect to energy, evaluated at some intermediate energy \bar{E}_{out} along the outward path. When this expression for $\varepsilon(KE)$ is used for the ratio $\varepsilon(KE)/\varepsilon(E_1)$, one obtains (Feng *et al.*, 1973)

$$\frac{\mathcal{E}'}{\mathcal{E}} = 1 + \frac{\Delta E_{out}}{\varepsilon(E_1)} \varepsilon'(\bar{E}_{out}) \quad (3.48)$$

$$\approx 1 + \frac{N\tau}{\cos \theta_2} \varepsilon'(\bar{E}_{out}). \quad (3.49)$$

This expression shows that the difference between \mathcal{E}' and \mathcal{E} increases with the length $x/\cos \theta_2$ of the outward path. It also shows that $\mathcal{E}' \simeq \mathcal{E}$ for particles scattered from the surface region of the sample because x is small there.

With Eq. (3.47), the yield $H(E_1)$ from a slab located at depth x given by Eq. (3.44) becomes

$$H(E_1) = \sigma(E)\Omega Q \frac{\mathcal{E}}{[\varepsilon(E)] \cos \theta_1} \frac{\varepsilon(KE)}{\varepsilon(E_1)} \quad (3.50)$$

In the discrete notation of Fig. 3.13a and b, this formula takes the form

$$H_i = \sigma(E_i)\Omega Q \frac{\mathcal{E}}{[\varepsilon(E_i)] \cos \theta_1} \frac{\varepsilon(KE_i)}{\varepsilon(E_{1,i})} \quad (3.51)$$

The physical interpretation of this result is as follows: As the incident beam penetrates the sample the energy of the projectiles decreases. As a consequence the scattering cross section $\sigma(E)$ increases. This effect tends to increase the yield $H(E_1)$ with decreasing energy E_1 of the detected particles. On the other hand, the stopping cross section ε also varies with E . In general this dependence is not as strong as that for $\sigma(E)$, but ε can either increase or decrease with decreasing values of E (Fig. 3.7). Consequently, the effect of the change in ε on the backscattering yield may either enhance or counteract the effect of the change in σ . Specifically, when ε increases with decreasing energy the effect is to decrease the yield as expressed by the inverse proportionality to $[\varepsilon(E)]$. The contribution from the change in the ratio $\varepsilon(KE)/\varepsilon(E_1)$ is of lesser importance. [The application of Eq. (3.50) will be discussed in Section 5.5.2.]

Alternative derivations of the thick-target yield have been given for uniform targets (Wenzel, 1952) and for nonuniform targets (Wenzel and Whaling, 1952; Powers and Whaling, 1962). Recent work on the thick-target yield has emphasized specific aspects such as the influence of energy straggling (Van Wijngaarden *et al.*, 1970; Brice, 1973), the influence of scattering geometry (Jack, 1973), the dependence on energy loss (Behrisch and Scherzer, 1973; Siritonin *et al.*, 1971, 1972), and analytical formulations (Chu and Ziegler, 1975).

3.6 DEPTH SCALE FOR A HOMOGENEOUS SOLID CONTAINING MORE THAN ONE ELEMENT (COMPOUND SAMPLE)

In this section, we shall discuss the backscattering spectrum of a sample composed of a homogeneous mixture of several elements. For simplicity we denote the material as a *compound sample* although it could be either a mixture or a chemical compound. This case differs from that of the mono-

isotopic elemental sample considered thus far in this chapter in two significant ways. First, as the probing particles penetrate the film, they lose energy as the result of interactions with more than one element. Consequently, the stopping cross section depends on the composition of the sample. Second, when the probing particles with energy E are scattered at a specific depth within the sample, the value of the kinematic factor K and the scattering cross section σ will depend on the particular mass (atomic number) of the atom they strike. Since the stopping cross section varies with energy, the energy that the particles lose along identical outward tracks also depends on the atom struck in the scattering collision. For a compound sample, the yield of the backscattering spectrum and the energy-to-depth conversion thus depend on the element struck in the collision. All counts generated by backscattering from a given element constitute the signal of this element in the spectrum.

In the rest of this section and in Section 3.7 we shall consider the particular case of a sample composed of two monoisotopic elements A and B. The extension to the general case of a multielemental compound sample is straightforward. We also assume that the sample is homogeneous, i.e., of uniform composition both in lateral dimensions and in depth.

3.6.1 Stopping Cross Section Factor $[\varepsilon]$

To relate the energy E_1 of the detected particle to the depth x at which the backscattering event occurs, we shall follow the formalism described in Section 3.2 for the depth scale of an elemental target. We use a subscript to indicate the atom struck, so that E_{1A} and E_{1B} denote the energies of detected particles scattered from atoms A and B, respectively. Superscripts are used to denote the stopping medium, so that $\varepsilon^{A_m B_n}$ is the stopping cross section of a material containing elements A and B in the atomic ratio m/n . For a compound, m and n are integers; for a solid solution, for example, they need not be. In the spirit of Section 2.5 we shall give preference to the abbreviated notation ε^{AB} for $\varepsilon^{A_m B_n}$, even if m and n are not unity. From Chapter 2, the stopping cross section $\varepsilon^{A_m B_n}$ of the sample is given by $m\varepsilon^A + n\varepsilon^B$, assuming that Bragg's rule for the linear additivity of stopping cross sections holds true. Examples of the application of that rule are given in Section 5.4.

For the scattering geometry shown in Fig. 3.15, a particle penetrating the sample to a depth x undergoes an energy loss ΔE_{in} along the inward path given by

$$\Delta E_{in} = (N^{AB}x/\cos \theta_1)\varepsilon_{in}^{AB}, \quad (3.52)$$

where N^{AB} is the number of molecules $A_m B_n$ per unit volume. The energy loss ΔE_{out} along the outgoing path depends on the collision partner. Therefore, the energy difference ΔE between particles scattered at the front surface

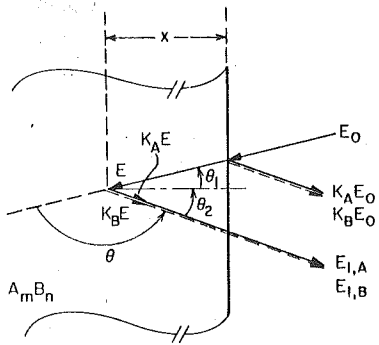


Fig. 3.15 Symbols used in the description of backscattering events in a compound sample composed of a homogeneous mixture of two monoisotopic elements A and B.

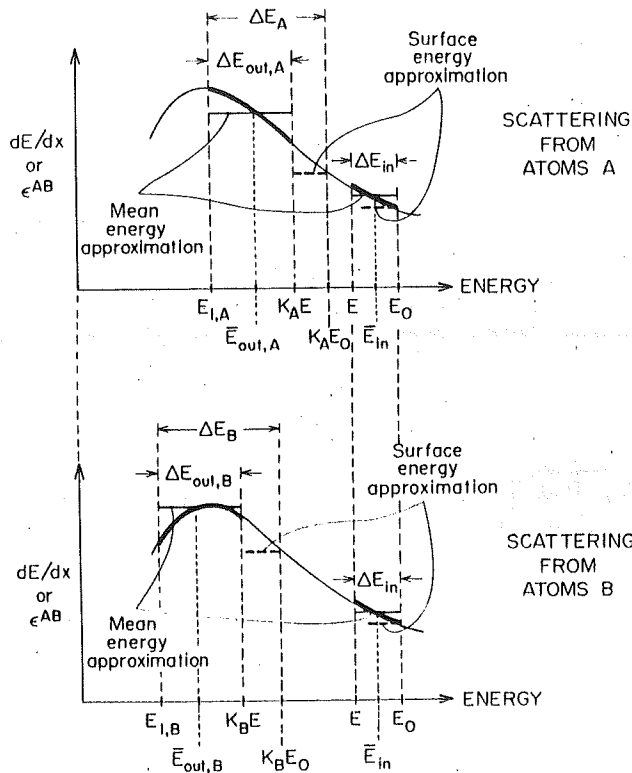


Fig. 3.16 Graphical representations of the energy loss of particles along their inward and outward paths (heavy lines) through a sample composed of a homogeneous mixture of two monoisotopic elements A and B. The light line is the functional form of dE/dx versus E . Since $dE/dx = N^{AB} \epsilon^{AB}$, the same plots apply to ϵ^{AB} versus E as well. Particles scattered at the two elements cover different energy ranges along their outward paths. The top of the figure applies for scattering by the heavy atom A; the bottom of the figure is for scattering by the atom B which is lighter than A. (Compare this with the corresponding parts of Fig. 3.7 for a monoisotopic sample.)

and at a depth x can have two values, ΔE_A or ΔE_B , depending on whether the particles scatter from atom A or atom B. The situation is represented graphically in Fig. 3.16 in a way corresponding to Fig. 3.7a. Notice the two different energy regions covered by particles scattered by atoms A and B. Thus there are now two depth scales, one attached to each signal, as shown for a single element in Fig. 3.8. These scales are in general different, but not by more than 10% in most cases for megaelectron volts of ^4He .

In analogy with the result of Section 3.2 for an elemental sample, we thus have

$$\Delta E_A = [\epsilon]_A^{AB} N^{AB} x \quad (3.53)$$

and

$$\Delta E_B = [\epsilon]_B^{AB} N^{AB} x, \quad (3.54)$$

where

$$[\epsilon]_A^{AB} = \frac{K_A}{\cos \theta_1} \epsilon_{in}^{AB} + \frac{1}{\cos \theta_2} \epsilon_{out,A}^{AB}, \quad (3.55)$$

$$[\epsilon]_B^{AB} = \frac{K_B}{\cos \theta_2} \epsilon_{in}^{AB} + \frac{1}{\cos \theta_1} \epsilon_{out,B}^{AB}. \quad (3.56)$$

These *generalized stopping cross section factors* contain the special case of an elemental sample composed of elements A or B only as $[\epsilon]_A^A$ or $[\epsilon]_B^B$ [see Eq. (3.10)]. As shown in Section 3.2 for elemental stopping cross section factors, approximations can be used to evaluate the stopping cross sections on the inward path ϵ_{in}^{AB} and on the outward paths $\epsilon_{out,A}^{AB}$ and $\epsilon_{out,B}^{AB}$ for particles scattered from atoms A or B. The discussion given there applies to the present case of a compound sample as well. The next section repeats this treatment in brief.

3.6.2 Approximations to $[\epsilon]$

For regions near the surface, the thickness x is small and the relative changes of energy along the incident and outward path are small also. Therefore, in analogy to Eq. (3.12) one gets

$$[\epsilon_0]_A^{AB} = \frac{K_A}{\cos \theta_1} \epsilon^{AB}(E_0) + \frac{1}{\cos \theta_2} \epsilon^{AB}(K_A E_0) \quad (3.57)$$

and

$$[\epsilon_0]_B^{AB} = \frac{K_B}{\cos \theta_1} \epsilon^{AB}(E_0) + \frac{1}{\cos \theta_2} \epsilon^{AB}(K_B E_0), \quad (3.58)$$

where the symbols $[E_0]_A^{AB}$ and $[E_0]_B^{AB}$ are used to denote the surface energy approximation to the stopping cross section factor for particles scattered from atoms A and B, respectively.

Similarly, one defines $[\bar{E}]_A^{AB}$ and $[\bar{E}]_B^{AB}$ as the mean energy approximation. For the inward path, $\bar{E}_{in} = \frac{1}{2}(E + E_0)$, as given in Eq. (3.15). However, the intermediate energy \bar{E}_{out} along the outward path is different for particles scattered from atoms A and B and must be specified for each case. Following Eq. (3.16),

$$\bar{E}_{out,A} = \frac{1}{2}(E_{1,A} + K_A E) \quad (3.59)$$

and

$$\bar{E}_{out,B} = \frac{1}{2}(E_{1,B} + K_B E), \quad (3.60)$$

where $E_{1,A}$ and $E_{1,B}$ refer to the detected energy of particles scattered at a depth x from atoms A and B, respectively. The locations of $\bar{E}_{out,A}$ and $\bar{E}_{out,B}$ for the mean energy approximation are shown in Fig. 3.16 also.

The value of E can be found from the methods described in Section 3.3 or estimated from the symmetrical mean energy approximation, in which case the values of \bar{E}_{in} and \bar{E}_{out} for the signals from A and B are then given by

$$\bar{E}_{in,A} = E_0 - \frac{1}{4}\Delta E_A, \quad (3.61)$$

$$\bar{E}_{in,B} = E_0 - \frac{1}{4}\Delta E_B, \quad (3.62)$$

$$\bar{E}_{out,A} = E_{1,A} + \frac{1}{4}\Delta E_A, \quad (3.63)$$

$$\bar{E}_{out,B} = E_{1,B} + \frac{1}{4}\Delta E_B, \quad (3.64)$$

in analogy with Eqs. (3.17) and (3.18). Note that in this case different values of E and \bar{E}_{in} are used for the different collision partners.

3.7 HEIGHT OF AN ENERGY SPECTRUM FOR A HOMOGENEOUS SOLID CONTAINING MORE THAN ONE ELEMENT (COMPOUND SAMPLE)

In the preceding section we established the connection between the energy of a detected backscattered particle and the depth within the homogeneous compound sample where scattering occurs. In this section we shall discuss the height of the backscattering spectrum of such a compound sample. Again we shall consider in detail the case of a mixture of two monoisotopic elements A and B. The extension to a multielemental compound sample is straightforward.

The backscattering spectrum of such a compound sample is sketched in Fig. 3.17b. This energy spectrum consists of a superposition of the two signals

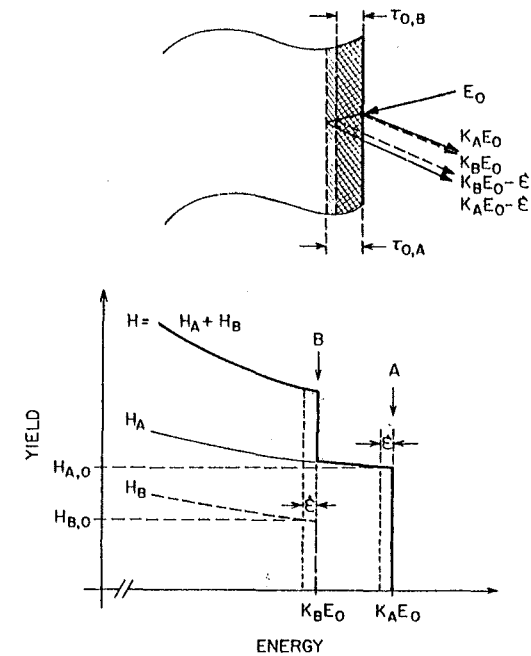


Fig. 3.17 Schematic of the backscattering process in the surface region of a sample composed of a homogeneous mixture of two monoisotopic elements A and B (a), and the resulting spectrum (b).

generated by the elements A and B in the sample. The edge of each signal is defined by the kinematic factor K of these two elements. For the example shown, $K_A > K_B$; that is, A is the heavier of the two atomic species. If $H_A(E_1)$ and $H_B(E_1)$ are the heights of the individual signals generated by particles detected with energy E_1 after scattering from elements A and B, the height of the total spectrum H at that energy is given generally by

$$H(E_1) = H_A(E_1) + H_B(E_1). \quad (3.65)$$

We shall develop the shape of this total spectrum by first considering scattering from the top surface region.

3.7.1 Spectrum Height for Scattering from the Top Surface Layer

For backscattering processes near the sample surface, the energy before scattering can be taken as E_0 . The expression for scattering from elements

A and B can then be taken directly from that for an elemental target [Eq. (3.36)] to give

$$H_{A,0} = \sigma_A(E_0)\Omega Q N_A^{AB}(\tau_{A,0}/\cos\theta_1) \quad (3.66)$$

and

$$H_{B,0} = \sigma_B(E_0)\Omega Q N_B^{AB}(\tau_{B,0}/\cos\theta_1), \quad (3.67)$$

where N_A^{AB} and N_B^{AB} are the number of atoms A and B per unit volume. The thicknesses $\tau_{A,0}$ and $\tau_{B,0}$ are chosen such that particles scattered within these slabs will have energies between $K_A E_0$ and $K_A E_0 - \mathcal{E}$ or $K_B E_0$ and $K_B E_0 - \mathcal{E}$. There are two such surface slabs now, because the energy lost along the outward path for particles scattered by atom A differs from that for particles scattered by atom B. This is shown schematically in the diagram of Fig. 3.17a. These two widths thus satisfy the conditions

$$\mathcal{E} = [\varepsilon_0]_A^{AB} N_A^{AB} \tau_{A,0} \quad (3.68)$$

and

$$\mathcal{E} = [\varepsilon_0]_B^{AB} N_B^{AB} \tau_{B,0}, \quad (3.69)$$

where N^{AB} is the number of molecular units $A_m B_n$ per unit volume. Since $N_A^{AB} = m N^{AB}$ and $N_B^{AB} = n N^{AB}$, the surface heights can be written as

$$H_{A,0} = \sigma_A(E_0)\Omega Q m (\mathcal{E}/[\varepsilon_0]_A^{AB} \cos\theta_1) \quad (3.70)$$

and

$$H_{B,0} = \sigma_B(E_0)\Omega Q n (\mathcal{E}/[\varepsilon_0]_B^{AB} \cos\theta_1). \quad (3.71)$$

The ratio of these heights is

$$\frac{H_{A,0}}{H_{B,0}} = \frac{\sigma_A(E_0) m [\varepsilon_0]_B^{AB}}{\sigma_B(E_0) n [\varepsilon_0]_A^{AB}} \quad (3.72)$$

To determine the ratio m/n from a backscattering spectrum, the ratio $[\varepsilon_0]_B^{AB}/[\varepsilon_0]_A^{AB}$ can be taken as unity in a zeroth-order approximation. This ratio actually approaches unity within 10% in most cases for He ion energies of 1 to 2 MeV; thus

$$m/n \simeq [H_{A,0}/\sigma_A(E_0)]/[H_{B,0}/\sigma_B(E_0)]. \quad (3.73)$$

From this zeroth-order approximation, one can then obtain a better estimate of the ratio $[\varepsilon_0]_B^{AB}/[\varepsilon_0]_A^{AB}$ and hence a first-order approximation to m/n . Typically, this first iteration is sufficient to give a value of the ratio m/n within the errors of the experimental data.

3.7.2 Spectrum Height for Scattering at a Depth

The calculation of the spectrum height $H(E_1)$ for particles detected at energy E_1 is complicated by the fact that the signals generated by scattering from atoms A and atoms B have different depth scales. That is, particles escaping the sample with the same detected energy E_1 are scattered from atoms A at a depth x_A , whereas those scattered from atoms B come from a depth $x_B \neq x_A$ (see Fig. 3.18a). Thus the energies E_A and E_B of the particles immediately before scattering will differ. In analogy to Eq. (3.44), the height of each signal can be written as

$$H_A(E_1) = \sigma(E_A)\Omega Q m (\mathcal{E}'_A/[\varepsilon(E_A)]_A^{AB} \cos\theta_1) \quad (3.74)$$

and

$$H_B(E_1) = \sigma(E_B)\Omega Q n (\mathcal{E}'_B/[\varepsilon(E_B)]_B^{AB} \cos\theta_1), \quad (3.75)$$

where \mathcal{E}'_A and \mathcal{E}'_B are the energy intervals spanned by particles immediately after scattering within the slabs of thickness τ_A and τ_B at depth x_A and x_B . One

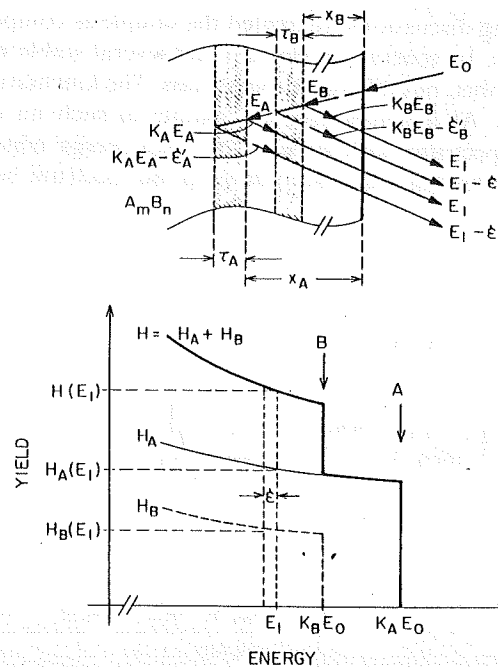


Fig. 3.18 Schematic of the backscattering process at some depth within a sample composed of a homogeneous mixture of two monoisotopic elements A and B (a), and the resulting spectrum (b).

can relate the energies \mathcal{E}'_A and \mathcal{E}'_B to \mathcal{E} by the procedure developed in connection with Eq. (3.47). The result is

$$H_A(E_1) = \sigma_A(E_A)\Omega Qm \frac{\mathcal{E}}{[\varepsilon(E_A)]_A^{AB} \cos \theta_1} \frac{\varepsilon^{AB}(K_A E_A)}{\varepsilon^{AB}(E_1)}, \quad (3.76)$$

$$H_B(E_1) = \sigma_B(E_B)\Omega Qn \frac{\mathcal{E}}{[\varepsilon(E_B)]_B^{AB} \cos \theta_1} \frac{\varepsilon^{AB}(K_B E_B)}{\varepsilon^{AB}(E_1)}, \quad (3.77)$$

and corresponds to Eq. (3.50) for the elemental case. As is true there, the last factor with the ratio in stopping cross sections is of lesser importance. The main changes as compared with the surface heights $H_{A,0}$ and $H_{B,0}$ come from variations in the cross sections σ_A and σ_B and the stopping cross section factors $[\varepsilon]_A^{AB}$ and $[\varepsilon]_B^{AB}$ with energy.

3.8 HIGH-ENERGY EDGE OF AN ENERGY SPECTRUM FOR AN ELEMENTAL SAMPLE WITH SEVERAL ISOTOPES

In the preceding discussions we treated the sample as composed of mono-isotopic elements. In general, an element has several stable isotopes of the same atomic number, but different atomic mass. The kinematic factor differs for each isotope. As a consequence, a sample of such an element has a backscattering spectrum with steps in the high-energy edge as shown in Fig. 3.19. The formalism required to develop the spectrum height of such a

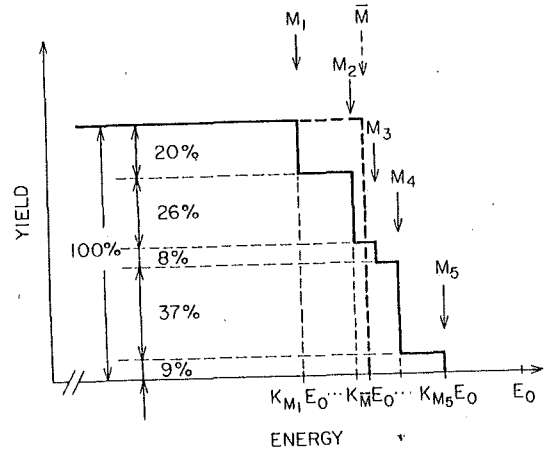


Fig. 3.19 Each isotope in an elemental sample contributes a step to the high-energy edge commensurate with its natural abundance. These isotopic steps are often so close to each other that the high-energy edge of an isotopic mixture can be replaced by a single step at some average location.

sample is like that for a compound sample. The equations are simplified by the fact that the stopping cross sections ε and scattering cross sections σ are practically the same for each isotope. However, since the kinematic factor K is different for each isotope, the stopping cross section factor $[\varepsilon]$ will differ for each isotope also. Assume that the mass M_i is present in a fractional abundance m_i . Then the kinematic factor K_{M_i} will specify a stopping cross section factor, which we can denote as $[\varepsilon]_{M_i}$. The ratio of the spectrum heights at the surface for any two isotopes, such as M_3 and M_4 , is then

$$\frac{H_{M_3,0}}{H_{M_4,0}} = \frac{m_3 [\varepsilon_0]_{M_4}}{m_4 [\varepsilon_0]_{M_3}} \quad (3.78)$$

by Eq. (3.72). For backscattering of ^4He in the megaelectron volt energy range, the ratio of isotopic $[\varepsilon]$'s is very close to unity and the ratio of the spectrum heights at the surface equals the ratio of the fractional abundances, as indicated in Fig. 3.19 for a sample containing five isotopes, such as Ge.

With ^4He ions in the megaelectron volt range and conventional solid-state detection systems, the isotopic steps in the high-energy edge are difficult to resolve when the element is of medium or heavy mass. The spectrum is then often interpreted as a single step of an average mass $\bar{M} = \sum_i m_i M_i$ at the position $K_{\bar{M}} E_0$ in the energy scale. This procedure is actually incorrect, because the kinematic factor is not a linear function of M . Strictly taken, the mean of the isotopic steps is located at $\bar{K} E_0 = (\sum_i m_i K_{M_i}) E_0$ and $\bar{K} \neq K_{\bar{M}}$ in general. The difference is insignificant for target masses much larger than the projectile mass, and usually K is used for \bar{K} or $K_{\bar{M}}$. We follow this usage in this book as well. The table of Ziegler (1973) gives $K_{\bar{M}}$, not \bar{K} .

3.9 ENERGY LOSS AND YIELD RESPOND TO ATOMS PER UNIT AREA

Up to this point in our development of the subject we have derived general formulas for converting energy to depth and for calculating the height of a backscattering spectrum. The purpose of this section is to emphasize the facts that (i) depth has a specific meaning in backscattering spectrometry which is not that of distance, as commonly associated with the word, but, rather refers explicitly to atoms per unit area, and (ii) the height of a backscattering spectrum does not depend on the atomic volume density of the target.

The fact that the energy loss that particles incur when they penetrate through a sample does not depend on the atomic density can be seen with the help of a conceptual experiment shown in Fig. 3.20, where a beam of

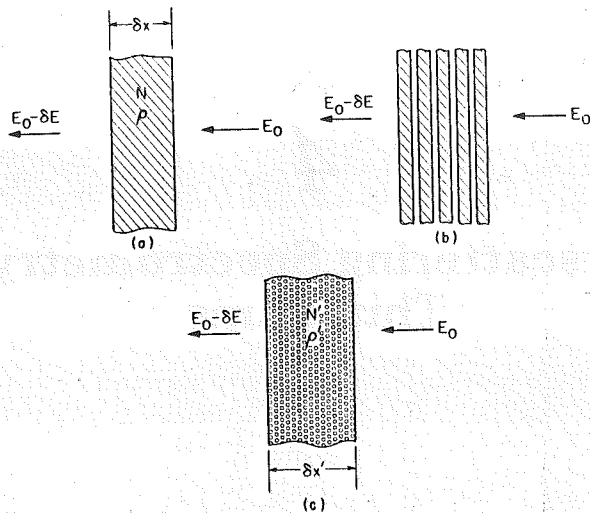


Fig. 3.20 Three different samples of the same material but different overall density all of which generate the same backscattering spectrum.

particles is shown incident perpendicularly with energy E_0 on three different samples. In the first case (Fig. 3.20a), the sample is a thin film of atomic density N , specific gravity ρ , and thickness δx . After transmission through the target, the particle energy is $E_0 - \delta E$. Imagine next that the physical thickness of this sample is increased to a value $\delta x'$ by slicing it into thin slabs and spacing them. Clearly, no energy is lost as the beam crosses these spaces, since no matter is present there. Hence δE is unchanged. Imagine now that this procedure is carried to the limit so that the additional volume is distributed microscopically and uniformly throughout the sample. Again, δE is unchanged, but the atomic density has been reduced to a value $N' < N$. Similarly, the specific gravity is now $\rho' < \rho$. This shows that the energy loss depends only on the amount of material traversed regardless of the physical thickness.

The number of atoms traversed is expressed by $N \delta x = N' \delta x'$. The energy loss δE is given by $\delta E = (dE/dx)dx = (dE/dx)' \delta x'$. This shows that dE/dx depends on the atomic density of the target. On the other hand, the energy loss can also be written $\delta E = \epsilon N \delta x = (\epsilon)' N' \delta x'$. Since $N \delta x = N' \delta x'$, then $\epsilon = (\epsilon)'$. The formal description of energy loss as

$$\delta E = \epsilon N \delta x \quad (3.79)$$

has the advantage of expressing the energy loss in terms of the two physically relevant quantities: ϵ , the specific energy loss per atom, and $N \delta x$, the number

of atoms per unit area. For this same reason we prefer the formulation

$$\Delta E = [\epsilon] N \Delta x \quad (3.80)$$

rather than $\Delta E = [S] \Delta x$ for energy loss in backscattering. Whenever a measurement made by backscattering spectrometry expresses depth in units of length, the knowledge of the density has been assumed. The word "depth" used in connection with backscattering therefore indicates a distance only when the density is known; otherwise "depth" stands as an abbreviation for the number of atoms per unit area $N \Delta x$ over the distance Δx traversed.

The three samples shown in Fig. 3.20 all have the same number of atoms per unit area. This is stated by the equality $N \delta x = N' \delta x'$. It also must follow, then, that the total numbers of counts generated by these samples in backscattering measurements are the same. Since the energy widths of the backscattering signals from these samples are the same, the spectra of all three are indistinguishable. Therefore the height (counts per channel) of a backscattering signal is independent of the atomic density of the sample. For example, backscattering measurements on a sample of evaporated silicon that has an atomic density less than that of bulk silicon will give spectra identical to those obtained from bulk silicon. One should note, however, that density changes generated by additional atoms of a different species do change the spectrum, as discussed further in Section 5.3. Such modifications are not of the type described by Fig. 3.20, because the additional volume contains energy-absorbing atoms, not voids.

3.10 NUMERICAL METHODS TO COMPUTE BACKSCATTERING SPECTRA

Many laboratories engaged in backscattering analysis have developed computer programs to calculate backscattering spectra. Most of these programs are tailored to meet the specific needs of the respective laboratories.

One program is available in documented form.[†] It is written in Fortran and can accommodate samples consisting of up to 10 distinct layers with up to 10 elements. The program considers only beams of normal incidence and does not incorporate energy straggling. Bragg's rule of additivity of stopping cross sections is assumed to be valid, and the composition and thickness of each layer in the sample are constant.

[†] The program is available from Rome Air Development Center, Air Force Systems Command, Griffiss Air Force Base, New York, as Report RADC-TR-76-182 (June 1976), entitled "Computer Program to Synthesize Backscattering Spectra for Samples Composed of Successive Layers of Uniform Thickness and Composition," by P. Børgeesen, J. M. Harris, and B. M. U. Scherzer.